ELECTRICAL RESISTIVITY STRUCTURE BENEATH MT. ERCİYES

CENTRAL ANATOLIA, TURKEY

by

Ruken YAZICI BOZKURT

B.S., Geological Engineering, Hacettepe University, 2014

Submitted to Kandilli Observatory and Earthquake

Research Institute in partial fulfillment of

the requirements for the degree of

Master of Science

Graduate Program in Geophysics

Boğaziçi University

2022

Dedicated to my mother.

ACKNOWLEDGEMENTS

ABSTRACT

ELECTRICAL RESISTIVITY STRUCTURE BENEATH MT. ERCİYES CENTRAL ANATOLIA, TURKEY

The Central Anatolia (CA) is an intermediate belt between the Pontides and the Anatolide-Tauride blocks. Numerous basins, folds, faults, volcanic fields and rich mineral resources in the region have attracted the attention of geoscientists for years. Mt. Erciyes is a Quaternary-aged stratovolcano located in CA, which has not been activated for a long time. In this thesis, I aimed to perform three-dimensional (3 - D) imaging of its electrical properties using magnetotellurics (MT) and interpret its structure. MT method has been extensively used in the exploration of volcanic areas. This study can be considered as the first systematic application of the MT performed in the vicinity of Mt. Erciyes. Between 2013 and 2018, deploying 48 wide-band MT soundings forming a grid surrounding the volcano and its location as part of the Continental Dynamics/Central Anatolian Tectonics project (CD/CAT). The obtained data set was used for determining the dimensionality of the survey area, and the realistic electrical structure of the region was achieved with 3 - D solution algorithms including 38 station data. The results showed that the regional geoelectric strike direction is $\sim N25°E$ which coincides with the structural strike of the region. For determining the dimensionality of the MT data, phase tensor analyses were performed. The observed wide-band data were inverted using a 3 - D inversion algorithm known as the MODEM$^{©}$ in two distinct ways; with and without topography information to reveal the electrical structure. The 3 - D inversion results revealed three distinct conductivity features: a widespread conductive anomaly found beneath the volcano and two conductive areas in the vicinity of the volcano. When the final model is examined, it is possible to observe that the conductive regions are separated from each other. If the final model is examined together with the geological data, it is noticed that the boundaries of the conductor coincide with the faulting in the region.

ÖZET

ERCİYES VOLKANI'NIN ELEKTRİK YAPISININ MANYETOTELLÜRİK YÖNTEM İLE İNCELENMESİ

İç Anadolu Bölgesi, Pontitler ile Anatolid - Torid blokları arasında yer alan ara bir kuşaktır. Bölgede bulunan çok sayıda havza, kıvrım, fay, volkanik alan ve zengin maden kaynakları yıllardır yerbilimcilerin ilgisini çekmiştir. Erciyes Volkanı, Orta Anadolu bölgesinde yer alan ve uzun süredir aktivite gözlenmeyen Kuvaterner yaşlı bir stratovolkandır. Bu tezde manyetotellürik (MT) yöntem kullanarak elektriksel özelliklerinin üç-boyutlu (3 - B) görüntülenmesini ve yapısını yorumlamayı amaçladım. MT popüler bir jeofizik yöntemdir ve son yıllarda volkanik alanların araştırılmasında yaygın olarak kullanılmaktadır. Bu çalışma, Erciyes Volkanı civarında yapılan MT yöntemin ilk sistematik uygulaması olarak kabul edilebilir. 2013 - 2018 yılları arasında, Kıta Dinamikleri/Orta Anadolu Tektoniği projesinin (CD/CAT) bir parçası olarak volkanı ve bulunduğu bölgeyi çevreleyen bir ağ oluşturacak şekilde 48 geniş bantlı MT ölçüm gerçekleşmiştir. Elde edilen veri seti boyutluluk analizinde kullanılmış ve 38 istasyon verisini içeren 3 - B çözüm algoritmaları ile bölgenin gerçek elektriksel yapısı elde edilmiştir. Analiz sonuçları, bölgesel yer-elektrik yöneliminin $\sim K25°\text{D}$ olduğunu gösterir ve bölgenin yapısal doğrultusu ile örtüşür. MT verilerinin boyutluluğunu belirlemek için faz tensör analizleri yapılmıştır. Gözlemlenen geniş bant verileri, MODEM© olarak bilinen 3 - B bir ters çözüm algoritması kullanılarak, Erciyes Volkanı ve içerisinde bulunduğu bölgenin elektriksel yapısı ortaya çıkartılmıştır. Ters çözüm algoritması iki farklı şekilde kullanılmıştır; topografya bilgisi içeren ve topografya bilgisi içermeyen. 3 - B ters çözüm sonucu, üç farklı iletkenlik özelliği ortaya çıkarmıştır: volkanın altında bulunan yaygın bir iletken anomali ve volkanın yakınında iki farklı iletken alan. Nihai model incelendiğinde, iletken bölgelerin birbirinden net bir şekilde ayrıldığını gözlemlemek mümkündür. Jeolojik verilerle birleştirildiğinde iletken sınırlarının bölgedeki faylanmalarla örtüştüğü görülmektedir.

TABLE OF CONTENTS

LIST OF FIGURES

LIST OF SYMBOLS

A	Anisotropy
$\mathbf{B}$	Magnetic flux density
$\mathbf{C}$	Distortion tensor
$\mathbf{C_d}$	Data covariance matrix
$\mathbf{C_m}$	Model covariance matrix
d	Data parameters
$\mathbf{D}$	Electric displacement
$\mathbf{D_A}$	Distortion matrix
$\mathbf{D_p}$	Data response function
$\mathbf{E}$	Electric field
g	Gain
$\mathbf{H}$	Magnetic Field
$\mathbf{J}$	Electric current density
k	Wave number
$\mathbf{m}$	Model parameters
q	Electric charge density
S	Shear
t	Time
T	Twist
$\mathbf{X}$	Real part of the impedance tensor
$\mathbf{Y}$	Imaginary part of the impedance tensor
$\mathbf{Z}$	Impedance tensor
$\mathbf{Z_{(1-D)}}$	Impedance tensor for 1-D medium
$\mathbf{Z_{(2-D)}}$	Impedance tensor for 2-D medium
$\mathbf{Z_{(3-D)}}$	Impedance tensor for 3-D medium
α	Non-invariant angle
β	Skew angle
δ	Skin depth

ϵ	Electric permittivity
κ	The Swift's skew
λ	Wavelength
μ	Magnetic permeability
ρ	Resistivity
ρ_a	Apparent resistivity
σ	Electrical conductivity
ϕ	Phase
$\mathbf{\Phi}$	Phase tensor
ω	Angular frequency

LIST OF ACRONYMS/ABBREVIATIONS

3-B	Üç - boyutlu
1-D	One-dimensional
2-D	Two-dimensional
3-D	Three-dimensional
ACA	Aegean - Cyprian Arc
ATB	Anatolide – Taurides Block
CA	Central Anatolia
CP	Central Pontides
CACC	Central Anatolian Crystalline Complex
CAFZ	Central Anatolian Fault Zone
CD / CAT	Continental Dynamics / Central Anatolian Tectonics
ÇB	Çankırı Basin
DEF	Dündarlı - Erciyes Fault
DFT	Discrete Fourier Transform
DSF	Dead Sea Fault
EAF	East Anatolian Fault
EFZ	Ecemiş Fault Zone
EM	Electromagnetic
EEB	Erciyes Extensional Basin
ERT	Electrical Resistivity Tomography
ESC	Erciyes Stratovolcano Complex
GPS	Global Positioning System
IAES	İzmir – Ankara – Erzincan Suture
ITS	Inner Taurid Suture
MT	Magnetotellurics
NAF	North Anatolian Fault
NLCG	Non-linear Conjugate Gradient
SPB	Sultansazlığı Pull-Apart Basin
TE	Transverse electric

TM	Transverse magnetic
TVZ	Taupo Volcanic Zone
USGS	The U.S. Geological Survey
VTI	Valibabatepe Ignimbrite Eruption

1. INTRODUCTION

The Earth is an enormous, complicated planet full of unknowns. For many years, geoscientists have been trying to explore the internal properties of this mysterious planet and reveal unknown aspects. Even though there has been research about the Earth for centuries, geoscientists still do not have enough information for the full description of the Earth. Along with the excitement of discoveries, a great curiosity towards the unknown keeps geoscientists exploring. This curiosity has led to the emergence and development of earth science. Geology is a discipline that studies the evolution process of the Earth over approximately four and a half billion years and attempts to resolve the structure and decipher the process of its formation of the planet Earth. Geophysics is another branch of earth science that investigates the Earth by benefiting from the fundamental principles of physics. Utilizing the geophysical methods, one can obtain numerous results about the physical properties of the Earth. In this thesis, both branches, namely geology and geophysics, were used for understanding the evolution of Mt. Erciyes and its vicinity.

Electrical conductivity (or its reciprocal electrical resistivity) is a fundamental property of material. The electrical conductivity is a measure of the capacity to conduct electric current within material. In a material with high conductivity, the electrical current flows easier (Heaney, 2003). It is a well-known fact that various rock types, sediments and geological structures can have different electrical conductivity values (Haak and Hutton, 1986). Measuring the electrical conductivity of these structures allows us to distinguish different materials and structures from each other and may give information about the tectonic processes. Magnetotellurics (MT) is a geophysical method that resolves the subsurface electrical conductivity by measuring variations in the magnetic and electric fields at the Earth's surface (Rikitake, 1948; Tikhonov, 1950 and Cagniard, 1953). Fundamentally the method uses naturally occurring electromagnetic (EM) fields to probe the Earth's electrical properties.

Vozoff (1991) states that there are two natural sources for the MT signal. These are the lightning and thunderstorm activity (MT fields above about 1 Hz) and Solar activity-magnetosphere interactions (MT signals below 1 Hz). For signals below 1 Hz the quality of the measured data is thus closely related to the activity of the Sun. Between these two sources a decreasing trend in the amplitude of the MT signal is observed (in the frequency range between 10 Hz and 0.1 Hz). This range is called the dead-band (Simpson and Bahr, 2005). More detailed information about the theory will be presented in the following section (In this thesis, period and frequency were used interchangeably.).

According to the information received from the USGS (the U.S. Geological Survey), the number of the possibly active volcanoes is around 1350. The fact that there are so many volcanoes on Earth has attracted the attention of many geophysicists for their MT applications, especially to observe resistivity patterns in regions where volcanoes are dense and to learn more about the volcanic complex. For the sake of example, in a study involving five large stratovolcanoes in Japan, a hydrothermal system of a volcanic structure was investigated, and the results obtained were compared and compatible with another geophysical method named self-potential (Aizawa et al., 2009). It is possible to give more examples of the study of volcanism in Japan. Yoshimura et al. (2018) investigated the shallow resistive structure of the Hakone volcano after a phreatic eruption and active seismicity using the MT method. They observed the presence of more than one bell-shaped conductor in the region. Naruko, a stratovolcano that has not been active for a long time, was studied by Ogawa et al. (2014), a high resistivity region with an NNE-SSW direction and a width of $10 - 15$ km was observed in the east, and a front arc conductor without a root was observed in the further east. Ceboruco Volcano, a quaternary-aged stratovolcano in Mexico, is one of the most active volcanoes in its region. Observations were made in November 2016 to investigate the geoelectric and hydrothermal systems of the volcano by Fuentes-Arreazola et al. (2021). According to the model results two main conductors and a shallow conductor associated with the regional aquifer were observed. It is stated that there are no magma chambers observed from this dataset.

The Taupo volcanic zone (TVZ), located on the North Island of New Zealand, is a back-arc basin characterized by many active volcanoes (Cole, 1990). There are a lot of MT studies conducted to understand and better interpret the dynamics of the region and its vicinity, such as Heise et al. (2008), Ingham et al. (2009), and Bertrand et al. (2012). As a result of a study conducted at Krafla, an active volcano located in Iceland, a layer of hydrothermal alteration was observed under the volcano, and two different layers with different resistivities were observed (Lee at al., 2020). In another MT study to investigate the composition of magma and the characteristics of the hydrothermal system of Newberry Volcano, a relatively resistive magma reservoir of about $50\Omega m$ was discovered (Bowles − Martinez and Schultz, 2020). Another study investigating the magma reservoir was examined by Pina−Varas et al. (2018) for the Teide Volcano in Tenerife. In the study, it was stated that many studies have been carried out in this area, and according to the results obtained, discussions about the reservoir locations and size are still ongoing. It is emphasized that the most important result of the final model is the incompatibilities with a reservoir at depths shallower than 8 km. Another example of MT studies in Europe can be given from Italy, which is home to many volcanoes. Mauriello et al. (2000) was investigate the structure of Mt. Etna, and presented that the center is characterized by very high resistivity values and E-W-directed resistive anomalies are a line that cuts the region. The studies are not limited to the ones mentioned in this text. It is possible to find many studies conducted in all locations with volcanoes worldwide and on volcanoes with distinct activities.

Not only in the world but also in Turkey, the MT method is used in many issues, and its results are discussed. Important studies have been carried out in the fault zones using the MT method. Karaş et al. (2017) studied the Ganos fault zone using the MT method, observed conductive anomalies along the fault zone, and emphasize that auxiliary faults merge to create a wide fluid-containing environment. Another important result obtained is that the fault zone has the potential to produce earthquakes due to the lack of fluid paths and mechanically strong and resistant environments. Avşar et al. (2013) investigated the properties of NAF in the Erzincan Basin using the MT method.

It was observed that the basin is characterized by unconsolidated sediments 3 km thick and is at a depth of 3.5 km towards the east. Viewing of the fault zone conductor in the west has been interpreted as the westward fluid content of the NAF. For example, Tank et al. (2005) and Kaya et al. (2013) can be given as examples of independent studies conducted for the Izmit Earthquake and the triggering fault the North Anatolian Fault zone (NAF). Tank et al. (2005) indicates the presence of a liquid-rich and high-resistivity region and argues that the underlying low - resistivity region is home to earthquake formation which represented by partial melting. Kaya et al. (2013) emphasized that the results of Tank et al. (2005) were supported in this study, in addition, there were various resistive and conductive anomalies in the study region. The study carried out by Bayrak and Nalbant (2001) it was aimed to display the conductive crust structure of Western Turkey (İzmir-Ankara Suture Zone, the Bornova Flysch Zone, and the Menderes Massif) with the MT method, and 2-D models were obtained with 35 stations. According to the model results obtained, the shell structure is divided into two; a viscoelastic lower crust conductive region and a brittle upper crust represented by the relatively high resistive region. Below the İzmir-Ankara Suture Zone, a structure containing two anomalies is observed, which is thought to have arisen due to its high seismic activity. Another significant result shows that western Turkey's lithosphere/asthenosphere boundary is quite shallow (with thicknesses varying between 30 and 50 km). Another study close to this suture zone is Özaydın et al. (2018) study, which covers the Çankırı Basin (ÇB) and the Central Pontides (CP). The NAF segment, which had caused a major earthquake in the past, showed itself in this study with its resistive properties exhibiting a depth of approximately 25 km. In the final model, the CP was interpreted as a metamorphic lower crustal section and observed as a fluid-filled conductive anomaly. The conductive anomaly located below the ÇB is associated with seismicity. Another essential study in which the MT method is used in crust and mantle studies belongs to Gürer et al. (2004). In this study, they are presented that there are different horizontal conductors with conductive lower crust and resistive upper crust and that these anomalies are compatible with the surrounding fault zones.

Volcanoes are another study area where the MT method is used in Turkey. Although it has not yet gained enough popularity, it has an increasing trend. One of the most recent studies is by Başokur et al. (2022), who studied the Karadağ stratovolcano. They present essential consequences such as a magma reservoir at a depth of about $3 - 7$ km, a shallow low resistive anomaly due to near-surface hydrothermal alteration. Tank and Karaş (2020), aimed in their study to solve the hydrothermal structure beneath the Mt. Hasan composite volcano, argued that the existence of a possible magma chamber at a depth of approximately $4 - 6$ km and the existence of clay-containing, highly conductive anomalies limited by the nearby NW–SE aligned faulting. Studies on volcano surveys with the MT method in Turkey are unfortunately limited to these two studies.

Mt. Erciyes (38.53°N, 35.45°E) is a stratovolcano located in Central Anatolia (CA), and with its 3917 m altitude, it is known as the highest stratovolcano in this region (Şen et. al., 2003, Friedrichs et al., 2021). The volcano and the corresponding volcanic activity have produced various types of products all along its evolution. Depending on the magmatism types alkaline and calc-alkaline rocks can be found in the vicinity of Mt. Erciyes. Basaltic, andesitic, dacitic and rhyodacitic rocks are abundant around the volcano (Kürkcüoğlu et al., 2004). Many researchers tend to examine the volcanological evolution of this late Pliocene − Quaternary-aged stratovolcano in two stages: (1) The Koç Dağ, and (2) The New Erciyes (Kürkcüoğlu et al., 1998, Şen et al., 2003) stages. The first stage was active between the Pliocene (5.333 - 2.58 Ma) and the Quaternary (2.588 - 0.005 Ma), and The New Erciyes stage took over onwards (Şen et al., 2003, Aydar et al., 2019). According to Aydar et al. (2019), ^{14}C dating proves that the volcano has erupted more than once in the Early Holocene (0.0012 Ma - Present).

The region where Mt. Erciyes located is called the Erciyes Stratovolcano Complex (ESC). This region is located at the center of a basin known as the Erciyes extensional basin (EEB), and this basin is restricted by Yeşilhisar (in the west) and Develi (in the west) normal faults (Higgins et al., 2015). The basin is considered as one of the most active regions of CA as it is surrounded by many active auxiliary faults (Koçyiğit

and Beyhan, 1998). The Ecemiş Fault Zone (EFZ) as part of the Central Anatolian Fault Zone (CAFZ), is one of the most active and essential faults in this region. It is a north-trending fault that cuts the caldera of the volcano. The significance of EFZ is that it controls the eastern part of the CA volcanic state (Dirik and Göncüoğlu, 1996). The basin where ESC and EEB are located is named Sultansazlığı pull-apart basin (SPB) and is associated with the activity of EFZ (Koçyiğit and Beyhan, 1998; Şen et al., 2003). SPB started to take shape with an east-west extension starting from the Upper-Miocene (Kaymakçı et al., 2001). Then expanded and formed by normal faults after the Pliocene (Koçyiğit and Beyhan, 1998; Dirik, 2001; Yıldırım et al., 2016).

Mt. Erciyes and its surroundings have attracted the attention of many earth scientists, numerous studies have been carried out on it. One of the earliest studies on Mt. Erciyes is by Innocenti et al. (1975). In this study, in which Neogene-aged calc-alkaline volcanism in Kayseri - Niğde region was investigated, Erciyes and its related volcanism were also mentioned. Kürkçüoğlu et al. (2001), in their study, argue that volcanic products generally exhibit a calc-alkaline character, and that tholeiitic basalt is also present, while basalts have a complex origin. One of the most detailed studies examining Erciyes belongs to Koçyiğit and Erol (2001). This study investigated the volcano, its basin, margin rocks, faults affecting the tectonics of the region and the seismicity of the study area. As a result, many volcanic cones and sills, dykes and ignimbrites that shaped the volcano were mentioned. Another important result is that the tectonics of the volcano are indicated by the Yeşilhisar, Erciyes and Develi fault segments. An original study on this volcano belongs to Maden (2010). Aimed to determine the thermal regime of the CA, the spectral analysis method was applied to the magnetic anomaly data, and the Curie-point depth and heat flow values of the Mt. Erciyes region were determined. The result obtained reveals the Curie depth in the study area as 13.7 km. It is thought that this result reflects the high geothermal potential of the region and partial melting of the crust contributes to this potential. Friedrichs et al. (2021) reconstructed the eruption timing of four early Holocene domes around Mount Erciyes by applying the zircon double-dating method for disequilibrium correction. As a result, the scenario in which all the Holocene domes erupt simultaneously has been proposed, ignoring the minor differences in mineralogy (~ 0.0089 Ma).

Males va Gottsmann (2021) conducted research on the long-term rest period of Erciyes and the detectability of magma recharge. As a result, they argue that magma recharge may not be detected using conventional geodetic and gravimetric methods. However, it is suggested that Erciyes is potentially sufficient to maintain an active magma reservoir containing eruptive magma. There are also studies on glaciation in the region. Sarıkaya et al. (2003) emphasize that Erciyes underwent an essential glaciation period in the Late Quaternary, which can be observed in three phases. The main purpose is to take samples from moraine sets for cosmogenic dating. For this reason, they continued their studies on three different moraine samples. In addition, as a result of the study, glaciation was observed on four main valleys and one ridge. Another important result is that the glaciers began to retreat.

This thesis aimed to investigate the electrical resistivity structure beneath Mt. Erciyes and its surroundings through three-dimensional modeling of wide-band MT data collected at 38 sounding locations.

In total the thesis can be examined under 8 headings. Following the introduction, in chapter 2, the theory of the MT method is explained in detail by reporting the theoretical aspects, the assumptions and the need-to-know terms of the MT method. In the third chapter, the geological and tectonic settings of the study area are described. Further information about the faults surrounding the volcano and the EPB are also explained. The stratigraphy of the ESC is given. The fourth chapter focuses on the strike and dimensionality analyses. To measure the regional strike and geoelectric strike, the geological and EM data were utilized, respectively, and the obtained results with these techniques are presented in ongoing chapters. The following section, chapter 5, has a significant role in achieving the aim of this thesis. Chapter 5 is based on the modeling of the MT data from the site, which has been closely studied tectonically and geologically in other chapters. The process of justifying the MT data according to the assumptions made in the application of the method is used for obtaining the models and chapter 5 focuses on this topic. In the following chapters, the results and the interpretations are made based on the modeling results and are presented in chapter 6 and 7, respectively. Finally, in the conclusion, chapter 8, the results are summarized.

2. THEORY OF MAGNETOTELLURICS (MT)

Geophysics is a discipline that provides a wide field of study. One way of classifying the geophysical methods is based on the sources of the signals used. The geophysical methods can be active or passive. Active methods use artificial sources, energy and/or signals while exploring the Earth. Seismic methods or electrical resistivity tomography (ERT) methods can be given as examples for active methods. However, unlike active methods, passive methods do not require any artificial sources. Instead, they utilize natural signals and/or energy acting on the Earth. MT is a passive EM exploration method for resolving the geoelectric structure of the subsurface. MT is widely used in many commercial areas such as oil and hydrocarbon exploration (Constable et al., 1998; Unsworth, 2005; Constable and Srnka, 2007; Constable, 2010; Zhang et al., 2014), mining (Farquharson, and Craven, 2009; Yang et al., 2018), exploration of geothermal systems (Heise at al., 2008; Munoz, 2014), groundwater surveying (McNeill, 1990; Asaue et al., 2012), investigating volcanoes (Ingham et al., 2009; Aizawa et al., 2016; Tank and Karaş, 2020; Tseng et al., 2020), and examination of fault systems (Stanley et al., 1990; Tank et al., 2005; Kaya et al, 2009; Karaş et al., 2020) as well as crust-mantle research (Chen et al., 2002; Unsworth et al., 2004) and earthquake prediction studies (Chouliaras and Rasmussen, 1988).

The MT theory has its roots back in the late 1940's and early 1950's by the pioneering works of Rikitake (1948), Tikhonov (1950) and Cagniard (1953). All three studies focused on the idea of electric **E** and magnetic **H** field variations on the Earth's surface, using Maxwell's equations and with some essential assumptions. To better understand the MT method, it is possible to summarize these basics in a few steps (Simpson and Bahr, 2005):

1. Mawwell's equations
2. Plane wave
3. Source of EM energy and ionospheric current system
4. Removal of distortion

5. Some basic concepts in the MT method

2.1. Maxwell's Equations

Maxwell's equations are one of the most crucial discoveries of modern physics that consist of four equations. Maxwell's equations describe how electric and magnetic fields are exchanged and produced by each other, by charges and currents. The four partial differential equations are:

Faraday's Law:

$$\nabla \times \mathbf{E} = -\frac{\partial B}{\partial t}. \tag{2.1}$$

Amperè's Law with Maxwell's correction of displacement current term

$$\nabla \times \mathbf{H} = \mathbf{J} + \frac{\partial \mathbf{D}}{\partial t}, \tag{2.2}$$

the magnetic and the electric laws of Gauss

$$\nabla \cdot \mathbf{B} = 0 \tag{2.3}$$

$$\nabla \cdot \mathbf{D} = q \tag{2.4}$$

where $\mathbf{E}$ is the electric field (in V/m), $\mathbf{B}$ is the magnetic flux density/magnetic induction (in Tesla or nanoTesla), $\mathbf{H}$ is the magnetic field (in Amperè/meter), $\mathbf{J}$ is the electric current density (in Amperè/meter^2), $\mathbf{D}$ is the electric displacement (in Coulomb/meter^2) and q is the density of electric charges (in Coulomb/meter^3) (Ward and Hohmann, 1987).

Maxwell's first Equation (2.1) is based on Faraday's law of EM induction. This law states that the change in the magnetic field over time creates an electric field. The second Equation (2.2) is based on Amperè's circuit law with Maxwell's correction of

displacement current term $\left(\dfrac{\partial \mathbf{D}}{\partial t}\right)$. It sets up the relationship between the electric currents and the magnetic fields. This equation shows that magnetic field intensity develops as a result of the effects of current density and time-varying electric field. The last two Equations (2.3) and (2.4) are known as magnetic and the electric laws of Gauss (2.3) and is based on the Gauss' law on magnetostatics. This law states that a closed surface integral of the magnetic flux density is equal to the total scalar magnetic flux in any surface of any shape or size in any medium. Equation (2.4) is derived from Gauss' law of electrostatics, which states that the shape and intensity of the electric field created by an electrically charged object. The product of the electric flux density vector and the surface integral on a closed surface is equal to the charge (Serway and Jewett, 2012).

The following formulas are the constitutive relations given about the electric and magnetic field medium parameters (Ward and Hohmann, 1987).

$$\mathbf{B} = \mu \mathbf{H} \tag{2.5}$$

$$\mathbf{D} = \varepsilon \mathbf{E} \tag{2.6}$$

$$\mathbf{J} = \sigma \mathbf{E} \tag{2.7}$$

where μ is the magnetic permeability (in Henry/meter), ε is the electric permittivity (in Farad/meter) and σ is the electrical conductivity (in Siemens/meter).

The second equation of Maxwell can be written as follows when substituting the Equations (2.6) and (2.7) into Equation (2.2)

$$\nabla \times \mathbf{E} = -\mu \frac{\partial \mathbf{H}}{\partial t} \tag{2.8}$$

$$\nabla \times \mathbf{H} = \sigma \mathbf{E} + \varepsilon \frac{\partial \mathbf{E}}{\partial t} \tag{2.9}$$

By applying vector identity

$$\nabla \times \nabla \times \mathbf{A} = \nabla(\nabla \cdot \mathbf{A}) - \nabla \cdot \nabla \mathbf{A} = \nabla \nabla \cdot \mathbf{A} - \nabla^2 \mathbf{A} \tag{2.10}$$

In accordance with assuming that there are no free charges on the Earth and Equations (2.8) and (2.9) in their curl form to be written as Helmholtz Equations are as follows ($\nabla \cdot \mathbf{E} = 0$):

$$\nabla^2 \mathbf{E} = \mu \frac{\partial}{\partial t} (\nabla \times \mathbf{H}) = \mu\sigma \frac{\partial \mathbf{E}}{\partial t} + \varepsilon\mu \frac{\partial^2 \mathbf{E}}{\partial^2 t} \tag{2.11}$$

$$\nabla^2 \mathbf{H} = -\sigma (\nabla \times \mathbf{E}) - \varepsilon \frac{\partial}{\partial t} (\nabla \times \mathbf{E}) = \mu\sigma \frac{\partial \mathbf{H}}{\partial t} + \varepsilon\mu \frac{\partial^2 \mathbf{H}}{\partial^2 t} \tag{2.12}$$

Considering some assumptions, Helmholtz Equations can be written as follows (time dependence as $e^{-i\omega t}$ and surface amplitudes of a plane wave is $\mathbf{E}_0$ and $\mathbf{H}_0$)(Ward and Hohmann, 1987).

$$\nabla^2 \mathbf{E} = i\omega\mu\sigma \mathbf{E} - \omega^2 \varepsilon\mu \mathbf{E} \tag{2.13}$$

$$\nabla^2 \mathbf{H} = i\omega\mu\sigma \mathbf{H} - \omega^2 \varepsilon\mu \mathbf{H} \tag{2.14}$$

Of the two elements on the right-hand side of the Ampere's law, the conduction currents are relatively larger than the displacement currents and thus in the MT method it is assumed that the displacement currents are ignored ($\omega^2 \varepsilon\mu << i\omega\mu\sigma$). The so-called Helmholtz equations are then used to define the diffusion process (Kaufman and Keller, 1981).

$$\nabla^2 \mathbf{E} = i\omega\mu\sigma \mathbf{E} \tag{2.15}$$

$$\nabla^2 \mathbf{H} = i\omega\mu\sigma \mathbf{H} \tag{2.16}$$

2.2. Plane Wave

An important assumption that may be considered as one of the building blocks of the MT theory is the plane wave assumption (Figure 2.1). In the application of the MT method, it is assumed that the ionospheric activities create time-dependent changes in the Earth's magnetic field. The theory suggests that the ionosphere serves as a signal generator creating plane waves that travel to the surface of the Earth. Passing through this boundary, a small amount of it diffuses depending on the conductivity and the period of the plane wave creating telluric currents. At mid-latitudes, Cagniard's assumptions about source fields are frequently valid for fewer than 10^4 seconds (Madden and Nelson, 1964).
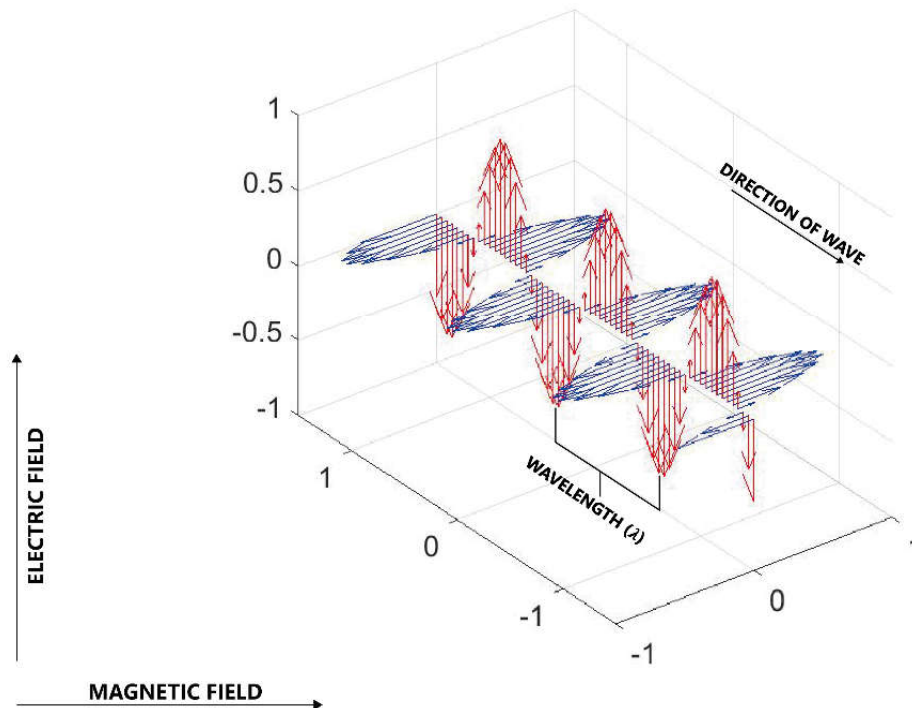
Figure 2.1. A visualization of a plane wave. The red lines give the direction of the electric field, and the blue lines the direction of the magnetic field.

Mathematical forms of a plane EM wave are as follow (Simpson and Bahr, 2005):

$$\mathbf{E} = \mathbf{E}_0 e^{i\omega t - \mathbf{k}z} \qquad (2.17)$$

$$\mathbf{B} = \mathbf{B}_0 e^{i\omega t - \mathbf{k}z} \qquad (2.18)$$

$\mathbf{E}$ and $\mathbf{B}$ symbolize the electric and magnetic fields, respectively with amplitudes at the origin $\mathbf{E}_0$ and $\mathbf{B}_0$. ω is angular frequency and λ is wavelength. ($\lambda = \frac{2\pi}{|\mathbf{k}|}$ and $\mathbf{k}$ is wavenumber) (Kaufman and Keller, 1981). In free space, the velocity of the EM is obtained from the ratio between $\mathbf{E}_0$ and $\mathbf{B}_0$.

Weinstein (1988) states some properties of EM waves as follows:

i. For an EM wave to be produced, there must be an accelerated charge.

ii. EM wave has the ability to propagate in a vacuum. Since they are uncharged, they are not affected by the magnetic and electric fields.

iii. They are transverse waves. Therefore, the electric field vector gives the magnetic field vector in the direction of propagation.

2.3. Source of the EM Energy

One of the most important results obtained from Maxwell's equations is based on the fact that, accelerated charges transmit electromagnetic waves. The EM energy term can be used to describe energies originating from space via stars such as the Sun, and they all travel in the form of waves. The Sun generates a natural radiation which is absorbed by the Earth's surface.

On the other hand, solar energy and lightnings cause natural changes in the Earth's magnetic field, these changes cause electric (telluric) currents below the Earth's surface (Figure 2.2).
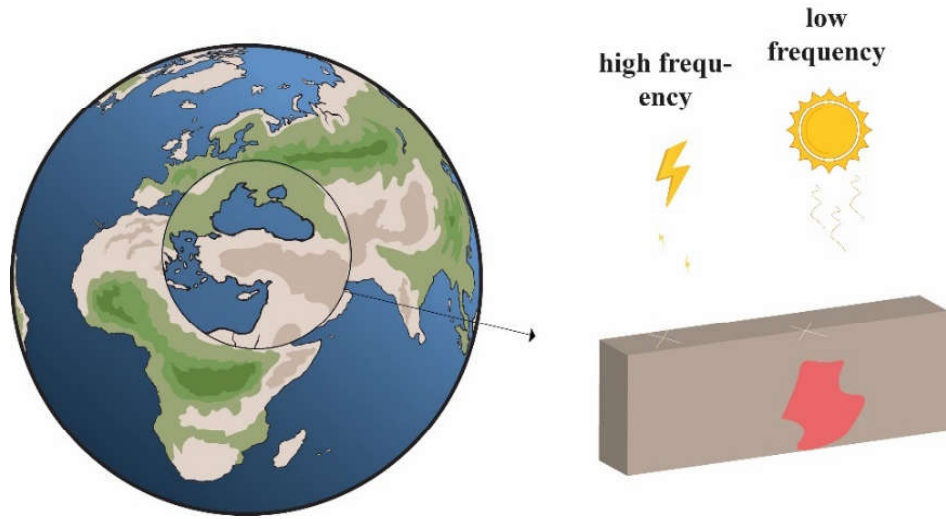
Figure 2.2. Global lightning activity and Sun's activity have vital importance for EM energy.

2.4. Ionospheric Current System

The ionosphere forms the basis of another essential assumption for the MT method. It is a layer located about 48 kilometers above the surface that extends for until 965 kilometers in space, containing plenty of electrons, ionized atoms, and molecules (Zell, 2020). (Figure 2.3). Natural EM sources in the frequency range of 10^4 Hz to 10^{-4} Hz originate from plasma processes in the Earth's magnetosphere and lightning discharges in the Earth's ionosphere (Kaufman and Keller, 1981; Vozoff, 1972; 1991). The reason this layer is so important is that it mediates the propagation of radio waves to distant places on the Earth. The propagation of radio waves is completely related to ion density. The ionosphere has a crucial place in geophysics because of its propagation character is due to its ions which is deeply affected by both wave and particle radiations from the Sun (Beynon, 1969; Rawer, 2013).
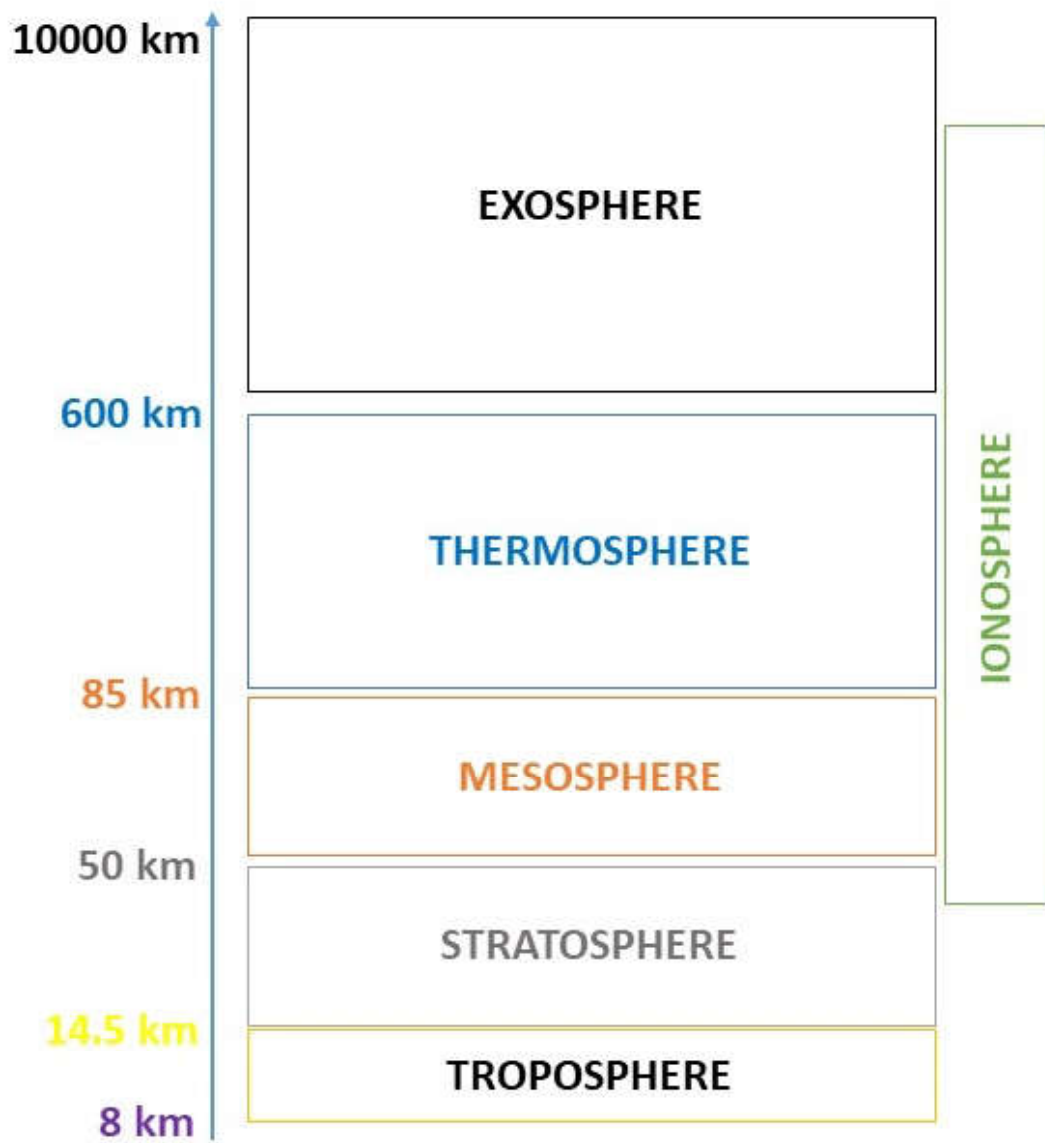
Figure 2.3. The layers of the atmosphere and the layer of the ionosphere. (Zell, 2020)

2.5. Removal of Distortion

The correct interpretation of the data in the MT method is essential to obtain a more accurate result. Local structures can distort regional electric fields, which is an important problem that will hinder the correct interpretation of the MT method. After removing the distortion reliably and feasibly, the data should be analyzed, and the results and interpretation adjusted accordingly.

Static shift, for instance, is one of the most common distortions faced in the modeling of MT data. Static Shift is a change in apparent resistivity that disrupts the interpretation of data (Spitzer, 2001). The static shift effect does not show itself in the phase curve, it is characterized by a vertical shift in the apparent resistivity curve by a frequency-independent factor. The reason is small-scale and inhomogeneous effects close to the surface (Sasaki, 2004). Static shift only affects the electric field and thus causes the apparent resistivity to shift. Therefore, false interpretations can be made if static shift is ignored. It does not affect the phase. For example, Beamish and Travassos (1992) recommend three methods (1. curve shifting, 2. statistical averaging, and 3. parameter constraints) for removing distortion and states that each method has its own pros and cons.

The data drawn for interpretation in this thesis were obtained through the phase tensor. The most important feature of the phase tensor is that it is distortion-free. Therefore, no distortion regulation has been made in this thesis.

2.6. Some Basic Concepts in the MT Method

Apart from the above-mentioned assumptions, there are basic concepts that are frequently used in this field and should be known. Considering that the MT method is a passive technique that includes electric and magnetic fields information, these measurements lead us to the impedance tensor.

In the application of the MT method, two horizontal electric (E_x and E_y) and magnetic (H_x and H_y) fields along with the vertical component of the magnetic field (H_z) are measured. These components are recorded in the time domain as time series and by Fourier transformation, they are transferred into the frequency domain (Ward and Hohmann 1987).

By taking the ratio of the horizontal components of the electric and the magnetic fields, the EM impedance tensor is obtained:

$$Z_{xx} = \frac{E_x}{H_x} \tag{2.19}$$

$$Z_{xy} = \frac{E_x}{H_y} \tag{2.20}$$

$$Z_{yx} = \frac{E_y}{H_x} \tag{2.21}$$

$$Z_{yy} = \frac{E_y}{H_y} \tag{2.22}$$

The general representation of the EM impedance tensor is given by a rank 2, 2×2 tensor,

$$\begin{bmatrix} E_x \\ E_y \end{bmatrix} = \begin{bmatrix} Z_{xx} & Z_{xy} \\ Z_{yx} & Z_{yy]} \end{bmatrix} \cdot \begin{bmatrix} H_x \\ H_y \end{bmatrix} \tag{2.23}$$

If the medium is one-dimensional (1-D), the conductivity variations just depend on the depth. In the case of conductivity variations depending on both depth and one of the horizontal components, the medium is accepted to be two-dimensional (2-D) (either $\rho(x, z)$ or $\rho(y, z)$). Two horizontal components together with the depth define the three-dimensional (3-D) medium ($\rho(x, y, z)$) (Vozoff, 1991).

In the MT method, while performing forward and inverse modeling, dimensionality analysis has an essential role in deciding the amount of data to be utilized by choosing 1-D, 2-D or 3-D earth (Marti et al., 2009).

In a 1-D medium the impedance tensor can be expressed as follow:

$$\mathbf{Z_{(1-D)}} = \begin{bmatrix} 0 & Z_{xy} \\ -Z_{yx} & 0 \end{bmatrix} \tag{2.24}$$

The principal components of this matrix are equal numerically and different from zero. In this case, the tensor relations of electric and magnetic fields are represented as in the above formulas.

However, for the emergence of 2-D, there are two different situations: if one of the components (either x or y) is parallel to the geo-electric strike or two components are not parallel to the geo-electric strike. In case of parallel,

$$\mathbf{Z_{(2-D)}} = \begin{bmatrix} 0 & Z_{xy} \\ Z_{yx} & 0 \end{bmatrix} \tag{2.25}$$

these principal components are both different from each other and zero. If not parallel to the strike, off-diagonal parameters are the same as mathematically but different from zero. The last possibility is that the medium is 3-D (Vozoff, 1991).

$$\mathbf{Z_{(3-D)}} = \begin{bmatrix} Z_{xx} & Z_{xy} \\ Z_{yx} & Z_{yy} \end{bmatrix} \tag{2.26}$$

Apparent resistivity is another essential concept frequently used in MT. The apparent resistivity curves are calculated with the help of impedance and solve for the electrical resistivity distribution of the medium depending on the frequency of the emitted signal. It is the first interpreted parameter during MT research.

Cagniard-Tikhonov formula presents apparent resistivity as follows:

$$\rho_a(\omega) = \frac{0.2}{f} \left[\frac{E_x(\omega)}{B_y(\omega)} \right]^2 \tag{2.27}$$

The phase difference between E_x and B_y is calculated as:

$$\varphi = arg(\mathbf{Z}) \tag{2.28}$$

For 1-D earth model, apparent resistivity and phase relationships are described as:

$$\varphi_{(1-D)} = \tan^{-1}\left(\frac{E_x}{B_y} \right) \tag{2.29}$$

The phase (φ), which we encounter here, is defined as the argument of impedance, it gives information about the phase difference between the electric and magnetic field components. In a homogeneous half-space, the constant value of the phase is 45°. Angles greater than 45° correspond to decreasing resistivity. This feature of the phase means that it is sensitive to changes in the true resistivity of the medium (Vozoff, 1991; Simpson and Bahr, 2005).

2.7. Dimensionality of the MT Data

The MT is a method that allows the determination of the resistivity distribution of the subsurface at depths ranging from a few tens of meters to hundreds of kilometers (Tikhonov, 1950; Cagniard 1953). The dimensionality in the MT method symbolizes the conductivity diversities of the underground.

In recent years, dimensionality analysis became a prominent tool used in the exploration of EM to resolve many problems. With the MT method, the electrical resistivity structure of the subsurface can be determined from a few hundred meters to hundreds of kilometers depth. Due to the target anomalies to be resolved, there are a wide range of applications that can be performed with the MT method. As the electrical conductivity is highly sensitive to the presence of fluids, MT is often utilized efficiently for problems that fluids are considered as important factors. These applications include (i) understanding geothermal systems, (ii) studying the fault's structure, (iii) determining melts around active volcanoes and (iv) resolving the amount of contamination in environmental studies.

In the MT method, there may be surficial, small-scale 3-D anomalies that may cause unwanted galvanic currents. These anomalies may obscure the regional 2-D structure by disrupting the electric field. The MT impedance tensor is affected by this situation. Although the medium is generally 2-D, the measured impedance tensor may exhibit 3-D behavior due to local frequency-independent telluric distortions. No significant 2-D interpretation can be made with the data measured due to this effect. "Decomposition" is performed to remove the effect of small-scale 3-D structures from the data.

Common methods used to perform dimensionality analysis are performed with Swift's skew (Swift, 1967), Bahr parametrization (Bahr, 1988; Bahr, 1991), Groom and Bailey decomposition (Groom and Bailey, 1989; McNeice and Jones, 2001) and phase tensor analysis (Caldwell et al., 2004).

2.7.1. Swift's Skew and Bahr's Parameters

A 2-D measure can be constructed from the elements of the impedance tensor to analyze whether the 2-D interpretation is possible or not. The Swift's skew (κ) parameter is the ratio of the addition of the diagonal impedance tensor elements to

difference of the off- diagonal impedance tensor elements (Swift, 1967).

$$\kappa = \frac{Z_{xx} + Z_{yy}}{Z_{xy} - Z_{yx}} \qquad (2.30)$$

where κ is a rotationally invariant tensor (Bahr, 1991), and it's also said to be the skewness parameter. According to Ledo (2002), when the skew value is less than or equal to 0.1 ($\kappa \leq 0.1$) the medium is 1-D. If the skew value is more than 0.3 ($0.3 < \kappa$), in that case, the medium is 3-D.

On the other hand, Bahr (1991) has some dimensionality parameters to interpret the medium which is related to the components of the impedance tensor.

$$\mu = \frac{(|[D_1, S_2]| + |[S_1, D_2]|)^{\frac{1}{2}}}{|D_2|} \qquad (2.31)$$

In the above equation, μ is said to be a one-dimensional parameter.

$$S_1 = Z_{xx} + Z_{yy} \qquad (2.32)$$

$$S_2 = Z_{xy} + Z_{yx} \qquad (2.33)$$

$$D_1 = Z_{xx} - Z_{yy} \qquad (2.34)$$

$$D_2 = Z_{xy} + Z_{yx} \qquad (2.35)$$

and,

$$[D_1, S_2] = \text{Im}(S_2 D_1^*) = \text{Re}(D_1)\,\text{Im}(S_2) - \text{Re}(S_2)\,\text{Im}(D_1) \qquad (2.36)$$

$$[S_1, D_2] = \text{Im}(D_2 S_1^*) = \text{Re}(S_1)\,\text{Im}(D_2) - \text{Re}(D_2)\,\text{Im}(S_1) \qquad (2.37)$$

where * indicates the complex conjugate.

There are two options in that parameter. If the value equals zero ($\mu \approx 0$) the medium is 1-D, otherwise, the medium is 2-D or 3-D. When ($\mu \approx 0$) the impedance tensor generates 5 parameters: common phase of all the tensor elements and multiples of the four distortion matrix elements (Bahr, 1991).

When the parameter D cannot be resolved from the tensor, it is referred to as static shift.

$$\eta = \frac{(|[D_1, S_2]| - |[S_1, D_2]|)^{\frac{1}{2}}}{|D_2|} \qquad (2.38)$$

Regional skew (η) is another value that is defined by Bahr (1991). It is completely related to the 2-D or 3-D features of the medium. If $\eta = 0$, the medium is 2-D. Once $\eta > 0.3$, the medium becomes 3-D.

The last one is Σ. This parameter represents that the medium is 2-D once its value is greater than 0.1, $\Sigma > 0.1$,

$$\Sigma = \frac{(D_{12} + S_{22})}{D_{22}}. \qquad (2.39)$$

2.7.2. Phase Tensor

The MT phase tensor (Φ) expresses how the polarization and phase relations change in a medium where the conductivity structure is 3-D (Caldwell et al., 2004). The information obtained is not affected by galvanic distortion in the region.

$$\mathbf{Z} = \mathbf{D}_A \cdot \mathbf{Z}_R \qquad (2.40)$$

$$\mathbf{Z} = \mathbf{X} + i\mathbf{Y} \qquad (2.41)$$

where D_A is the 2×2 distortion matrix and the regional field is represented by an R in the index. We can present the relationship between distorted and regional impedance tensors as follows.

Definition of the phase tensor is

$$\Phi = \mathbf{X}^{-1}\mathbf{Y} \qquad (2.42)$$

where $\mathbf{X}^{-1}$ is the inverse of the real impedance tensor and $\mathbf{Y}$ is the imaginary part of it.

$$\Phi = (\mathbf{D}_A X_R)^{-1}(\mathbf{D}_A Y_R) = X_R^{-1}\mathbf{D}_A^{-1}\mathbf{D}_A Y_R = X_R^{-1}Y_R = \Phi_R \qquad (2.43)$$

It means that observed and regional phase tensors are the same and distortion-free. Real and imaginary components of the impedance tensor can be used to write the phase tensor as a matrix (Caldwell et al., 2004).

$$\begin{bmatrix} \Phi_{11} & \Phi_{12} \\ \Phi_{21} & \Phi_{22} \end{bmatrix} = \frac{1}{|X|} \begin{bmatrix} X_{22}Y_{11} - X_{12}Y_{21} & X_{22}Y_{12} - X_{12}Y_{22} \\ X_{11}Y_{21} - X_{21}Y_{11} & X_{11}Y_{22} - X_{21}Y_{12} \end{bmatrix} \qquad (2.44)$$

where $|X|$ is the determinant of the X. Caldwell et al. (2004) presents phase tensor as a representative ellipse (Figure 2.4). This ellipse consists of algebraically described four elements of phase tensor which are the minimum (Φ_{min}) and maximum (Φ_{max}) tensor values, the skew angle (β) and the non-invariant angle (α).

$$\text{tr}(\Phi) = \Phi_{11} + \Phi_{22} \qquad (2.45)$$

$$\text{sk}(\Phi) = \Phi_{12} - \Phi_{21} \qquad (2.46)$$

$$\det(\Phi) = \Phi_{11}\Phi_{22} - \Phi_{12}\Phi_{21} \qquad (2.47)$$

the all invariants that define the ellipse are

$$\Phi_1 = \frac{\text{tr}(\Phi)}{2} \qquad (2.48)$$

$$\Phi_2 = \det(\Phi)^{\frac{1}{2}} \tag{2.49}$$

$$\Phi_3 = \frac{\text{sk}(\Phi)}{2} \tag{2.50}$$

The skew angle $\beta = \frac{1}{2}\tan^{-1}\left(\frac{\Phi_{12}-\Phi_{21}}{\Phi_{11}+\Phi_{22}}\right)$ and non-invariant angle $\alpha = \frac{1}{2}\tan^{-1}\left(\frac{\Phi_{12}+\Phi_{21}}{\Phi_{11}-\Phi_{22}}\right)$, where

$$\Phi_{min} = (\Phi_{12} + \Phi_{23})^{\frac{1}{2}} - (\Phi_{12} + \Phi_{23} - \Phi_{22})^{\frac{1}{2}} \tag{2.51}$$

$$\Phi_{max} = (\Phi_{12} + \Phi_{23})^{\frac{1}{2}} + (\Phi_{12} + \Phi_{23} - \Phi_{22})^{\frac{1}{2}} \tag{2.52}$$
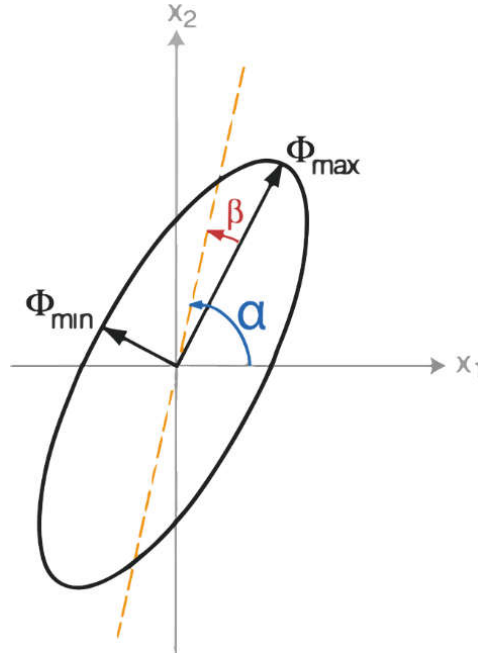
Figure 2.4. Graphical representation of the phase tensor ellipse and its invariants β, α, Φ_{min} and Φ_{max}, where x_1 and x_2 are the coordinate reference frame. (Taken from Caldwell et al., 2004)

If the medium is isotropic homogeneous then β equals zero, the phase tensor ellipses are nearly a circle. In a 2-D case, the phase tensor is symmetric and α represents the strike direction. When the media begins to have a 2-D or 3-D conductivity distribution, the ellipses begin to elongate in the direction of the strike. As the values of β get larger, the 3-D features of the medium increase. This is an indication of the three-dimensional resistivity structure. Phase tensors can be represented by ellipses, and the strike direction is given by $\alpha - \beta$. (Caldwell et al., 2004).

3. GEOLOGICAL AND TECTONIC SETTINGS OF THE STUDY AREA

Anatolia has a complex geological history and was formed as a result of tectonic processes that have been going on for millions of years. Frequent earthquakes and volcanoes all around Anatolia show that these processes are still active. Anatolia lies between two ancient continents, the continent of Laurasia in the north which manifests itself as Eurasia of today and the former continent of Gondwana, representing Africa-Arabia in the south. During the Paleozoic-Early Tertiary, the Neo-Tethys Ocean was aligned approximately east- west between Eurasia and Gondwana (Şengör and Yılmaz, 1981).

Anatolia consists of the amalgamation of some continental fragments that were separated from the main continents of Eurasia and Gondwana (Göncüoğlu, 2010). During the Paleozoic and Mesozoic periods, the continental parts of Gondwana separated from the continental margin, moved north, and added to the Eurasian continent. The parts that makeup Anatolia came together in the Mesozoic and Cenozoic, and Anatolia attained its present shape in the Oligo-Miocene. (Şengör and Yılmaz, 1981; Okay and Tüysüz, 1999). As a result of these complex geological processes, it is possible to observe both igneous and sedimentary rocks, accretionary wedge and ophiolitic series in Turkey (Okay, 2008).

In general, it is possible to analyze the tectonics of Anatolia by dividing it into three headings: The Pontides, the Anatolide – Taurides block (ATB), and Arabian platform (from north to south) (Okay, 2008. Figure 3.1). The Pontides are Paleozoic-aged fold and thrust belts which are essential in the African-Eurasian convergence and represented by the evolution of the Neo-Tethys and the Paleo-Tethys oceans (Şengör and Yılmaz 1981, Meijers et al., 2010).

The Neo-Tethys Ocean is the last closed ocean between Eurasia and Gondwana, of the late Paleozoic to early Cenozoic ages (Zhu et al., 2021). The Pontides consist of three zones separated from each other along tectonic lines:

- the Western Pontides (The Strandja Massif, İstanbul Zone and the Sakarya Zone),
- the Central Pontides,
- the Eastern Pontides (Yılmaz et al., 1997).

Another important structure, the ATB (such as Tavşanlı zone and İzmir-Ankara-Erzincan Suture Zone (İAES)), collides with the Pontides in the early-late Eocene interval, and the two belt are separated from each other by the IAES (Şengör and Yılmaz, 1981). It is a tectonic structure extending along a line from the Aegean Sea in the west down to Iran in the east. During the middle Cretaceous, subduction zones and mélange structures emerged, and the ATB underwent a high pressure and low-temperature metamorphosis (Okay, 2008). This block is divided into many subsections because they show different structural and stratigraphic features. ATB is more similar to the Arabian plate than the Pontides in terms of their stratigraphic features. The third block is the Arabian Platform which is located at the southeast of Anatolia and is separated from the ATB by the Assyrian suture belt. The Arabian platform was separated by a part of the Neo - Tethys Ocean and the ATB during the Phanerozoic. Cretaceous-aged and younger structures are exposed throughout Southeastern Anatolia (Okay, 2008).
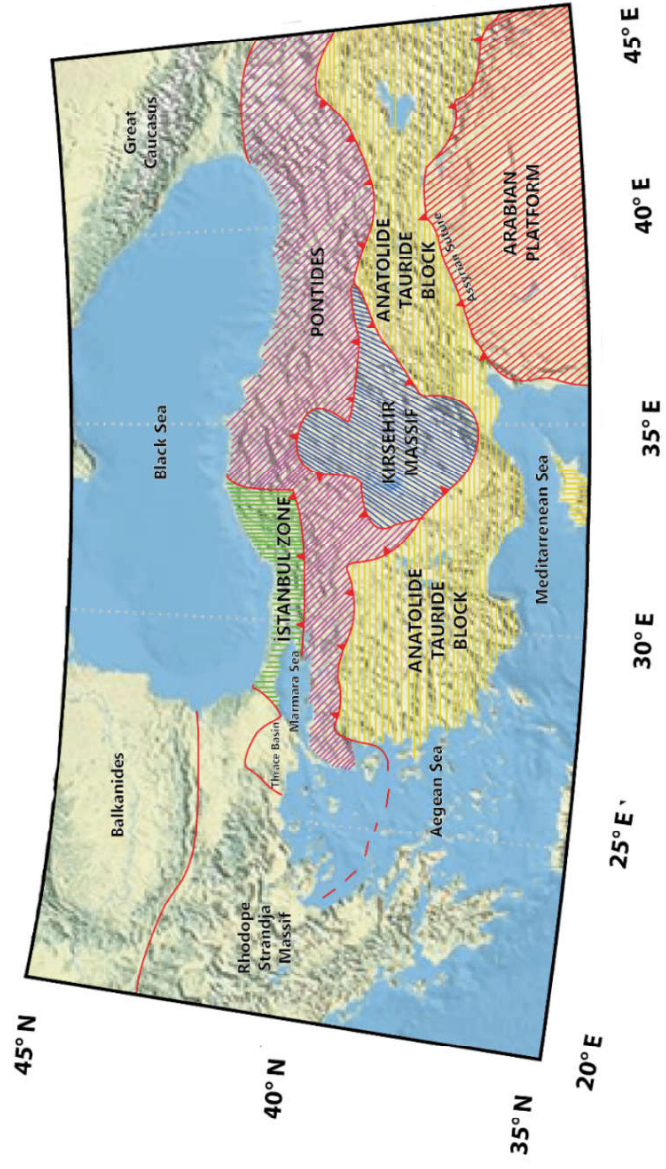
Figure 3.1. Main tectonic units of Anatolia (modified from Okay and Tüysüz, 1999)

Anatolia is a region where the Earth's crust is very active, and earthquakes occur frequently. According to Bozkurt (2001), the NAF, East Anatolian Fault (EAF), Aegean- Cyprian Arc (ACA) and the Dead Sea Transform Fault (DSTF) have an essential position in the active tectonics of Anatolia that started in the Early Pliocene (5 Ma). NAF is about a 1200 km long, right-lateral strike-slip fault zone extending from the Karlıova triple junction to the Aegean Sea (Şengör et al., 2005; Faccenna et al., 2006). NAF has many second-order strike-slip faults or auxiliary fault zones, and CAFZ is one of them (Dirik, 2001). CAFZ is a NE-SW-trending, 730 km long, a sinistral strike slip structure located in the eastern part of CA (Dirik, 2001; Koçyiğit and Erol, 2001). On the other hand, the CAF is seismically active and has a rate of motion of about 0.3 cm/year (Koçyiğit and Beyhan, 1998). The northeastern and southwestern parts of this fault zone relate to the Erciyes basin, which is approximately northeast-southwest oriented and one of the largest and most developed structures of the CAF (Koçyiğit and Erol, 2001). The boundary of the EEB is determined from west to east by the Yeşilhisar and Develi normal faults, respectively (Higgins et al., 2015). Faults surrounding the region have produced earthquakes before and seismicity analysis has been made (Koçyiğit and Erol, 2001). Figure 3.2 was drawn by using KOERI data to obtain information about the activity of these faults. Mt. Erciyes stratovolcano is also located in this area. EEB divided by ESC and consists of the Sultansazlığı and Kayseri-Sarımsaklı depressions (Bozkurt, 2001). Considering the lithological changes of the ESC in vertical and horizontal directions, the unit was divided into members by Pasquare (1968) from bottom to top. These are basaltic and andesitic lavas, dacitic rhyodacitic lava domes, olivine basalt lava, hyalodacitic lava domes, and pumice ash deposits.
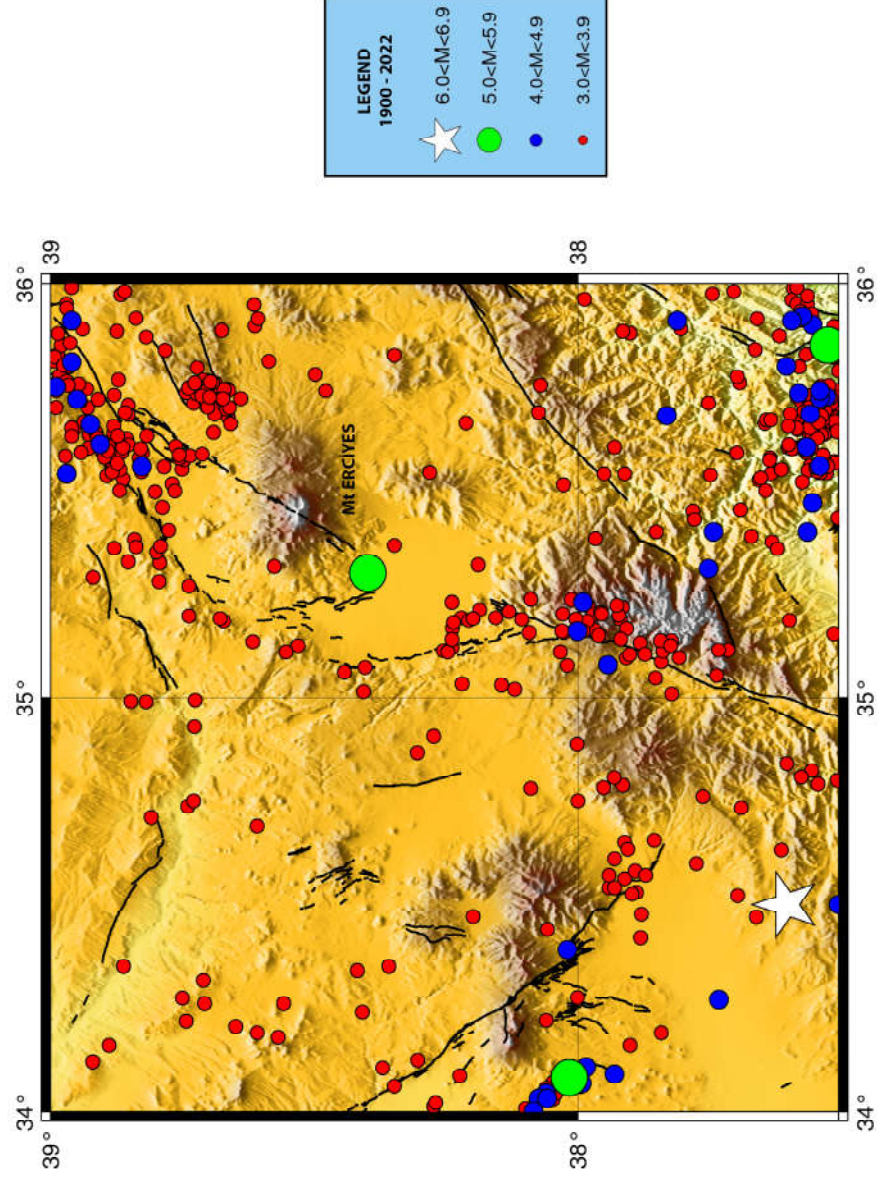
Figure 3.2. Earthquake dataset $M \geq 3.0$ map from $1900 - 2022$. The colored dots and the star symbolize earthquakes of different magnitudes. Earthquake data is taken from KOERI.

CA embodies countless large and small faults, a pull-apart basin, and many volcanoes (Koçyiğit and Erol, 2001; Aktuğ et al., 2013). EFZ, EEB and Mt. Erciyes are some of the essential tectonic structures found in this region. Mt. Erciyes, one of the major volcanoes of CA, (38.53°N 35.45°E, 3917 m) is a stratovolcano and located approximately 15 km south of Kayseri (Figure 3.3). The stratigraphy of Mt. Erciyes was investigated by Şen et al. (2003), and it was documented that Mt. Erciyes has at least 64 monogenetic vents. This volcano produced pyroclastic deposits and lava flows during its evolution (Kürkçüoğlu et al., 1998). Most of these products are calc-alkaline (include volcanic types such as basalt, andesite, dacite and rhyolite) and they constitute the Koç Dağ and the New Erciyes sequences. The Koç Dağ and the New Erciyes are two volcanological evolution stages of Mt. Erciyes from Pliocene to Quaternary (Şen et al., 2003). The Koç Dağ constitutes the eastern part of the volcano, and mainly composed of alkali basalt, andesite, and basaltic andesite lava flows (Kürkçüoğlu et al., 1998). According to Innocenti et al. (1975), the first eruption of the Erciyes stage occurred with the eruption known as the Valibabatepe ignimbrite eruption (VTI) (2.8 Ma Innocenti et al. (1975), 2.73 Ma Higgins et al. (2015), and 2.5 Ma Çiner and Aydar (2019)). As a result of this explosion, a caldera collapse occurred. The Erciyes stage consists of different basaltic-andesitic, andesitic, dacitic, rhyodacitic lava generations, and associated pyroclastics (Kürkçüoğlu et al., 1998). Two eruptive stages resulted in the formation of the Mt. Erciyes. An effusive-extrusive and a second extrusive-explosive cycle contributed to the evolution of this stage (Aydar et al. 2019). It is easy to distinguish differences in the phases by scoria fall and mudflow deposits (Şen et al., 2003). Late Holocene-aged volcanic products were not encountered (Aydar et al., 2019).
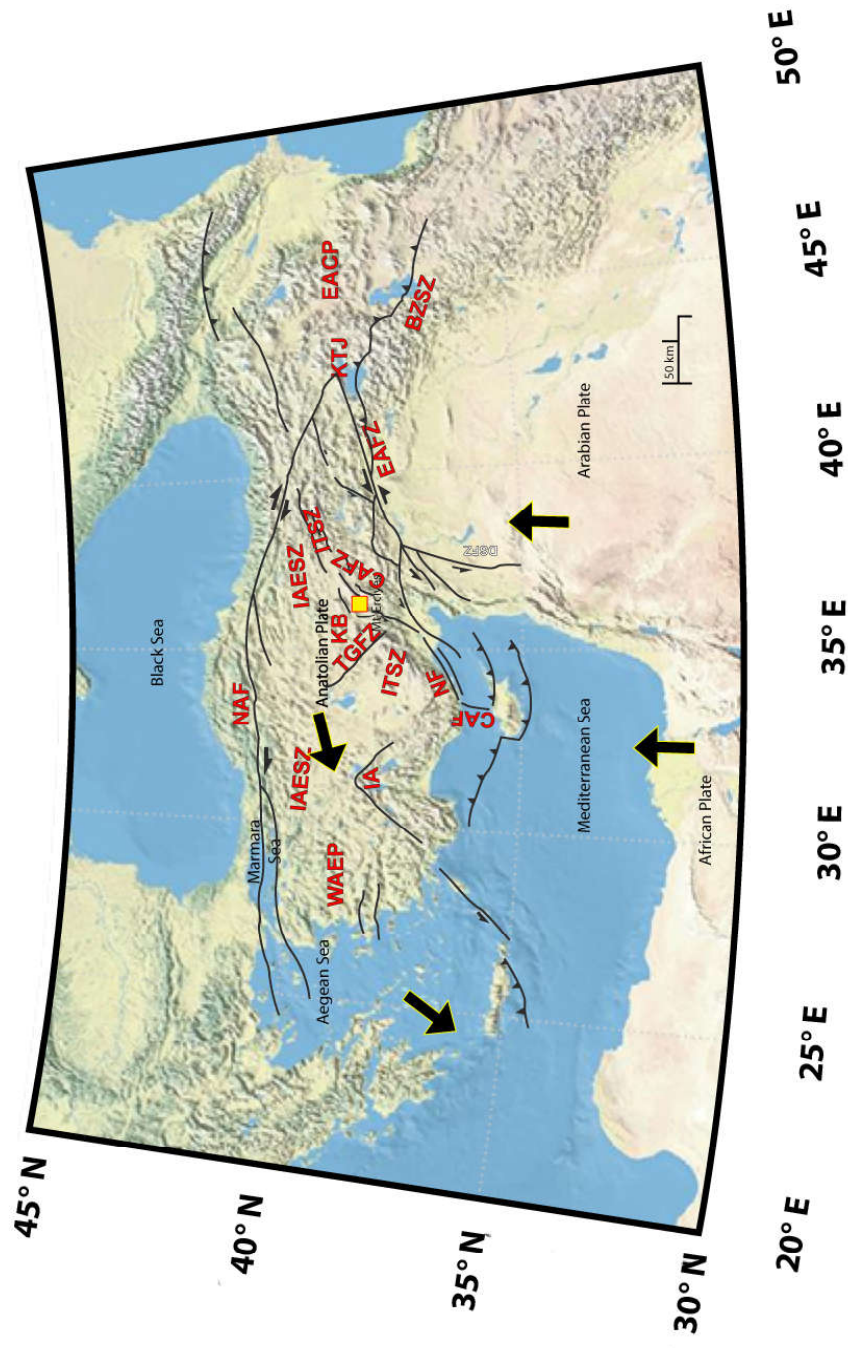
Figure 3.3. Tectonic setting of Turkey edited from Higgins et al. (2015). Large black arrows give information about the direction of movement of the plates. The black lines symbolize the main plate boundaries and auxuliary tectonic structures responsible for the tectonics of Anatolia. The yellow square indicates the study area that this thesis is examining.

The glaciation of mountains in Turkey belonged to the Late Quaternary (Sarıkaya et al., 2009). Mt. Erciyes is one of the mountains that still has glaciers. During the Late Pleistocene-Early Holocene times was produced glacial erosion characteristics (horn, arete, cirque) and deposits (moraines) in crustal surface above-2700 m in the Mt. Erciyes (Koçyiğit and Erol, 2001). Mt. Erciyes consists of five valleys, two of which are considered as the main ones (Aksu and Üçker valleys), and the rest are relatively smaller valleys (Öksüzdere, Saraycık, and Topaktaş valleys) (Sarıkaya et al., 2009). Öksüzdere, Topaktaş and Saraycık valleys are located in the northeast, south, and southwest of the mountain, respectively. Although these valleys have glacial deposits as in other valleys, the extent of glaciation is relatively small. Besides, Aksu Valley involves an active glacier and Üçker Valley involves a rock glacier (Güner and Emre, 1983).

4. MEASURING THE STRIKE

4.1. Geological Methods

When describing many geological structures, their plane is mentioned, such as an oblique- slip fault or sedimentary bedding. Strike and dip are two related and essential geological terms that are closely related to the plane of structures. Geologists use the concepts of strike and dip relative to the horizontal plane when describing the deformation of rock layers due to bending or breaking.

To talk about strike and dip, we need to mention a planar structure, such as joints, fault lines, dykes, sills, and the foliation planes in metamorphic rocks (Panchuk, 2019). The strike is the direction of a line formed by the intersection of the surface with a horizontal plane (Lahee, 1923). In such a case, it would be hard to define a strike for a horizontal plane. The strike value is determined by measuring the angle that the plane on which the compass rests makes with the north. The dip is the deviation of an inclined surface from the horizontal and should be measured perpendicular to the strike direction (Monroe et al., 2007). The east or west edge of the compass rests on the planar structure to be measured, and the compass base is horizontal. The strike angle is the acute angle the compass makes with the north. The angle showing the direction value gives the strike direction.

To measure the angle of dip, the south or north side of the compass leans parallel to the compass direction. If the south direction is leaned north, if the north direction is leaned south gives us the dip direction. The edge of the compass leans perpendicular to the plane line. The value indicated by the moving pendulum inside the compass is measured as the dip angle (Coe, 2010).

Please note that both strike and dip values are measured utilizing the plane on which the compass rests.

4.2. The Geoelectric Strike

The geoelectric strike is one of the crucial definitions for MT. In a 2-D situation, where the resistivity changes with depth and in one horizontal direction but remains constant in the other horizontal direction, in which the resistivity is constant is called geo-electric strike. (Khyzhnyak, 2014, Maulinadya and Grandis, 2019). Due to lateral inhomogeneity of electrical conductivity on Earth, the geoelectric strike is a direction that represents the orientation of electric current flow in the subsurface (Niasari, 2016). The geoelectric strike is of great importance in modeling resistivity data due to the variety of area of utilization. Determination of geothermal reservoir boundaries and evaluation of fractures and faults at various depths that are flow paths for the geothermal fluid are some of the uses of strike analysis (Khyzhnyak, 2014).

Rotational analysis of the MT impedance tensor can be used to calculate the geo-electric strike angle (Maulinadya and Grandis, 2019). When off-diagonal elements in a 2-D environment are parallel to the geo-electric strike direction the impedance tensor is,

$$\mathbf{Z} = \begin{bmatrix} 0 & Z_{xy} \\ Z_{yx} & 0 \end{bmatrix} \tag{4.1}$$

Vozoff (1972) states the geo-electric strike as follows,

$$\tan(4\theta_0) = \frac{(Z_{xx} - Z_{yy})(Z_{xy} + Z_{yx})^* + (Z_{xx} + Z_{yy})^*(Z_{xy} + Z_{yx})}{|Z_{xx} - Z_{yy}|^2 - |Z_{xy} + Z_{yx}|^2} \tag{4.2}$$

where * indicates the complex conjugate.

In the MT method, the components of the electric field (E_x, E_y) and the magnetic field (H_x, H_y, H_z) are measured. In a 2-D case, the impedance tensor is split into two modes: the case where the x-axis is parallel to the strike and the y-axis is perpendicular to the strike and vice versa. If the electric field is parallel to the strike, it represents

transverse electric mode (TE), if the strike is parallel to the magnetic field, it is called transverse magnetic mode (TM) (Maulinadya and Grandis, 2019). It is possible to call them **E**-polarization and **B**-polarization. In the TE mode, E_x , where the electric field is parallel to the geological direction, and the magnetic field components H_y and H_z, which are perpendicular to this component, are measured. Similarly, in the TM mode, H_x, perpendicular to the geological direction and E_y perpendicular to this component are measured as follows:
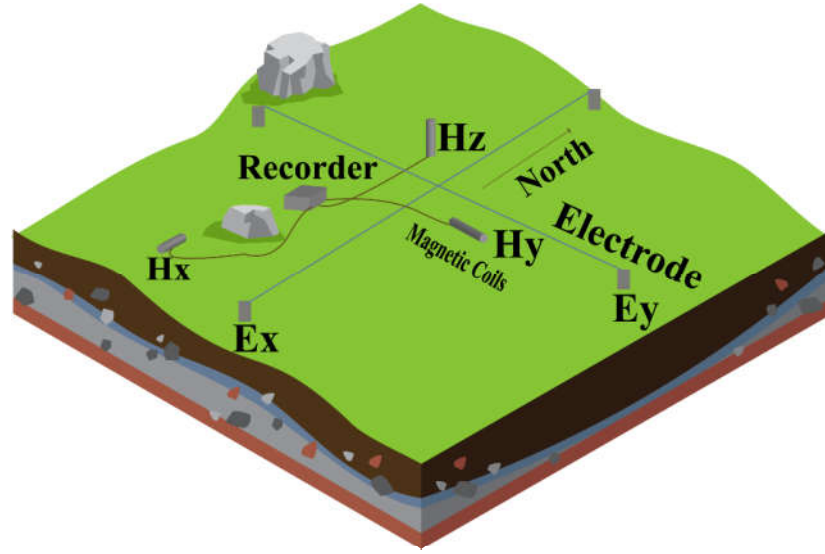
Figure 4.1. Pieces of equipment of an MT installation site. (Recorder, electrodes, and magnetic coils.

Simpson and Bahr (2005) say that 90° turns mean the rotation of the two main impedance tensor components inside the tensor. This means that the calculated strike direction has an ambiguity of 90°.The mathematical expression is as follows:

$$(\overset{\beta}{=}90)\begin{pmatrix} 0 & Z_{xy} \\ Z_{yx} & 0 \end{pmatrix}(\overset{\beta}{=}90)^T = \begin{pmatrix} 0 & 1 \\ -1 & 0 \end{pmatrix}\begin{pmatrix} 0 & Z_{xy} \\ Z_{yx} & 0 \end{pmatrix}\begin{pmatrix} 0 & -1 \\ 1 & 0 \end{pmatrix} = \begin{pmatrix} 0 & -Z_{yx} \\ -Z_{xy} & 0 \end{pmatrix} \qquad (4.3)$$

When reading the rose diagrams obtained as a result of the strike analysis, 90° should be subtracted and read.

4.3. Magnetotelluric Data Acquisition

The data for this thesis study were collected through three separate field studies. To understand the deep electrical resistivity structure of the study area, measurements were made along the profiles enclosing Mt. Erciyes and surrounding the complex it is in to conduct a wide- band MT study.

During this study two Phoenix Geophysics (MTU-5A) systems were used (Figure 4.2.). Horizontal components of the electric field were measured (E_x and E_y) with non-polarizing electrodes containing Pb-PbCl$_2$ solution. Magnetic measurements were performed with three magnetic coils (MTC-50).

Figure 4.2. Phoenix Geophysics MTU-5A. a is an MT recorder. The GPS antenna is indicated by b. The letters c and d denote magnetic coils and electrodes, respectively (This photo was taken from the Phoenix Geophysics official page. July, 2022).

During the establishment of the sounding stations, it was carefully studied so that the measurements were not affected by noise. All electrodes are embedded and recording devices are stored in boxes to reduce noise impact and ensure safety. The vertical component of the magnetic field can be used to generate the tipper data. Since the study area is a volcanic complex, the magnetic coils could not be buried deep enough and were affected by the noise. Therefore, it was not included in this study.

5. MODELING

The modeling process consists of two steps;

i. forward relation,

ii. inversion.

$$\mathbf{D}_p = F(\mathbf{m}) \tag{5.1}$$

$\mathbf{D}_p$ represents the predicted data set, and $\mathbf{m}$ represents the model parameters. F is an operator that establishes a relationship between the model and the dataset. According to Menke (1984), observed data ($\mathbf{d}$) is presented as vectors with a length of N. Similarly, model parameters ($\mathbf{m}$) can be presented as vectors with a length of M,

- data: $\mathbf{d} = \begin{bmatrix} d_1 & d_2 & d_3 & ... & d_N \end{bmatrix}^T$
- model: $\mathbf{m} = \begin{bmatrix} m_1 & m_2 & m_3 & ... & m_M \end{bmatrix}^T$

where T represents the transpose of the matrix. The final form of inversion as follows with an error (e) option,

$$F(\mathbf{d}, \mathbf{m}) = \mathbf{d} - F(\mathbf{m}) + e \tag{5.2}$$

The modeling process of the obtained data is the most crucial stage in this study. MT modeling aims to calculate the obtained true resistivity distribution as accurately as possible and to obtain the most statistically suitable model of the subsurface. The Earth has a very complex structure, and the aim of modeling is to illustrate the geological structure in a realistic way by using geophysical data. Geophysical data is used as a model parameter, and a simple model is used to obtain the geological structure.

This process is called inverse modeling.

According to Menke (1984), the inverse problem for a linear case ($F(\mathbf{m}) = G\mathbf{m}$) can be calculated as follows ,

$$E = e^T e = (\mathbf{d} - G\mathbf{m})^T(\mathbf{d} - G\mathbf{m}) = \sum_{i=1}^{N} \left[d_i - \sum_{j=1}^{M} G_{ij} m_j \right] \left[d_i - \sum_{k=1}^{M} G_{ik} m_k \right] \quad (5.3)$$

If the derivative of E with respect to m is calculated term by term, first term gives,

$$\frac{\partial}{\partial m_q} \left[\sum_{j=1}^{M} \sum_{k=1}^{M} m_j m_k \sum_{i=1}^{N} G_{ij} G_{jk} \right] = \sum_{j=1}^{M} \sum_{k=1}^{M} [\delta_{jq} m_k + m_j \delta_{kq}] \sum_{i=1}^{N} G_{ij} G_{jk} = 2 \sum_{k_1}^{M} m_k \sum_{i=1}^{N} G_{iq} G_{ik}.$$
$$(5.4)$$

Second term gives,

$$-2\frac{\partial}{\partial m_q} \left[\sum_{j=1}^{M} m_j \sum_{i=1}^{N} G_{ji} d_i \right] = -2 \sum_{j=1}^{M} \delta_{jq} \sum_{i=1}^{N} G_{ji} d_i = -2 \sum_{i=1}^{N} G_{iq} d_i \quad (5.5)$$

Third term gives zero because it does not contain $\mathbf{m}$,

$$\frac{\partial}{\partial m_q} \sum_{i=1}^{N} d_i d_i = 0 \quad (5.6)$$

The sum of the three terms is as follows,

$$\frac{\partial E}{\partial m_q} = 0 = 2 \sum_{k=1}^{M} m_k \sum_{i=1}^{N} G_{iq} G_{ik} - 2 \sum_{i=1}^{N} G_{iq} d_i \quad (5.7)$$

As matrix notation yields,

$$G^T G\mathbf{m} - G^T \mathbf{d} = 0. \tag{5.8}$$

A vector of length $\mathbf{m}$ is multiplied by the square matrix $G^T G$. Due to unknown model parameters, this problem is square matrix equation (Menke, 1984).

$$\mathbf{m}_{est} = \left[G^T G\right]^{-1} G^T \mathbf{d} \tag{5.9}$$

which is the least-squares solution to the inverse problem $G\mathbf{m} = \mathbf{d}$.

The data obtained as a result of the measurements can be interpreted by modeling 2- D and 3-D. With 2-D modeling, sufficient information can be provided about changes in the crustal structure and faults. The finite difference method and the finite element method are the two most used methods for the 2-D MT modeling process. Siripunvaraporn (2012) states that, 3-D modeling has many advantages over 2-D modeling:

    i. The main reason for the need for 3-D inversion is that 3-D makes it easy to explain the three-dimensional world.

    ii. Dimensionality analysis is required for 2-D inversion, but it is a great advantage that dimensional analysis is not a crucial requirement for 3-D.

    iii. For 2-D inversion, it is necessary to measure along the entire MT profile line specified. There is no such requirement for 3-D, measured data from scattered stations can be used for inversion.

The algorithm used for the 3-D models obtained in this study is MoDEM© which is based on non-linear conjugate gradients (NLCG) algorithms (Egbert and Kelbert, 2012; Kelbert et al., 2014). The MoDEM© uses both the real and the imaginary part of the impedance tensor and can benefit from the tipper information. For this

algorithm, penalty functional (Φ) is expressed in form:

$$\Phi(\mathbf{m}, \mathbf{d}) = (\mathbf{d} - F(\mathbf{m}))^T C_d^{-1} (\mathbf{d} - F(\mathbf{m})) + v(\mathbf{m} - \mathbf{m}_0)^T C_m^{-1}(\mathbf{m} - \mathbf{m}_0) \qquad (5.10)$$

where C_d is the covariance of the data errors, $\mathbf{m}_0$ is the prior values for the model parameters and C_m (or more properly $v^{-1}C_m$) is the model covariance or regularization term. During the modeling process MODEM $^{©}$ efforts to minimize the penalty function for solving regularized EM inverse problems (Kelbert et al., 2014).

5.1. Inversion of the MT Data

The first step in the inversion process is to create a regional model that fits the data substantially. Inversion algorithm, MODEM $^{©}$ developed by Egbert and Kelbert (2012) and Kelbert et al. (2014) was utilized for the inversions of all four elements of the electromagnetic impedance tensor (Z_{xx}, Z_{xy}, Z_{yx}, and Z_{yy}). For the model, which included the topography information, the topography data were obtained from ETOPO1 (NOAA–National Centers for Environmental Information). For both regional models, 38 wide-band MT stations out of 48 were used to focus beneath the volcano. The resistivity of the initial model was chosen as 100 Ωm. For the without topography model the total numbers of cells in X-Y-Z directions were $100 \times 100 \times 30$, respectively. The final regional inversion scheme for this model merged into a model with an RMS of 3.85 at the end of the 84th iteration. The number of cells is higher for the model containing topography information, in X-Y-Z directions were $99 \times 81 \times 110$ (30 out of 110 are air layers), respectively. The nodes of the mesh are designed to prevent the stations on the mesh elements from colliding with each other, and the cell size of the center of the model is chosen as 2.5 km. (Figures 5.1 and 5.2). The final regional inversion scheme for this model merged into a model with an RMS of 3.07 at the end of the 110th iteration. To observe whether the lack of topography affected the final model, both topography and non-topography models were calculated and compared (Figures 6.14 and 6.15). The fitting curves of the topography model can be seen in Appendix B. When examined in general, the regional resistivity distribution has acceptable fitting rates.
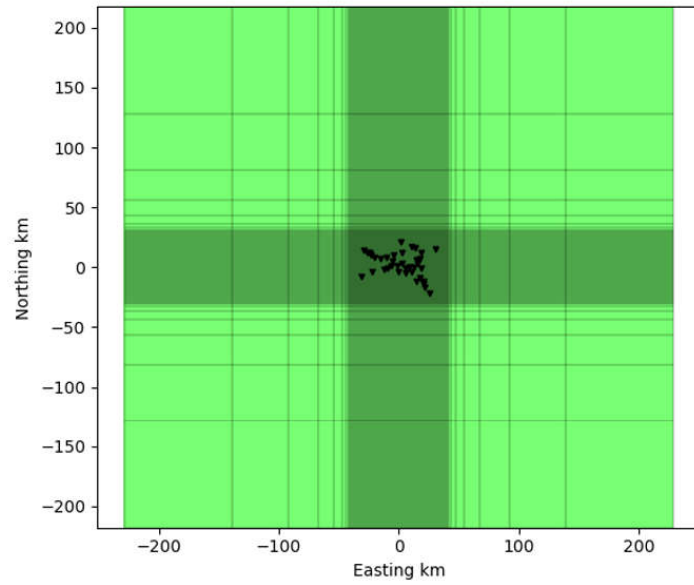
Figure 5.1. The initial model (without topography) of the 3-D modeling scheme of Mt. Erciyes the section is the view from the top where black triangles indicate the MT stations.
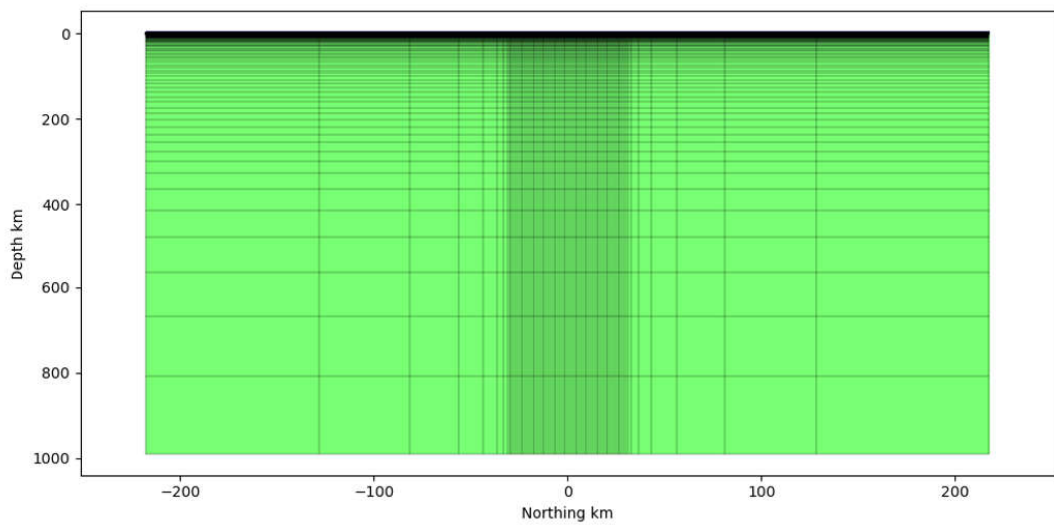
Figure 5.2. The initial model (without topography) of the 3-D modeling scheme of Mt. Erciyes as a cross-section.

5.2. Sensitivity Tests

After obtaining the final model of the data used, sensitivity tests were performed to check the accuracy of the results and the validity of some anomalies. The tests were performed by drawing resistive anomalies on the conductors in the obtained models to check the reliability of the modeling results.

For MODEM $^{©}$ results, the sensitivity tests made to cover all C1, C2, C3, and C4 conductors aimed to examine the deep conductor up to approximately 5 km (Figure 5.3). These four anomalies were masked with a $100\Omega m$ value. When an artificial anomaly was added to the region, the RMS value gradually increased from 3.07 to 4.6. It can be said that considering the test results, the model is sensitive to this anomaly at the tested depths.

Figure 5.3. The map indicates sensitivity tests and the injection methodology for conductive anomalies beneath Mt Erciyes.

6. RESULTS AND INTERPRETATION

In this study, the electrical resistivity structure beneath Mt. Erciyes is revealed by a 3-D model of high-resolution wide-band MT data. Wide-band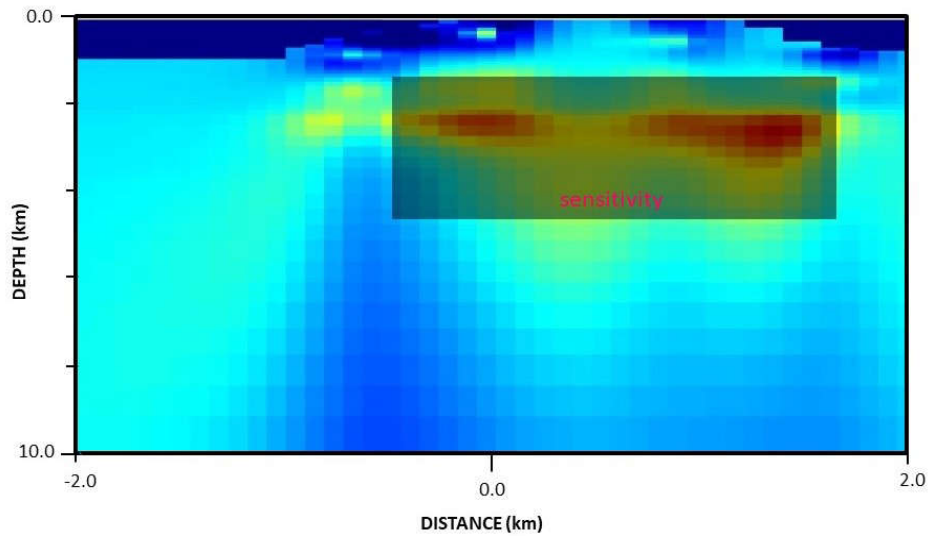 MT data were collected from the east and west of Mt. Erciyes and in the form of a profile surrounding the caldera of the Koç Dağ. The study area has been previously investigated with geological and geophysical techniques that were applied by various researchers at various times. The current study is an original work that aims to examine the electrical resistivity structure beneath the Mt. Erciyes using 3-D MT method.

Since there is no structural strike information that measured in the fieldwork, the strike value of Higgins et al. (2015) is used to compare the results (Figure 6.1). This value states that the dominant azimuth direction of the region is 25° to 35°. Rose diagrams of each decade are given separately for all sounding stations in Figure 6.2. The dominant direction changes calculated from different frequency bands (changing between 10^{-3} 10^4 Hz) and phase tensors are shown this figure. It is possible to obtain values in less or more range in the desired frequency band. The uncertainty in the angles is not considered. Figure 6.3 presents two different strike values as a result and interprets the overall orientations in the desired frequency band for the study region. Both of them were calculated by EM data collected from the fieldwork. The first diagram (Strike Z) is established by using Swift's methods, and the second one (PT Azimuth) is calculated by Caldwell's method.
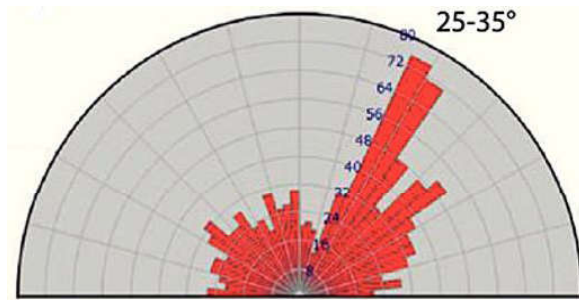
Figure 6.1. Rose diagram presentation of the geological direction of the study area, which Higgins et al. (2015) obtained in the study area by geological methods.
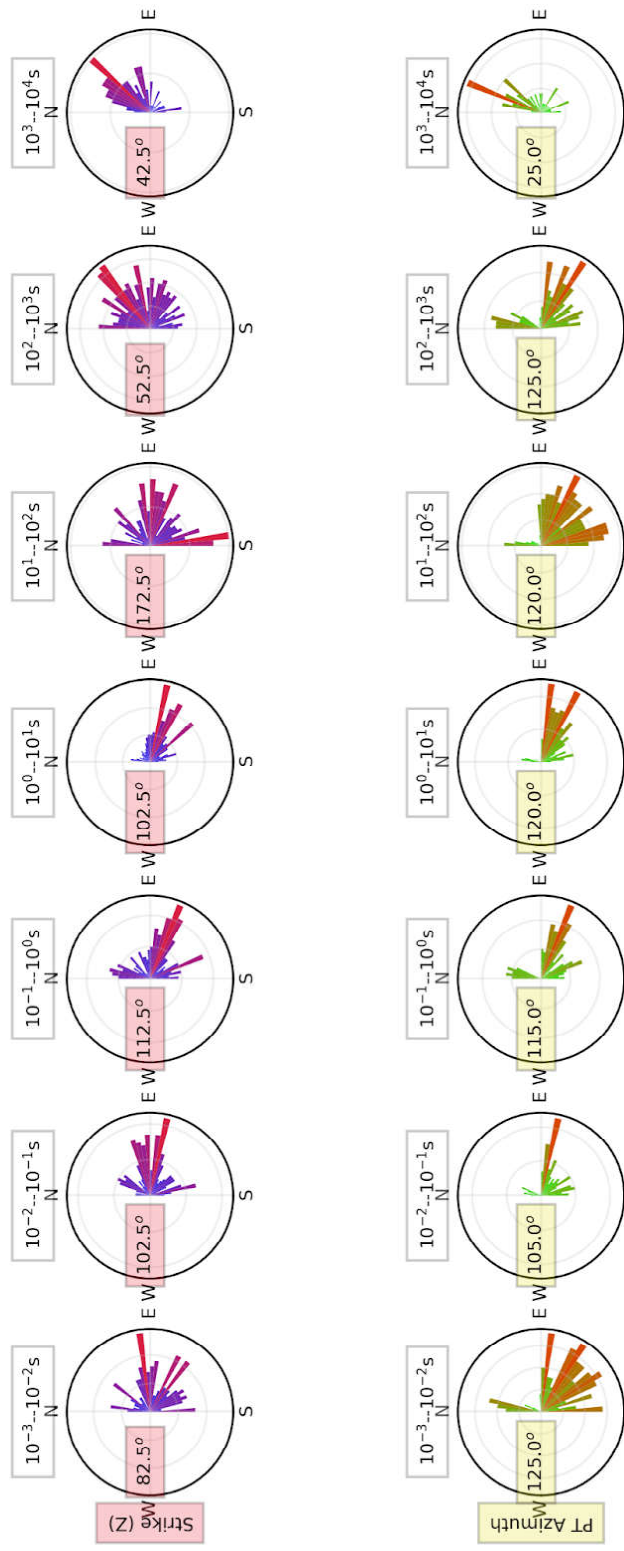
Figure 6.2. Rose diagrams representation of geo-electric strike for wide-band MT data.
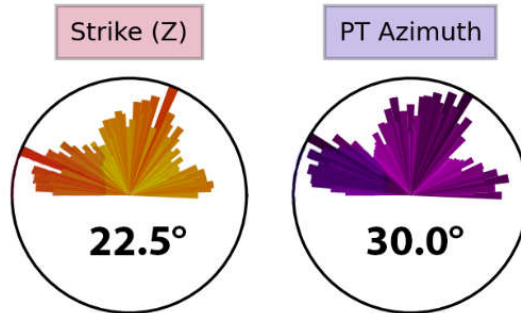
Figure 6.3. Rose diagram presentation for geo-electric strike directions for all stations.

The geoelectrical strike orientation in the study area was obtained as $N25°E$. The results of the studies by Higgins et al. (2015), gave the dominant azimuth direction in a range between 25° and 35°. The strike analyses show that the orientation of geological and geoelectrical strikes in the study area are similar. On the other hand, the complexity of the lithological resistivity may be the reason for the different values obtained. In the process of 3-D modeling of the subsurface resistivity information of MT data, it is important that the structural orientation of the study area and the geoelectrical orientation obtained are compatible to obtain a suitable, accurate and minimum error value model. The value we obtained, and the value measured during the field study are close to each other proving the reliability of our data. In addition to this, when one takes a glance at the map in Figure 6.4, it is possible to say that the structural orientation of the study area is shaped by the faults in the region and there is a rotation to the northeast.

The variations in the electric and magnetic fields with respect to time are recorded during field studies. The time-domain data are transformed into frequency-domain using the discrete Fourier transform (DFT). The impedance is then calculated from the frequency-domain data. As a result, the apparent resistivity and phase values are obtained, and these values are plotted as a function of frequency.

All apparent resistivity and phase curves are plotted for all of the sounding locations. The whole data set was observed bit-by-bit, and general information about the resistivity property of the study region was obtained (The apparent resistivity and phase curves for all stations are presented in the Appendix A).

The location of all stations in ESC is presented on the map below (Figure 6.4). Three stations were selected to better interpret the characteristics of the study area, and to recognize the different structures in the region. It is possible to see the locations of stations 20, 6 and 24, respectively, from Figure 6.4. The data obtained from the apparent resistivity, phase and phase tensor ellipses are read from these two-part graphs. Station number 20 is the dataset of one of the stations installed west of the ESC (Figure 6.5). When the apparent resistivity curves are examined, the transition is starting from resistive values getting more conductor as it goes deeper, and after about around 1 Hz its starts to becoming more resistive. The XY and YX modes in the phase plots give the resistivity variation of the field for the two perpendicular axes. The fact that the curves are apart is proof that the environment is either 2-D or 3-D. On the map, this point coincides with the restriction of two different auxiliary faults (Yeşilhisar Fault on the left and Erciyes Fault on the right). The opposite is true for data at station number 6 (Figure 6.6). This station is located outside the volcanic area, near the EPB boundary. In curves and ellipses, there is a fluctuation from conductor to resistive structure. The fact that the phase frequencies are separate from each other indicates that dimensionality is dominant in the medium. The resistivity values of the number 20 and number 6 stations are close to each other. They're probably pointing to the same resistive anomaly. The station number 24 is located in the region between Erciyes and Develi faults (Figure 6.7). It is possible to observe that two curves are separated from each other which is kind of represented these fault lines. The phase curves of this station have the same effect. There is a trend from the higher phase to the lower phase, from conductor to resistive. 2-D / 3-D dimensionality dominates the environment.
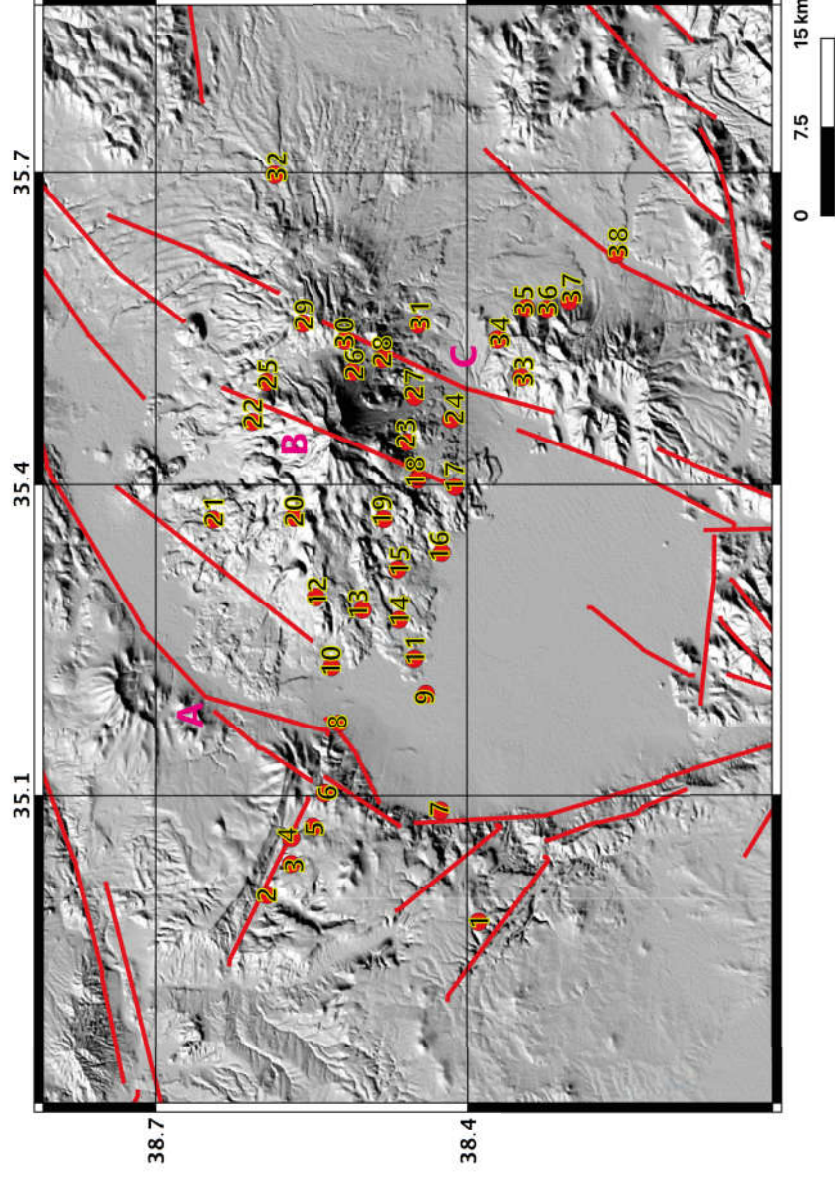
Figure 6.4. The map in the figure shows the locations of all sounding stations in ESC and the fault lines surrounding the region. Red lines indicate fault lines. The fault names for the letters A, B, and C are Yeşilhisar F., Erciyes F., and Develi F., respectively. (The information about the fault lines belongs to N. Kaymakçı as personal communication.)
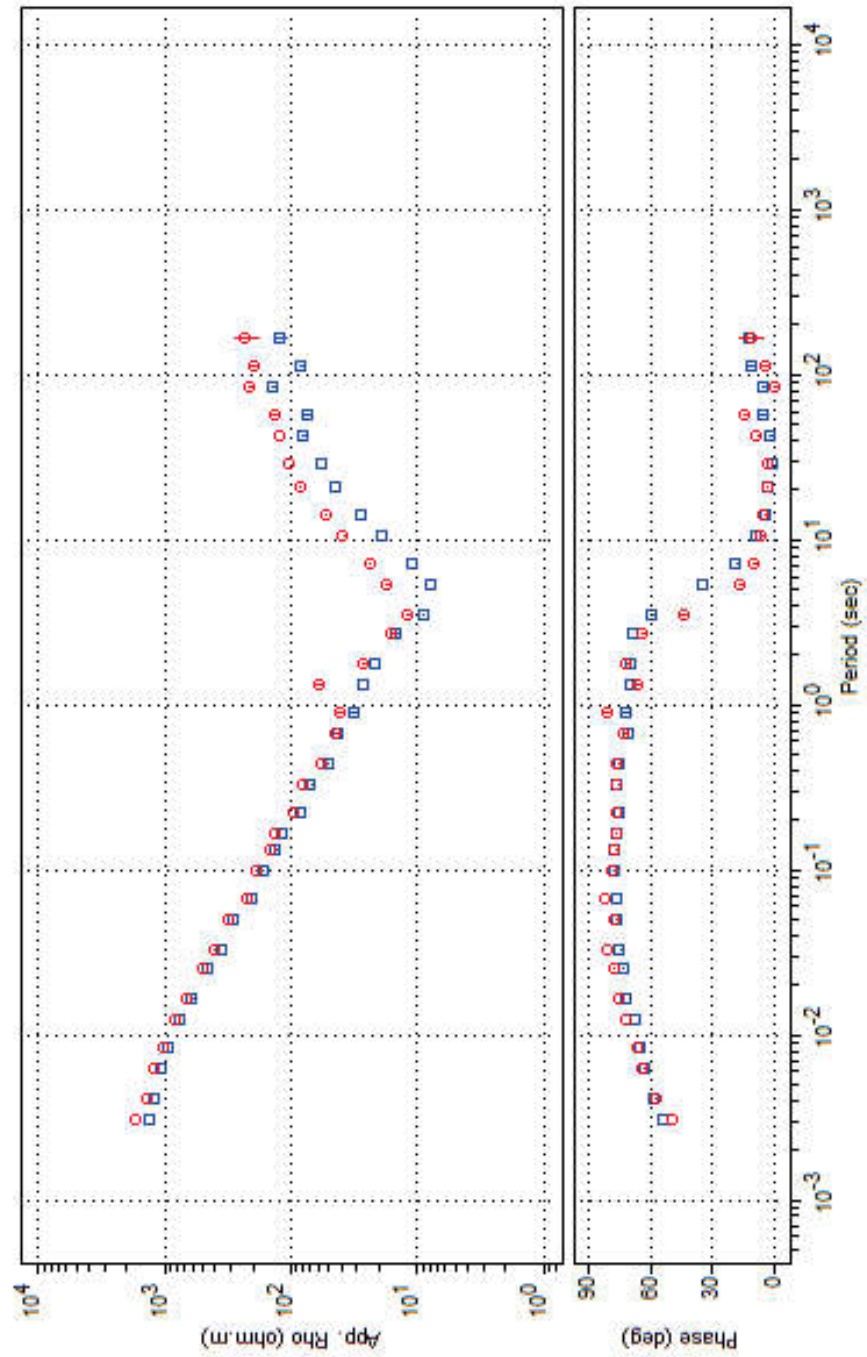
Figure 6.5. Apparent resistivity and phase curve of station number 20. See the map in Figure 6.4 for the station's location.
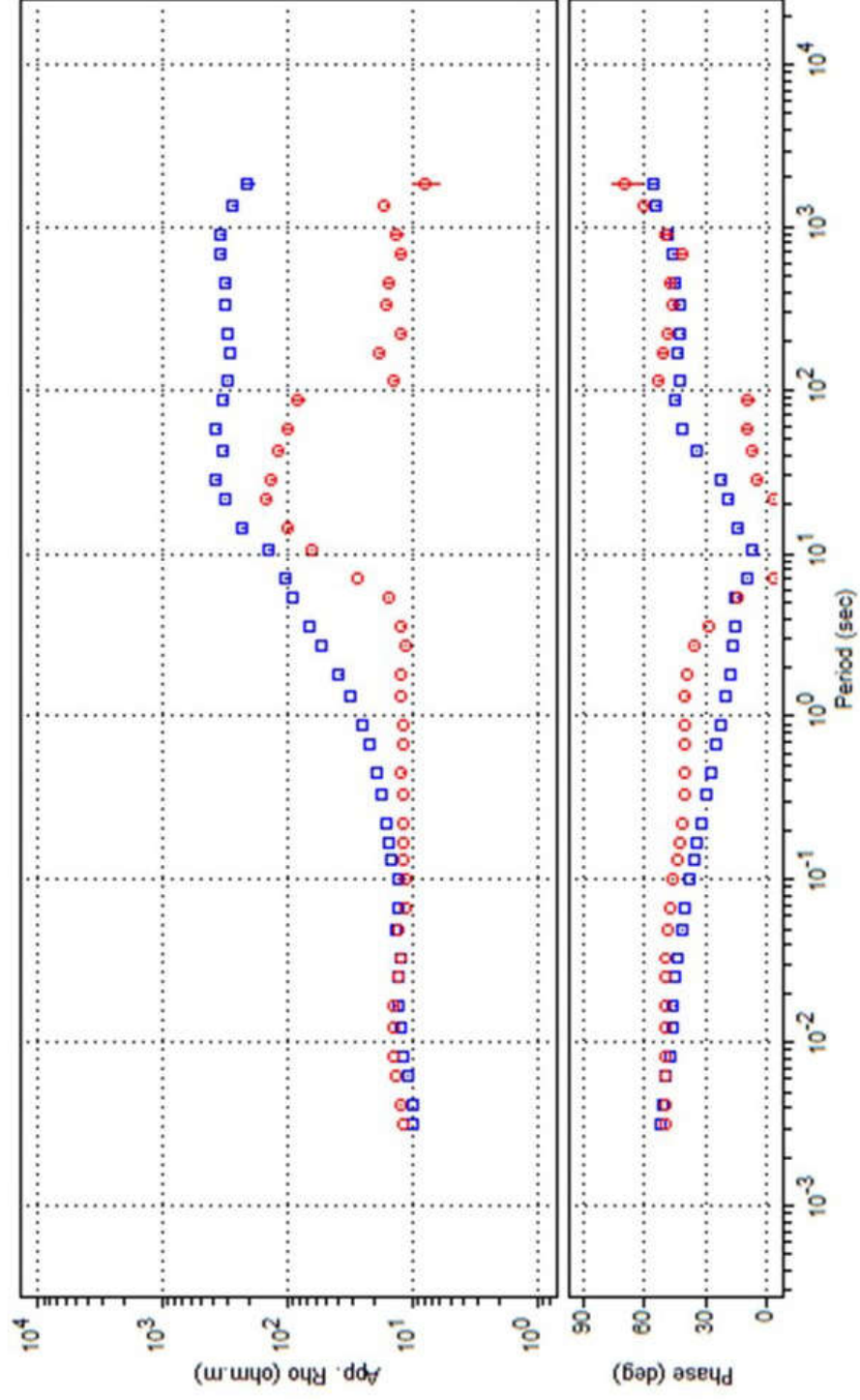
Figure 6.6. Apparent resistivity and phase curve of station number 6. See the map in Figure 6.4 for the station's location.

Figure 6.7. Apparent resistivity and phase curve of station number 24. See the map in Figure 6.4 for the station's location.

The data obtained as a result of the phase tensor analyses are mostly compatible with the stress orientation of the region. The local electrical characteristics of a region may vary over short distances depending on the geological diversity of the region, but the regional trend in fault lines and similar systems are generally in the same orientation. Based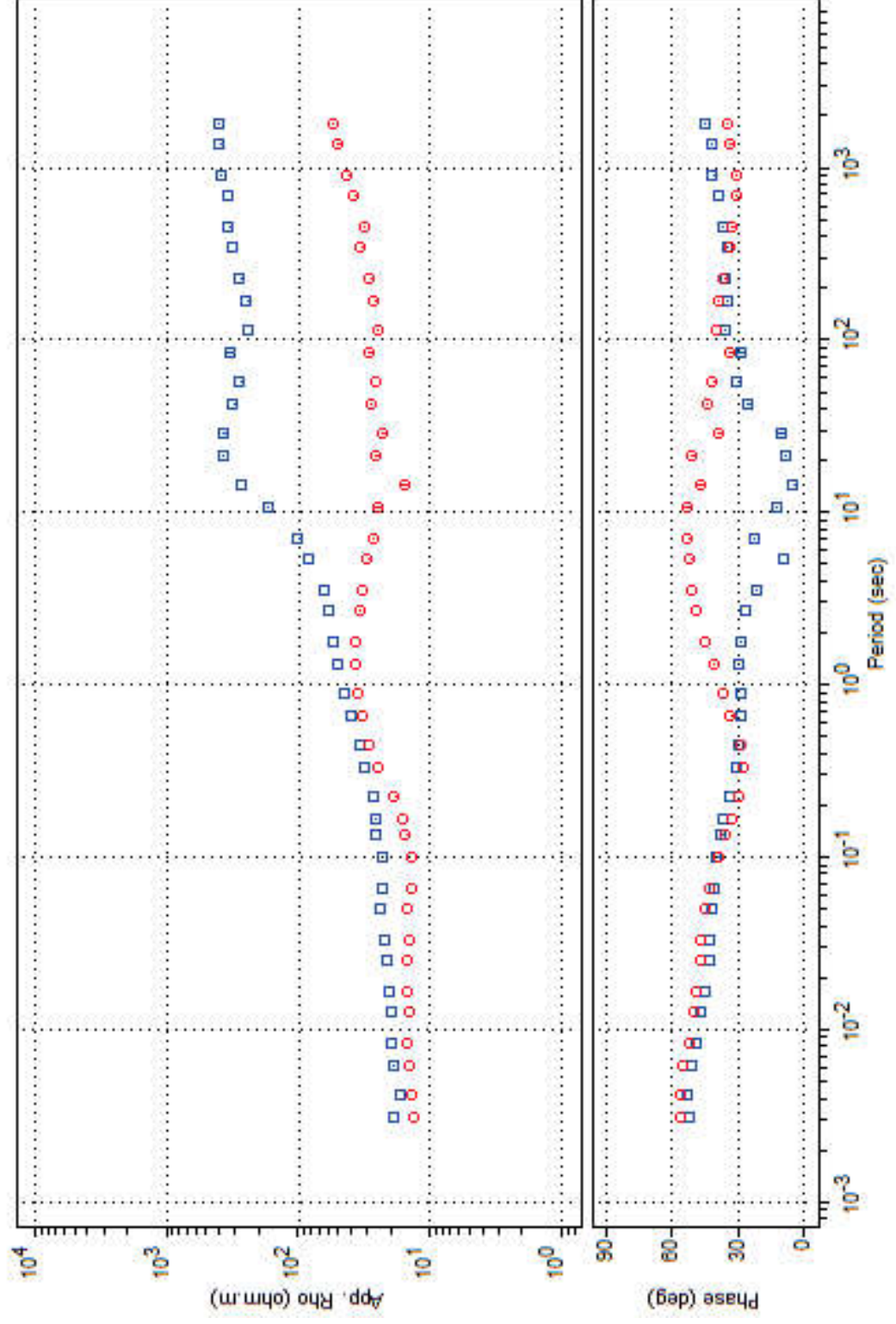 on this information, the measurement results of the phase tensor analyses can help to make comments on the directional and geoelectrical trends of the study area. The Φ_{max} values of various stations indicate the direction of geoelectric impact which increases in intensity as the difference between the maximum and minimum phases increases. According to Bibby et al. (2005), a deviation from a perfectly round shaped circle is considered a drift from the ideal 1-D medium.

On the shaded digital elevation model in Figure 6.8, the red circles indicate the locations of the stations, the lines indicate fault lines, and the yellow lines provide information about the profiles of sections named P1, P2 and P3. The wide-band-MT used in the modeling of Mt. Erciyes has three phase pseudo-sections of phase tensor ellipses, filled with skew values (Figures 6.9, 6.10, 6.11). Basic information about the polarization direction of the major axes and the dimensionality of the β value / skew angle is obtained from the ellipses in the phase tensor plots. The aim is to interpret the electrical-structural properties of the region. Colors between dark red and dark blue that fill the ellipses are associated with higher and lower β values, which express three-dimensionality. The first part is derived from measurements of stations surrounding the caldera of the Koç Dağ. It is possible to examine the obtained data in three different profiles. When the phase tensor ellipses of the first profile (NE - SW) are examined (Figure 6.9), low β values appear at higher frequencies, a very one-dimensional electrical structure becomes evident for frequencies around 1 Hz, and a one-dimensional orientation is observed. The orientation of ellipses below 1 Hz is similar to the EPB orientation. The second profile (Figure 6.10) is parallel to the first profile but on the west of Mt. Erciyes. This profile is located where the mountain vents are centered upon. At around 0.1 Hz, ellipses tend to be one-dimensional. The surface has a one-dimensional character, while three-dimensionality dominates deeper. Profile 3 (Figure 6.11) is NW - SE oriented and lies relatively on the south of the volcano. Dimensionality changes from three dimensions to two and one from west to east. This

exchange zone is found deeper in the west than in the east.
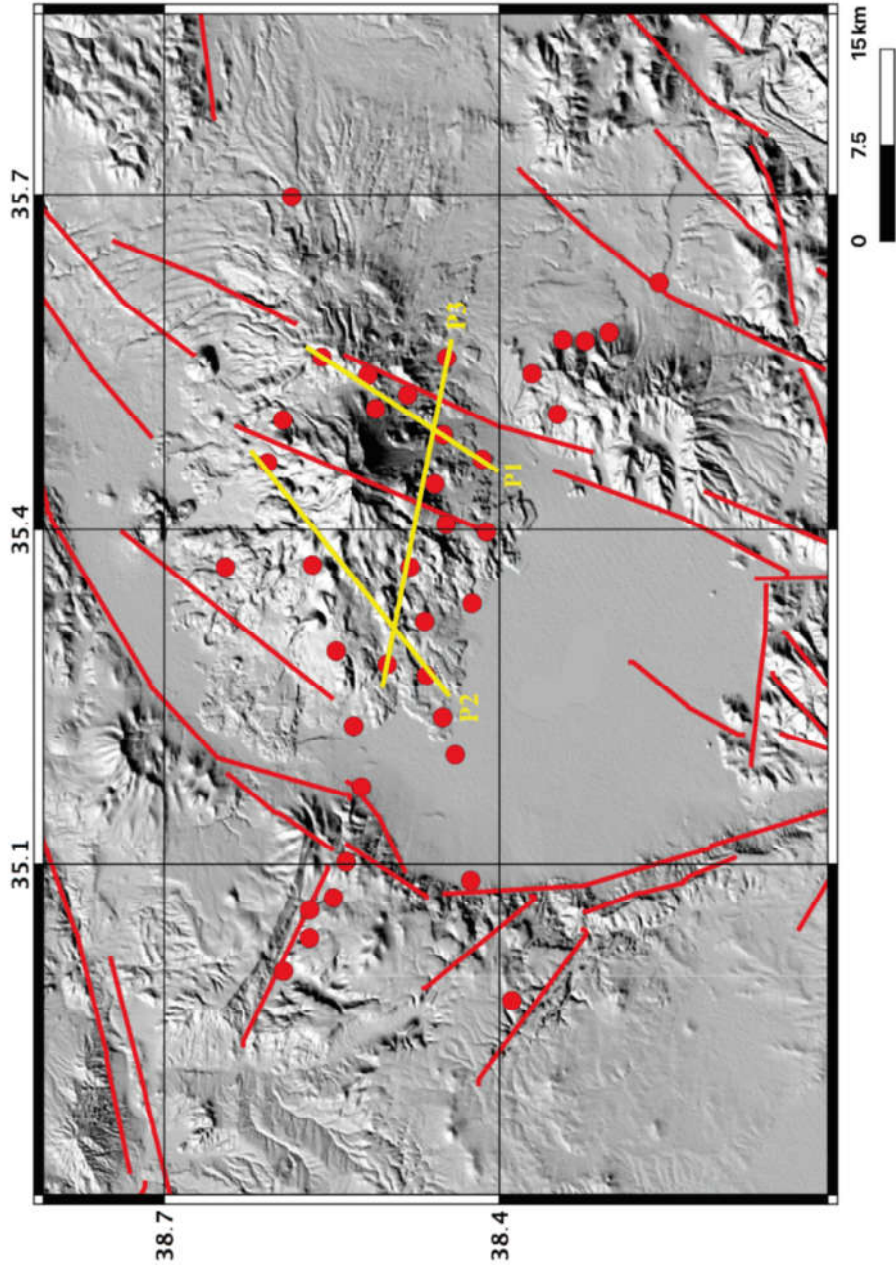
Figure 6.8. The map above contains the location information of the phase tensor profiles (yellow lines) painted with skew values.Red lines indicate fault lines. (The information about the fault lines belongs to N. Kaymakçı as personal communication.)
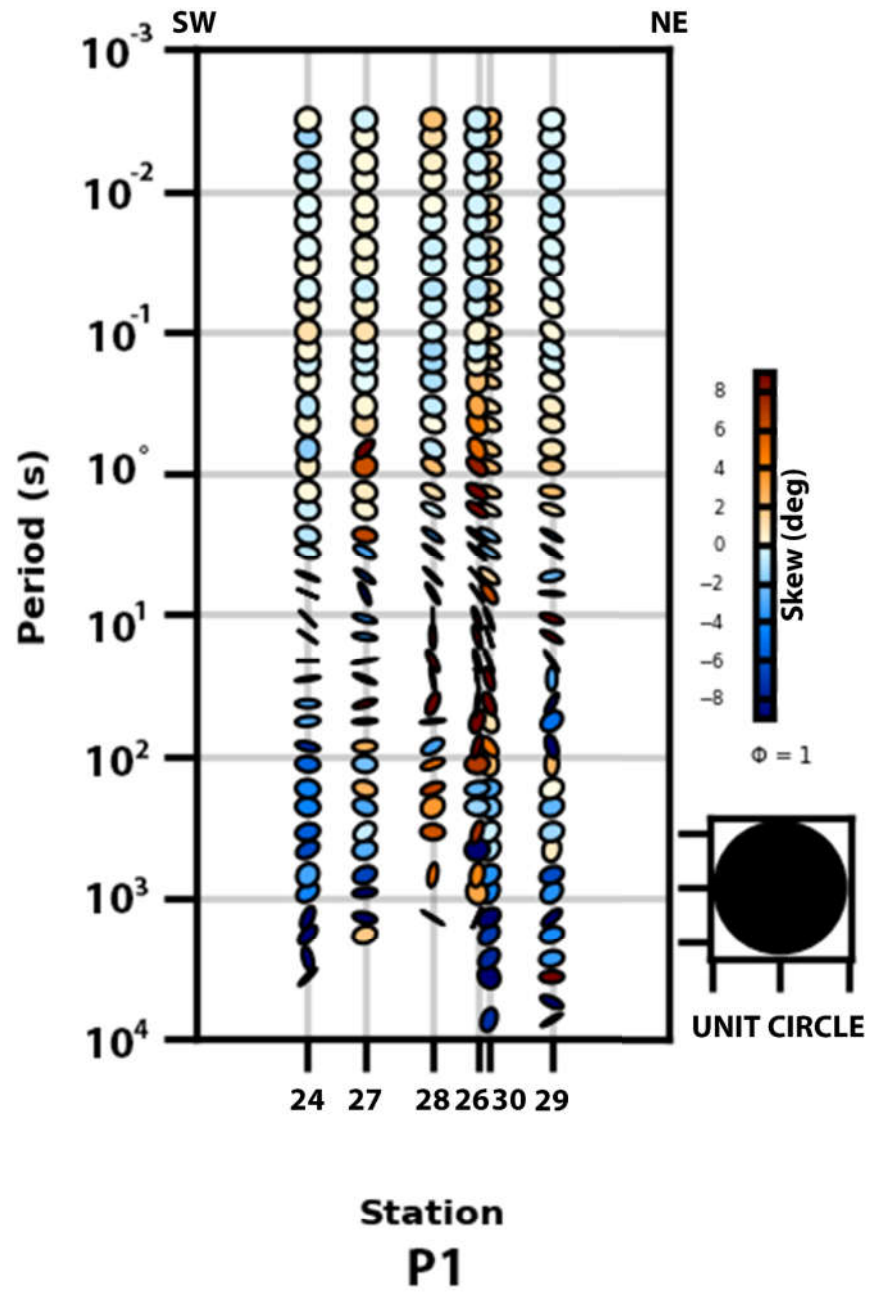
Figure 6.9. Profile 1 is a pseudo-section containing data from six sounding locations recorded around Mt. Erciyes. Ellipses are colored with the β value.
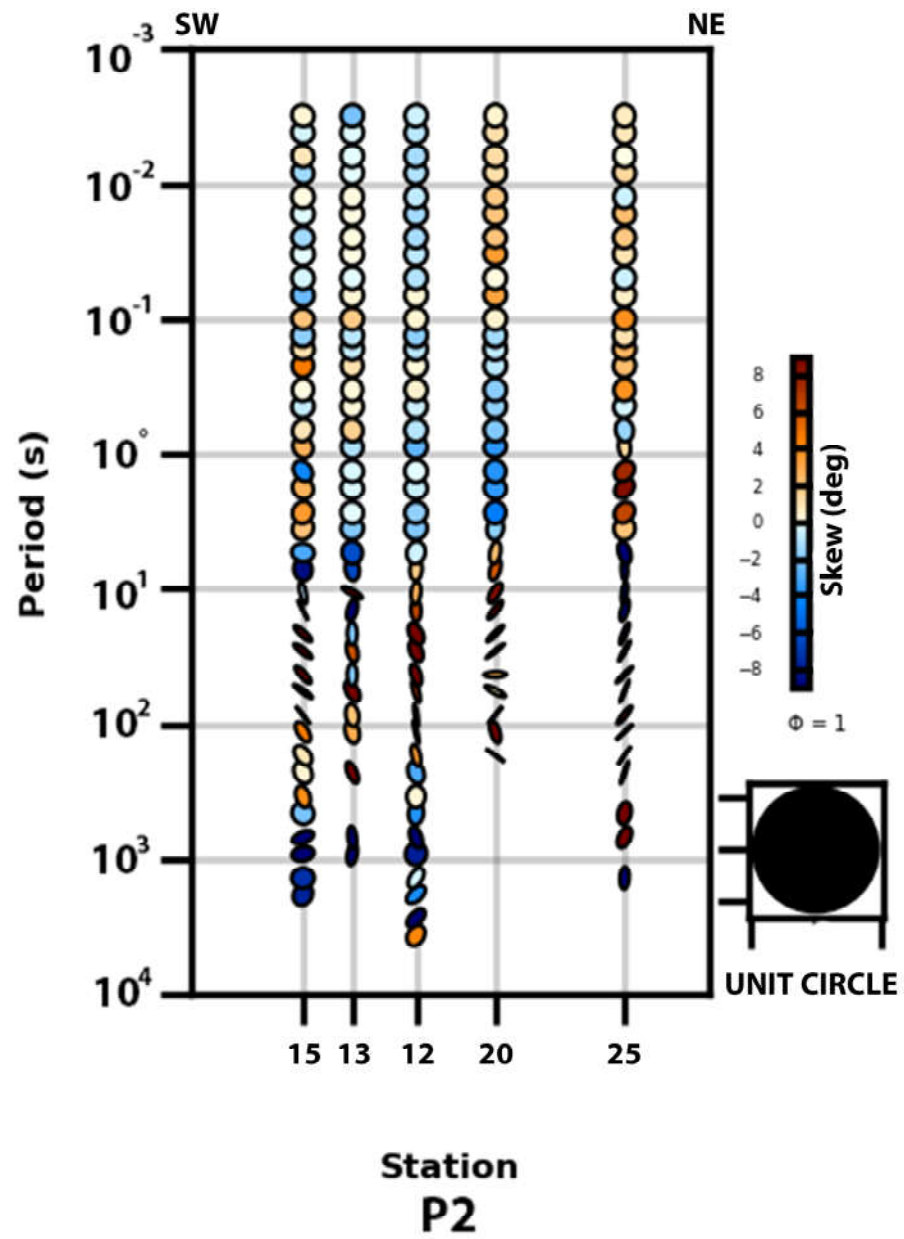
Figure 6.10. Profile 2 is a pseudo-section containing data from five sounding locations recorded around Mt. Erciyes. Ellipses are colored with the β value.
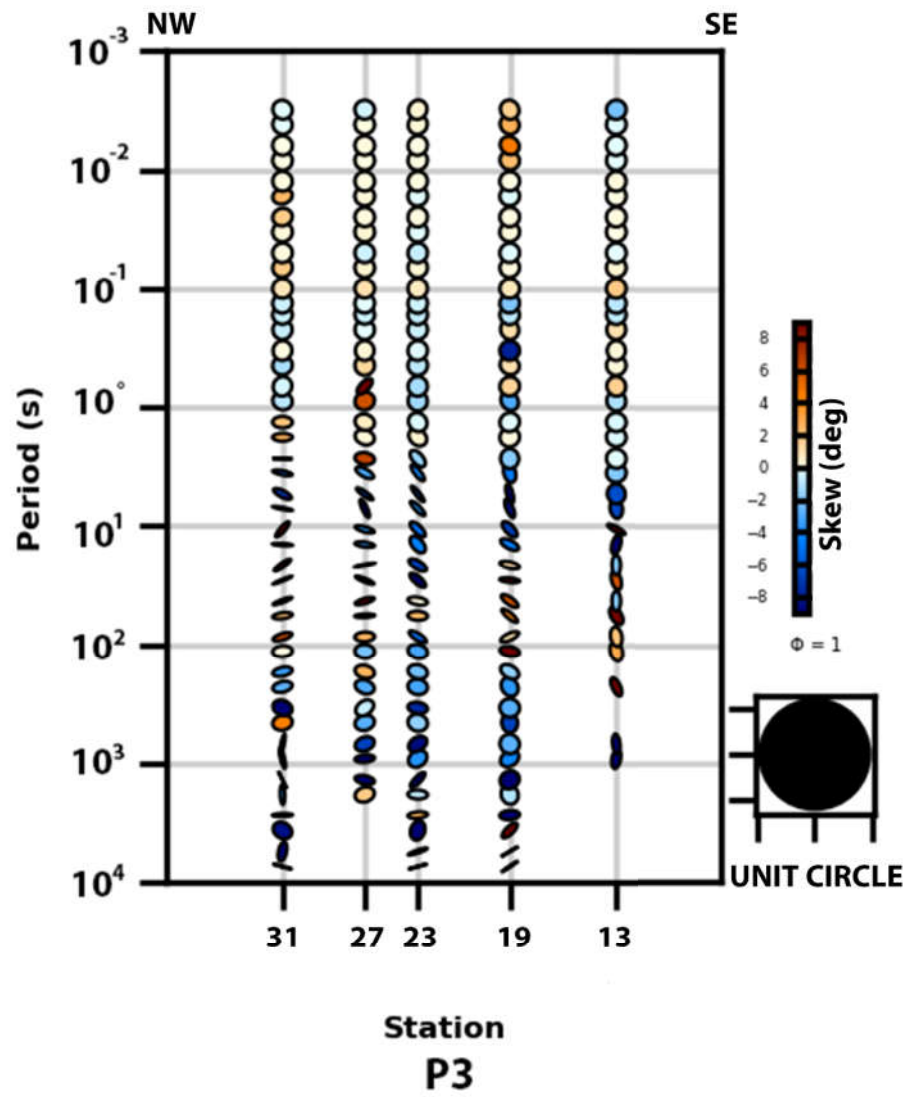
Figure 6.11. Profile 3 is a pseudo-section containing data from five sounding locations recorded around Mt. Erciyes. Ellipses are colored with the β value.
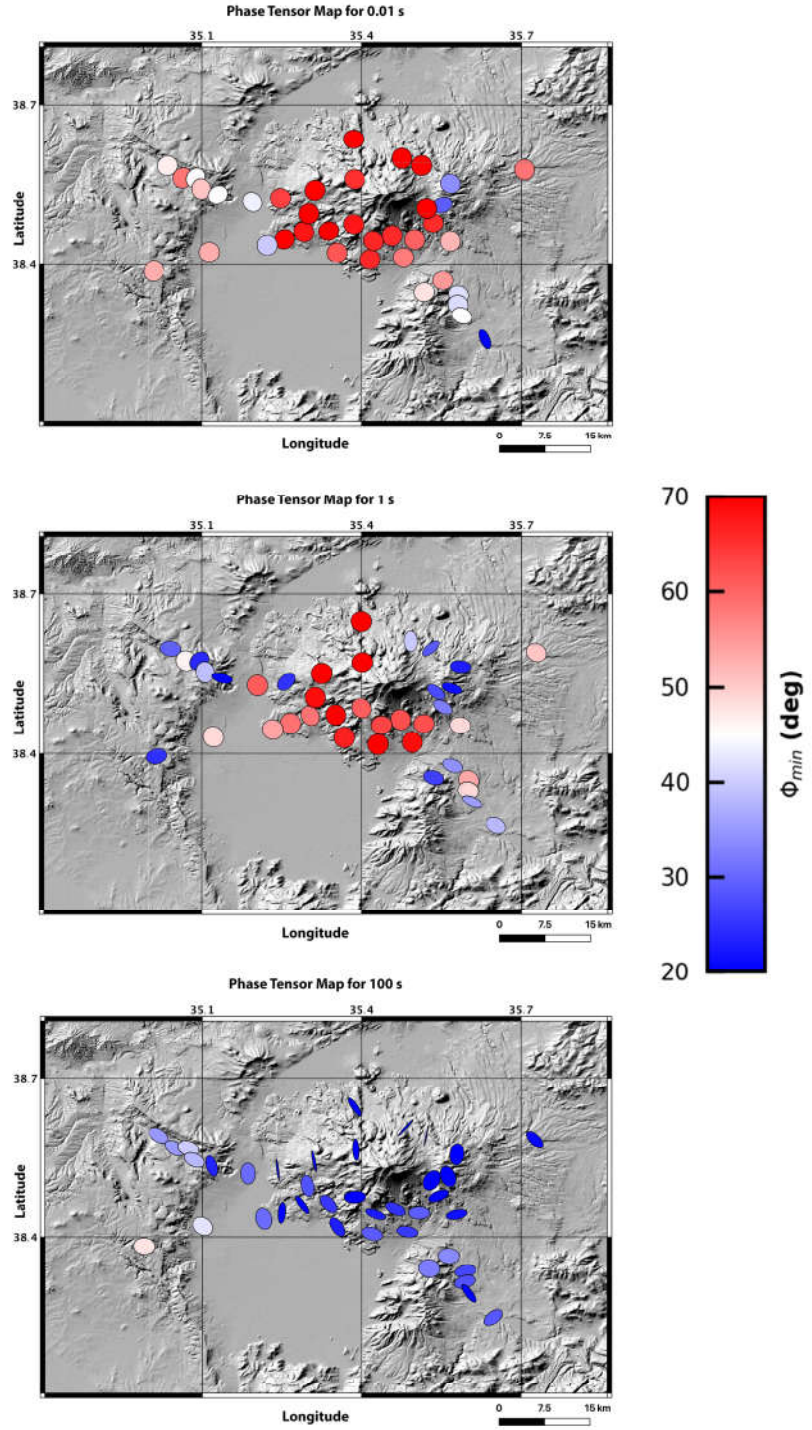
Figure 6.12. Phase tensor ellipses with topography for 0.01 s, 1 s and 100 s. The color scale of ellipses is enlightened about the change in the conductivity values through Φ_{min} in degrees. It means that high Φ_{min} values indicate a structure that is changing from high resistivity to high conductivity.

The above-mentioned Figure (6.12) shows the phase tensor ellipses with topography information for 0.01 s, 1 s, and 100 s. In the ellipses in the figure, the dimensionality of the MT data can be observed without distortion. Ellipses are filled with color to demonstrate the change in the conductivity by means of Φ_{min} in degrees. Especially the colored (red and blue) ellipses indicate the 3-D character. For interpretation, it should be considered that high Φ_{min} values indicate a structure that changes from high resistivity to high conductivity.

Figure (6.13) consists of six different conductivity slices to observe conductor changes at different depths (2 km, 3 km, 4 km, 5 km, 7 km, 10 km) and topography data are not included. The purple hexagrams represent the locations of the measurements taken from the volcanic complex. The dark blue region at a depth of 1000 m represents the air layers. The purpose of the plots is to conduct a preliminary investigation to learn about low and high resistivity anomalies. The surface layer of the model is taken as the reference height as zero. Looking at the plots, five slices show highly resistant anomalies under the volcanic complex that can be easily recognized. From the section that gives the information on 2000 m depth, the conductive and resistive regions under the complex have begun to emerge.
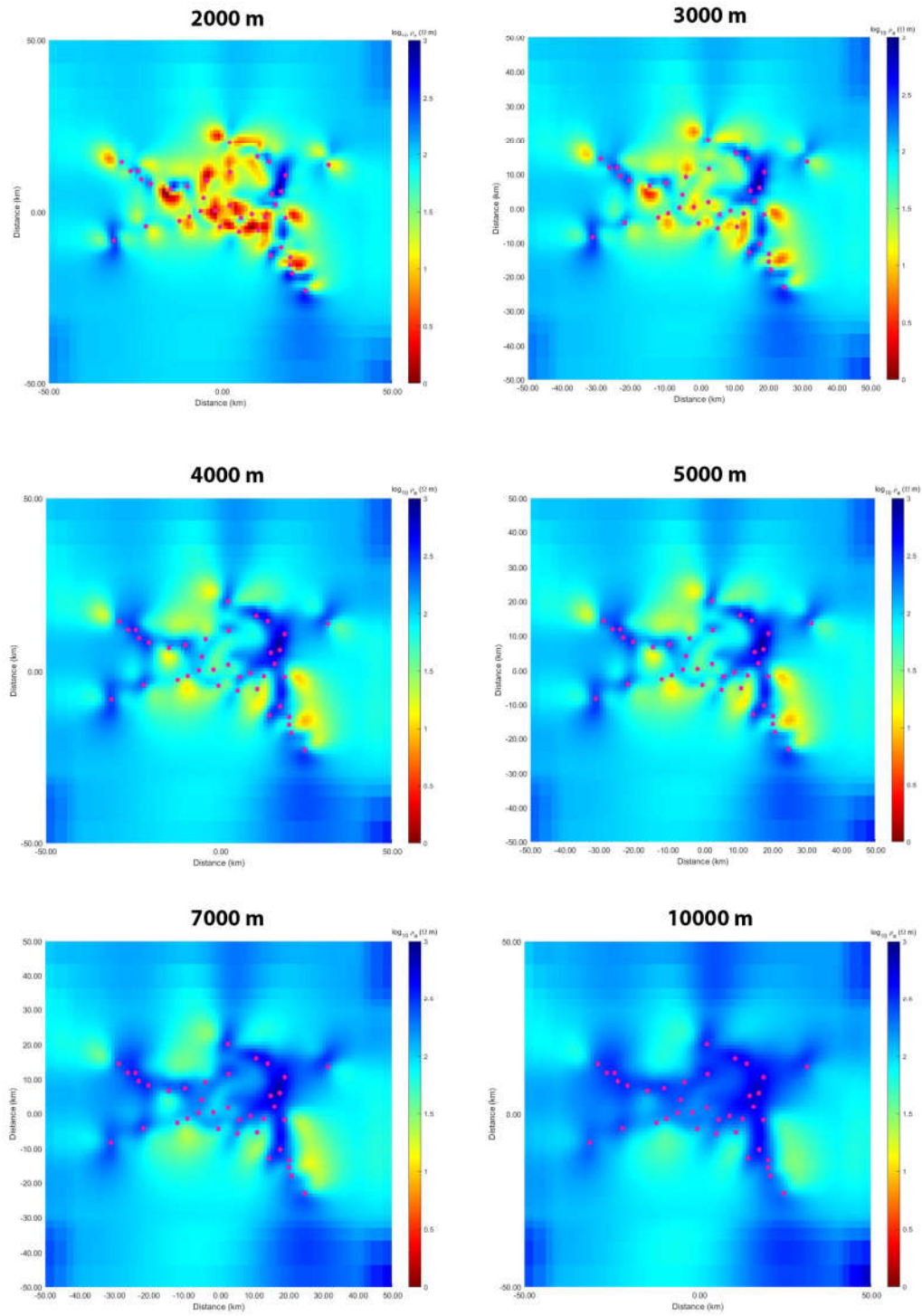
Figure 6.13. Resistivity slices were plotted for six different depths achieved from the resulting model in the map view form (without topography information).
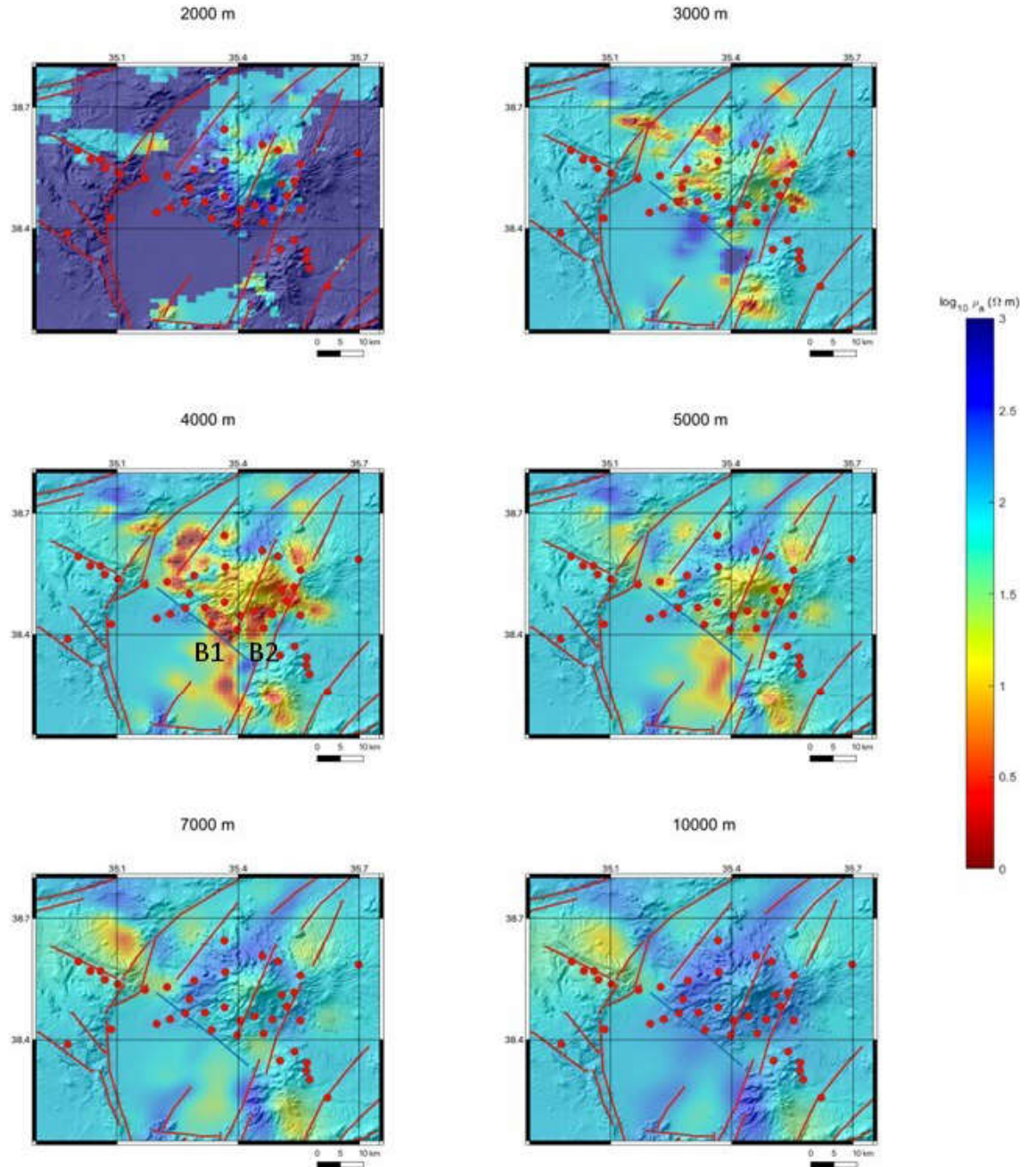
Figure 6.14. Six different resistivity slice maps were generated from the topographic final data. Location of the MT stations (represented by red circles), auxuliary fault information (represented by red lines) and topography map were added to the sections.

Figure 6.14 shows six consecutive resistivity depth slices of 2, 3, 4, 5, 7 and 10 km, respectively, in the study area. Topography data, station locations and auxiliary fault lines responsible for tectonism in the region are also added to the slices. The red circles represent the locations of the measurements taken from the volcanic complex. The dark blue region at a depth of 2000 m represents the air layers. As in the slices without topography (Figure 6.14), the surface layer of the model is taken as 0 as the reference height. When the bird's-eye view of the sections in the figure is examined, it is possible to see the entire electrical structure of Mt. Erciyes. Conductive-resistive boundaries overlap with fault lines in the region.
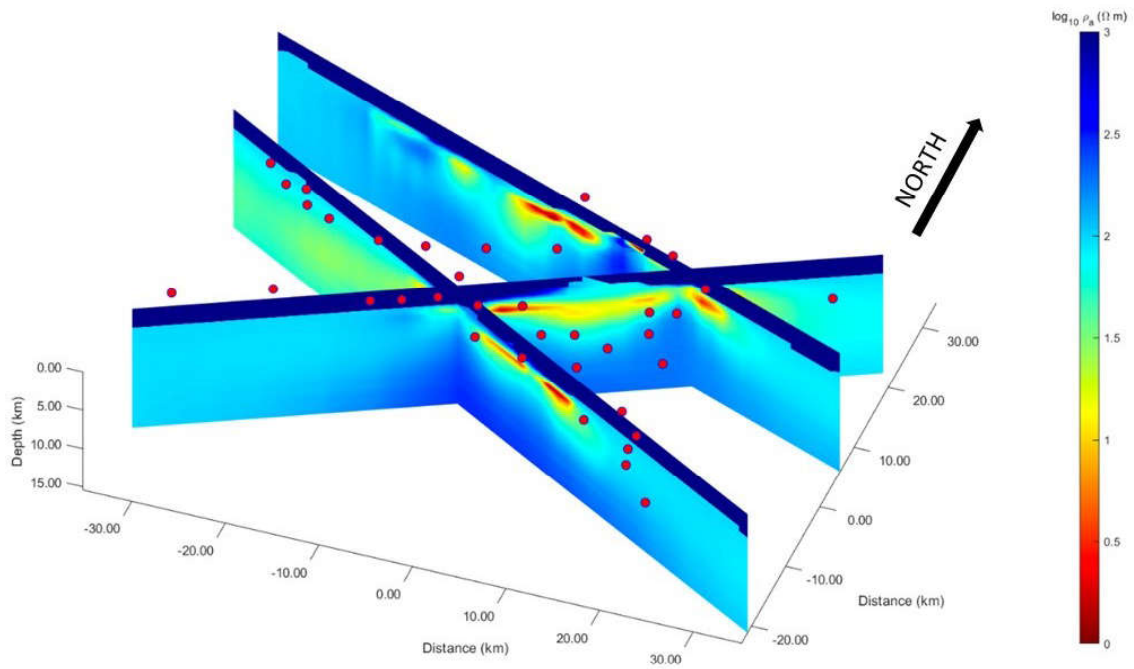
Figure 6.15. The resistivity cross-section. Red reverse circles point out the sounding locations on this profile.

The final regional inversion scheme converged into a model with an RMS value of 3.07 at the end of the 110th iteration. Figure 6.15 was drawn according to the fault system, and extending in the northeast-southwest direction. It is parallel to the

Yeşilhisar and Develi fault lines, which are the major fault lines in the region. This section provides the most realistic information on the dimensions and geometry of the conductors present in the study area because of the orthogonality. The low resistivity anomalies are apparent in this profile.

When the final resistivity model was observed (Figure 6.16), an essential and widespread conductive layer was observed under the volcanic complex C1, C3, C4 about 5 km depth. The relatively lower resistivity anomaly is apparent in this profile C2. There is a largely resistive layer under the low-resistivity C2 structure R1. All visible conductive fields are spread between two fault lines (Yeşilhisar and Develi Faults). The conductive-resistive boundaries of these conductive layers under the volcano are cut by the three dominant faults in the region (Yeşilhisar, Erciyes and Develi Faults).

Figure 6.16. The resistivity section is drawn parallel to the direction of geoelectrical strike (above). It is possible to see a zoomed-in version of the same section below.

7. DISCUSSION

7.1. Geological Evolution of Mt. Erciyes

The region where Mt. Erciyes is located has a complicated geological and tectonic structure. The complexity of the structure originates from the high tectonic activity experienced during the evolution of the region. There are many active faults and auxiliary fault segmen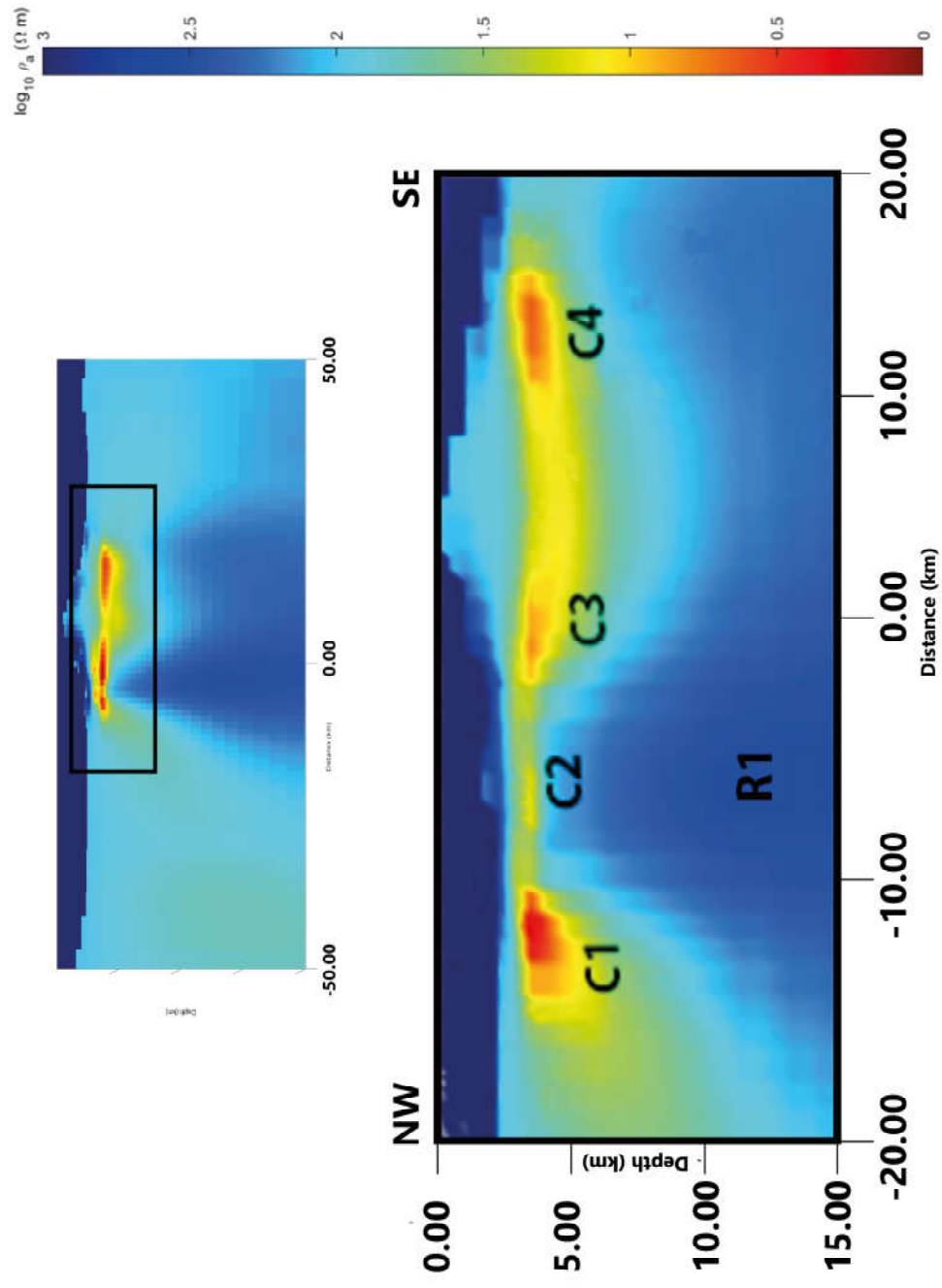ts surrounding the volcano. Mt. Erciyes stands at the boundary between the Anatolide-Tauride block and Central Anatolian Crystalline Complex (CACC) which also serves as a suture zone known as Inner Tauride Suture (ITS) zone. The first intense orogenic movement in the ATB started at the end of the Cretaceous and continued until the Miocene. As of the Miocene, the orogeny movement ended, and volcanism initiated. It is possible to examine the evolution of Mt. Erciyes in two distinct stages; namely the Koç Dağ and the Erciyes (Kürkcüoğlu et al., 1998; Şen et al., 2003). The Koç Dağ, the first part of the evolution, is characterized by the first explosive activity, the VTI (2.5 Ma. Çiner and Aydar, 2019), leading to the formation of a caldera (Innocenti et al., 1975). While magmatic activities during the formation of the Koç Dağ and the Erciyes cause the dominant calc-alkaline products to be observed in the region, alkaline and tholeiitic components are also present in the region. Koçyiğit et al. (2001) refers to the VTI is the most sensitive spot to understand the chronostratigraphic formation of the basin and Mt. Erciyes. Geochemical studies suggested that Mt. Erciyes volcanism occurred as a direct consequence of strike-slip faulting present in the region (Alıcı - Şen et al., 2004; Doğan et al., 2013).

Mt. Erciyes and its located area are surrounded by many auxiliary fault lines and segments. EFZ is one of the important auxiliary fault lines in this region. The reason why it is essential is that EFZ played a role in the evolution of Mt. Erciyes (Toprak, 1998; Şen et al., 2003). With the tectonic regime it developed, the EFZ allowed the stratovolcano complex to settle in this region (Tatar et al., 2000).

One can examine the evolution of the ESC in several stages (Şen et al., 2003):

i. A basaltic volcano was formed with andesitic flow forms.

ii. This previously formed volcano collapses, and the main andesitic stratovolcano develops in its place.

iii. Andesitic and dacitic evolution started.

iv. Olivine - basalt outflows started from this dacitic origin structure formed and it was deposited on the western slope.

v. The central crater lava flows are of hyalodacite origin.

Since Mt. Erciyes is a stratovolcano, each eruption it undergoes during its evolution accumulates and forms a layer on the surface. The eruption of lava in different compositions of the volcano shows that the origin magmas forming the lava are also of different compositions. Mt. Erciyes has evolved to produce a more acidic magma during this process.

7.2. Shallow Structure Analyses

Shallow structure analysis is characterized by ignimbrites. The chemical composition of ignimbrites consists of the origin magma that forms it. The VTI is an essential distinction between the Koç Dağ and the Erciyes phases and provides significant information about the content of magma. A substantial feature of VTI is that, unlike other ignimbrites, it does not contain any biotite (Le Pennec et al., 1994; Çiner et al., 2011). Considering the Bowen reaction series, the absence of biotite can be interpreted as the crystallization of magma at high temperatures.

The resistivity of the ignimbrites can be classified according to their state, welded or non-welded. According to Wohletz (2006), welded ignimbrites can have resistivity values ranging from 17 to 60 Ωm, while welded ignimbrites can have values ranging from 200 to 1400Ωm. According to Temel et al. (1998), the thickness of the welded ignimbrites is 5-15 m. Şen et al. (2003), gives an approximately similar result by classifying them as welded, medium welded and well welded for 3m, 4m and 7m, re-

spectively. Dinçer and Bostancı (2019), and Akin et al. (2021) argue that VTI has a strongly welded structure. In the model we obtained, the approximate resistivity value of ignimbrites is $80\Omega m$. In this case, it is possible to define it as welded.

The model we obtained is not sufficient to give detailed information about the thickness of the ignimbrites, but at Figure 6.15 (2000 m) it is possible to observe that the VTI has been deformed by the fault lines in the region. This situation can be interpreted that the faulting in the region that occurred before the VTI. Higgins et al. (2015) state that the ignimbrite layer is subjected to syndepositional deformation and faulting causes this. Mt. Erciyes is a Quaternary stratovolcano; it indicates that the ignimbrites found in the complex are much older than the volcano (Çiner and Aydar, 2019). Starting from the ignimbrites, the faulting before it and the stratovolcano formed after it gives a brief summary of the dynamics of the region.

7.3. Deep Structure Analyses

The apparent resistivity and phase curves obtained show the electrical resistivity transition in different parts. (The apparent resistivity and phase curves for all stations are presented in the Appendix A). High conductivity values in the apparent resistivity curves indicate surface conductive layers. When the apparent resistivity and phase curves observed in the frequency domain of the Z_{xy} and Z_{yx} elements of EM impedance tensor are examined, the curves being separated from each other draws attention. These modes give the resistivity variation of the field for the two perpendicular axes; based on this information, the separation observed especially in stations around the caldera is proof that the environment is 2 - D or 3 - D. The presence of many fault lines / auxiliary fault lines in ESC can be shown as the reason for this unconformity. Besides on the complex structure of the region, the results obtained from the phase tensor analysis of the MT data confirmed the strong inhomogeneity in the study area. In Figures 6.9, 6.10, 6.11 phase tensors are presented graphically with ellipses, following the illustration methods of Caldwell et al. (2004), which showed the polarization direction of the major axes and gave basic information about the dimensionality of the β values (i.e., skew angles). The ellipses are filled with colors ranging from red to dark

blue for highlighting high and low β values for expressing the asymmetry of the phase tensor as an indicator for three-dimensionality. When the phase tensor ellipses of the stations around the volcano are examined, low β values at higher frequencies stand out, and a three- dimensional electrical structure becomes evident for deeper parts. Stations 29 (See the map in Figure 6.4 for the station's location) and 30 (See the map in Figure 6.4 for the station's location) show a different orientation from surrounding stations.

Phase tensor ellipses suggest similar results in the region (Figure 6.12). From the ellipses in the figures, the dimensionality of the MT data can be observed without distortion. As can be seen in this figure, there are higher Φ_{min} values at 100 s and at 1 s compared to 0.01 s. The ellipses in Figure 6.12 indicates a shallow homogeneous layer that achieves higher conductivity values over a more complex deeper structure. Ellipses of 0.01 s indicate higher conductivity compared to surrounding locations. When examined at all four periods, it is seen that the ellipses point to the conductor.

In the latest model, which includes 38 stations, a piece of evidence was observed that indicated the presence of a relatively small conductivity anomaly and three widespread conductive areas in the surrounding system that lies beneath Mt. Erciyes. In both models (with topography and without topography), it is possible to observe several conductive - resistive interfaces. Active sinistral faulting resulted in the displacement of the Central Anatolian Fault zone (4-24 km since Miocene according to Aktuğ et al., 2013). In Figure 6.14, at 4000 m slice, there are two anomalies (B1 and B2) separated from each other. This conductors look likes shifted by the lateral movement of this fault zone. It can be a proof the left lateral movement of the fault and traceable on the models.

On the other hand, when all C anomalies are examined together, they can be interpreted as magma pockets belonging to a large magma chamber and separating from each other over time instead of a single large magma chamber. This situation is similar when considering the reservoir model theory proposed by Klügel et al. (2005).

It is an expected result that the fault lines define conductive - resistive interfaces. These interfaces coincide with the surficial fault traces on the models. Earlier Koçyiğit and Erol (2001) prepared a similar figure for describing the structure and the position of the faults in a geological sense. The models based on the resistivity structure achieved in the current study suggest similar positions for similar faults. From these available data, a similar block-faulted zone can be expected below the volcano.

All the numerical models obtained in this study show that the width of the conductive zone is greater below the central structure of the volcano. Since the cross-section (Figure 6.15) is orthogonal to the active fault system, it provides the most realistic information on the dimensions and geometry of the conductors present in the study area because of the orthogonality. The low resistivity anomalies are appearing in this profile. To the west of the volcanic complex there is a deeper conductive layer (C1 in Figure 6.16). It can be said that these structures in the east and west of the volcano feed each other and show the route through which hot gases and magma are transported to the cone of the volcano. Considering the conductive regions observed in the model; a deeper source is required to increase the melt fraction. Comparing Figure 6.13 and Figure 6.14 , it is possible to observe the boundaries of the conductors in all slices. The lower limit of the resistive zone can be determined as about 8 - 10 km.

The electrical conductivity of the subsurface is an essential parameter in the study of hydro/geothermal and volcanic environments and is gaining increasing popularity in MT research around the world (Muñoz, 2014). In the final resistivity model, the conductive and resistive regions are named C1, C2, C3, C4 and R1 (the conductive ones C1 and C2 and a highly resistive anomaly R1). Sensitivity tests confirm the location of this conductive anomaly. There aren't any vertically distributed high-conductivity anomalies to recharge the C1 - C4 anomalies. This observation indicates that the volcano is far from activity.

The C1 anomaly in the west of the volcano goes deeper and was moved by the fault. C1, the resistivity value ($< 10 \Omega m$) is consistent with the clay alteration (smectite and illite-smectite) formed due to a possible hydrothermal activity around Mt.

Erciyes (Muñoz, 2014). Most importantly, the largest conducting zone C1 is located near the faulting zone and postglacial valleys. The hydrothermal activities in İncesu and Yeşilhisar (Kayseri - Türkiye), suggested by Ak et al. (2015), are close to C1, making this anomaly related to hydrothermal. In this case, the source of the magma/heat in this region is essential. Volcanic activity on Mt. Erciyes continued until about 2000 years ago, and today only volcanic gas and hot water eruptions are observed (Dirik, 2009). It is possible to associate this situation with hydrothermal activity, but at the same time, this activity can cause unrest. Samrock et al. (2015) obtained models similar to Mt. Erciyes in their study to determine the unrest in the Aluto volcano. They explained the absence of an active source under the Aluto and the unrest of the volcano as it is located in the hydrothermal system. For the other conductive and resistive structures, there is no source or magma chamber to feed the anomalies. Friedrichs et al. (2020) argue that the long-term zircon crystallization of the last 300,000 years is the presence of an evolved magma reservoir located beneath the volcano. It is possible to overlap this structure with C3 and C4 anomalies. Fault line borders physically demarcate the resistive/conductive anomalies. After C1, the source melts moved both vertically and laterally (about 5-10 km) along C2, C3, and C4, respectively. The progression from C4 to C1 indicates a potential path towards shallow areas just below the ESC. In the resistive structures observed in the final model (Figure 6.16), a relatively conductive medium C2 stands out, which can be interpreted as a common region feeding each other between anomalies.

To comment on the ongoing tectonic processes, cross-sections (Figure 6.15) from the final electrical resistivity models can be examined. Section C is approximately 30 km long lying inside the EPB and is aligned in a NW - SE direction. Yeşilhisar and Develi fault lines define the boundaries of the anomaly. The EFZ emerges as an abrupt interface between conductive and resistive anomalies C3 and C4. This conductive interface hosts a structure of dacite - pyroclastics and falls just below the topographic peak of the model. Moving to the north along the EFZ, there is another highly conductive anomaly that can be identified as materials called VTI (Higgins et al., 2015). The current model shows high conductivity anomalies below Mt. Erciyes. In the EPB, the auxiliary faults of the EFZ, which strengthened the suitable environment

for the upward movement of the volcanic materials accumulated in the region, limited the interconnected highly conductive zones at shallow depths.

The sketch in Figure 7.1 summarizes the electrical characteristics of the study zone of this thesis, obtained from the results indicated above. When the shallow structure is examined, some resistive layers can be seen covering the volcanic body. Most probably they are related to the lava blocs. The blue structures correspond to the part VTI. There are some conductive anomalies in the deep structure. While the Yeşilhisar and Develi faults restrict the basin, it is possible to see all resistive anomalies that are illustrated between them. There is a widespread conductor overall beneath Erciyes. C1 might be related to some hydrothermal activity. On the other hand, C3 and C4 are possible hydrothermal reactive anomalies separated by a fault line. The absence of a deep source is the reason of magma chamber is not possible for this volcano.
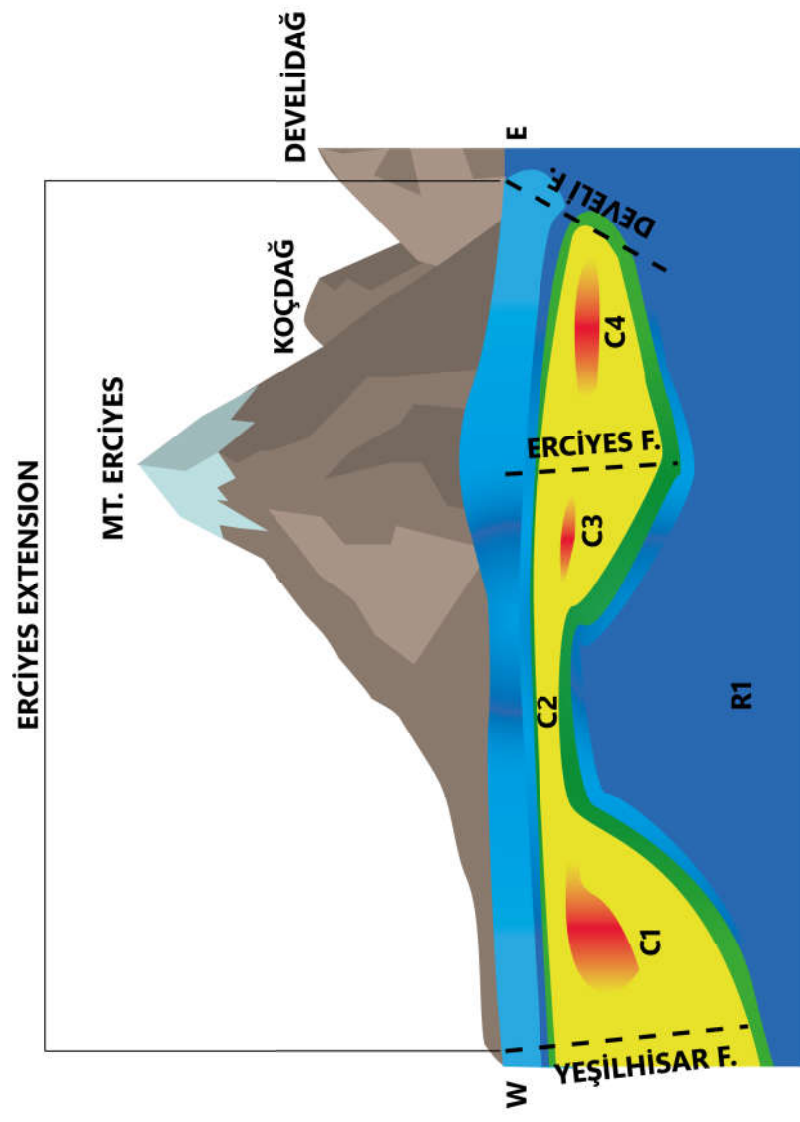
Figure 7.1. The figure presents a simplified outline of the result from the MT resistivity model.

8. CONCLUSION

MT data were collected at the ESC located in CA to display the electrical conductivity distribution of the region, were obtained from a total of 48 stations and only 38 of them were used in the modeling process. These data were used to create the first detailed 3-D electrical resistivity model of the ESC and surrounding area. Dimensionality analysis and 3-D inversions with wide-band MT datasets were evaluated to resolve the conductivity structure of the study area and yielded the results presented as a thesis.

Mt. Erciyes is located in a complex tectonic and geological environment. Despite the complexity, the phase tensor analyses of the acquired MT data and the resulting models provide clear images that highlight key elements of existing structures. At the end of the MT data evaluation process, the geoelectric impact value obtained from the impedance tensor was calculated as $\sim N25°E$. This strike angle is consistent with the geologic strike. The resulting model was with several major conductive features imaged at different depths and locations beneath Mt. Erciyes and ESC. When the obtained electrical resistivity models are observed, the resistive and conductive boundaries are visible. Based on this result, it can be stated that the MT method is an effective way to view the transitions of regions.

A relatively deeper and larger anomaly was observed to the west of the final pattern (about 5 km deep). This anomaly, called C1, could be a potential hydrothermal region. The location and shape of the C2 anomaly indicate a common region feeding each other between anomalies. Since a source thought to feed the anomalies is not reflected in the final model, it is not possible to talk about a possible magma chamber in the region. Since a source thought to feed the anomalies is not reflected in the final model, it is not possible to talk about a possible magma chamber in the region. However, these anomalies can be interpreted as residual magma pockets. For more detailed results and more detailed research to be obtained from the region, it is recommended to conduct a study with more stations.

REFERENCES

Aizawa, K., Y. Ogawa, and T. Ishido, 2009, "Groundwater Flow and Hydrothermal Systems within Volcanic Edifices: Delineation by Electric Self-Potential and Magnetotellurics", *Journal of Geophysical Research: Solid Earth*, Vol. 114, No. B1.

Aizawa, K., C. Cimarelli, M.A. Alatorre-Ibargüengoitia, A. Yokoo, D.B. Dingwell, and M. Iguchi, 2016, "Physical Properties of Volcanic Lightning: Constraints from Magnetotelluric and Video Observations at Sakurajima Volcano, Japan", *Earth and Planetary Science Letters*, Vol. 444, pp. 45-55.

Ak, S., O. Yumuk, H. Yıldız, and M. Mengeloğlu, 2015, "Hamurcu-(İncesu-Kayseri ve Başdere (Yeşilhisar-Kayseri) Au-Ag-Cu-Mo-Pb-Zn-As Cevherleşmesi", *MTA Doğal Kaynaklar ve Ekonomi Bülteni*, Vol. 20, pp. 85-95.

Akin, L., E. Aydar, A. K. Schmitt, H. E. Çubukçu, and A. Gerdes, 2021, "Zircon Geochronology and O-Hf Isotopes of Cappadocian Ignimbrites: New Insights into Continental Crustal Architecture Underneath the Central Anatolian Volcanic Province, Turkey", *Gondwana Research*, Vol. 91, pp. 166-187.

Aktuğ, B., E. Parmaksız, M. Kurt, O. Lenk, A. Kılıçoğlu, M. A. Gürdal, and S. Özdemir, 2013, "Deformation of Central Anatolia: GPS Implications", *Journal of Geodynamics*, Vol. 67, pp. 78-96.

Asaue, H., T. Kubo, T. Yoshinaga, and K. Koike, 2012, "Application of Magnetotelluric (MT) Resistivity to Imaging of Regional Three-dimensional Geologic Structures and Groundwater Systems", *Natural Resources Research*, Vol. 21, No. 3, pp. 383-393.

Avşar, Ü., E. Türkoğlu, M. Unsworth, İ. Çağlar, and B. Kaypak, 2013, "Geophysical Images of the North Anatolian Fault Zone in the Erzincan Basin, Eastern Turkey, and Their Tectonic Implications", *Pure and Applied Geophysics*, Vol. 170, No. 3, pp. 409-431.

Aydar, E., E. Şen, M.A. Sarıkaya, and C. Kuzucuoğlu, 2019, "In the Footsteps of Strabon: Moun Erciyes Volcano—The Roof of Central Anatolia and Sultansazliği Basin", Springer, Cham, pp. 565-576.

Bahr, K., 1988, "Interpretation of the Magnetotelluric Impedance Tensor: Regional Induction and Local Telluric Distortion", *Journal of Geophysics*, Vol. 62, No. 1, pp. 119-127.

Bahr, K., 1991, "Geological Noise in Magnetotelluric Data: a Classification of Distortion Types", *Physics of the Earth and Planetary Interiors*, Vol. 66, No. 1-2, pp. 24-38.

Başokur, A. T., A. Koçyiğit, Ö. Hacıoğlu, H. İ. Arslan, N. Meqbel, 2022, "Magnetotelluric Imaging of the Shallow-seated Magma Reservoir Beneath the Karadağ Stratovolcano, Central Anatolia, Turkey", *Journal of Volcanology and Geothermal Research*, Vol. 427, pp. 107567.

Bayrak, M., and S. S. Nalbant, 2001, "Conductive Crust Imaged in Western Turkey by MT", *Geophysical Research Letters*, Vol. 28, No. 18, pp. 3521-3524.

Beamish, D., and J.M. Travassos, 1992, "A Study of Static Shift Removal from Magnetotelluric Data", *Journal of Applied Geophysics*, Vol. 29, No. 2, pp. 157-178.

Bertrand, E. A., T. G. Caldwell, G. J. Hill, E. L. Wallin, S. L. Bennie, N., Cozens,... and P. Wameyo., 2012, "Application of Fuzzy Set Theory", *IEEE Transactions on Systems, Man, and Cybernatics*, Vol. 39, No. 2.

Beynon, W. J. G., 1969, "The Physics of the Ionosphere", *Science Progress*, Vol. 1933, pp. 415-433.

Bibby, H. M., T. G. Caldwell, and C. Brown, 2005, "Determinable and Non-determinable Parameters of Galvanic Distortion in Magnetotellurics", *Geophysical Journal International*, Vol. 164, No. 3, pp. 915-930. Bozkurt, E., 2001, "Neotectonics of Turkey–a Synthesis", *Geodinamica acta*, Vol. 14, No. 1-3, pp. 3-30.

Cagniard, L., 1953, "Basic Theory of the Magneto-telluric Method of Geophysical Prospecting", *Geophysics*, Vol. 18 No. 3, pp. 4605635.

Caldwell, T. G., H. M. Bibby, C. and Brown, 2004, "The Magnetotelluric Phase Tensor", *Geophysical Journal International*, Vol. 158, No. 2, pp. 457-469.

Chen, C. C., C. S. Chen, and C. F. Shieh, 2002, "Crustal Electrical Conductors, Crustal Fluids and 1999 Chi-Chi, Taiwan, Earthquake", *Terrestrial Atmospheric and Oceanic Sciences*, Vol. 13, No. 3, pp. 367-374.

Chouliaras, G., and T. M. Rasmussen, 1988, "The Application of the Magnetotelluric Impedance Tensor to Earthquake Prediction Research in Greece", *Tectonophysics*, Vol. 152, No. 1-2, pp. 119-135.

Coe, A. L., *Geological Field Techniques*, John Wiley & Sons, New Jersey, 2010.

Cole, J. W., 1990, "Structural Control and Origin of Volcanism in the Taupo Volcanic Zone, New Zealand", *Bulletin of Volcanology*, Vol. 52, No. 6, pp. 445-459.

Constable, S. C., A. S. Orange, G. M. Hoversten, and H. F. Morrison, 1998, "Marine Magnetotellurics for Petroleum Exploration Part I: A Sea-Floor Equipment System", *Geophysics*, Vol. 63, No. 3, pp. 816-825.

Constable, S., and L. J. Srnka, 2007, "An Introduction to Marine Controlled-source Electromagnetic Methods for Hydrocarbon Exploration", *Geophysics,*, Vol. 72, No. 2, pp. WA3-WA12.

Constable, S., 2010, "Ten Years of Marine CSEM for Hydrocarbon Exploration", *Geophysics*, Vol. 75, No. 5, pp. A67-A81.

Çiner, A. and E. Aydar, 2019, "In Landscapes and Landforms of Turkey: A Fascinating Gift from Volcanoes: the Fairy Chimneys and Underground Cities of Cappadocia", Springer, Cham, pp. 535-549.

Çiner, A., E. Aydar, K. Dirik, B. Rojay, O. Ersoy, E. Sayın, and A. Kutluay, 2011, *Vertical Anatolian Movement Project*, Y. M. A. TÜBİTAK Project No: 107Y333.

Dinçer, İ. and M. Bostancı, 2019, "Capillary Water Absorption Characteristics of Some Cappadocian Ignimbrites and the Role of Capillarity on Their Deterioration", *Environmental earth sciences*, Vol. 78, No. 1, pp. 1-18.

Dirik, K., 2001, "Neotectonic Evolution of the Northwestward Arched Segment of the Central Anatolian Fault Zone, Central Anatolia, Turkey", *Geodinamica Acta*, Vol. 14, No. 1-3, pp. 147-158.

Dirik, K., 2009, "Kapadokya Bölgesi'nin Jeolojisi, Jeomorfolojisi ve Bunların Bölgedeki Medeniyetler Üzerindeki Etkisi.", paper presented at the *1. Tıbbi Jeoloji Çalıştayı*, Ürgüp.

Dirik, K. and M. C. Göncüoglu, 1996, "Neotectonic Characteristics of Central Anatolia", *International Geology Review*, Vol. 38, No. 9, pp. 807-817.

Dogan, A. U., D. W. Peate, M. Dogan, F. I. Yesilyurt-Yenice, and O. Unsal, 2013, "Petrogenesis of Mafic–Silicic Lavas at Mt. Erciyes, Central Anatolia, Turkey", *Journal of Volcanology and Geothermal Research*, Vol. 256, pp. 16-28.

Egbert, G. D., and A. Kelbert, 2012, "Computational Recipes for Electromagnetic Inverse Problems", *Geophysical Journal International*, Vol. 189, No. 1, pp. 251-267.

Erinç, S., *Jeomorfoloji I (Güncelleştirenler: Ertek A., Güneysu C.)*, Der Yayınları, İstanbul, 2012.

Faccenna, C., O. Bellier, J. Martinod, C. Piromallo, and V. Regard, 2006, "Slab Detachment Beneath Eastern Anatolia: A Possible Cause for the Formation of the North Anatolian Fault", *Earth and Planetary Science Letters*, Vol. 242, No. 1-2, pp. 85-97.

Farquharson, C. G. and J. A. Craven, 2009, "Three-dimensional Inversion of Magnetotelluric Data for Mineral Exploration: An Example from the McArthur River Uranium Deposit, Saskatchewan, Canada", *Journal of Applied Geophysics*, Vol. 68, No. 4, pp. 450-458.

Friedrichs, B., J. C. Schindlbeck-Belo, M. Danišík, S. F. Jenkins, E. Yurteri, M. Cobankaya, ... and R. S. J. Sparks, 2020, "New Insights Into Source and Dispersal of Mediterranean S1 Tephra, an Early Holocene Marker Horizon Erupted at Mt. Erciyes (Turkey)", *Quaternary Science Reviews*, Vol. 249, pp. 106606.

Friedrichs, B., G. Atıcı, M. Danišík, E. Yurteri, A. K. Schmitt, 2021, "Sequence Modeling in Zircon Double-Dating of Early Holocene Mt. Erciyes Domes (Central Anatolia)", *Quaternary Geochronology*, Vol. 61, pp. 101129.

Fuentes-Arreazola, M. A., D. Núñez, F. J. Núñez-Cornú, A. Calderón-Moctezuma, D. Ruiz-Aguilar, and J. M. Romo-Jones, 2021, "Magnetotelluric Imaging of the Ceboruco Volcano, Nayarit, Mexico", *Journal of Volcanology and Geothermal Research*, Vol. 418, pp. 107339.

Groom, R.W. and R. C. Bailey, 1989, "Decomposition of Magnetotelluric Impedance Tensor in the Presence of Local Three-dimensional Galvanic Distortion", *J. Geophys. Res.*, Vol. 94, pp. 1913-1925.

Göncüoğlu, M. C., *"Introduction to the Geology of Turkey: Geodynamic Evolution of the Pre-Alpine and Alpine Terranes"*, General Directorate of Mineral Research and Exploration, 2010.

Güner, Y., and Ö. Emre, 1983, "Pleistocene Glaciation on Mount Erciyes and Its Relation to Volcanism", *Bulletin of Geomorphology 11*, pp. 23-34.

Gürer, A., M. Bayrak, and Ö. F. Gürer, 2004, "Magnetotelluric Images of the Crust and Mantle in the Southwestern Taurides, Turkey", *Tectonophysics*, Vol. 391, No. 1-4, pp. 109-120.

Haak, V., and R. Hutton, 1986, "Electrical Resistivity in Continental Lower Crust", *Geological Society, London, Special Publications*, Vol. 24, No. 1, pp. 35-49.

Heaney, M. B., 2003, "Electrical Conductivity and Resistivity", *Electrical Measurement, Signal Processing, and Displays*, Vol. 7, No. 1.

Heise, W., T. G. Caldwell, H. M. Bibby, and S. C. Bannister, 2008, "Three-dimensional Modelling of Magnetotelluric Data from the Rotokawa Geothermal Field, Taupo Volcanic Zone, New Zealand", *Geophysical Journal International*, Vol. 173, No. 2, pp. 740-750.

Higgins, M., L. M. Schoenbohm, G. Brocard, N. Kaymakci, J. C. Gosse, and M. A. Cosca, 2015, "New Kinematic and Geochronologic Evidence for the Quaternary Evolution of the Central Anatolian Fault Zone (CAFZ)", *Tectonics*, Vol. 34, No. 10, pp. 2118-2141.

Ingham, M. R., H. M. Bibby, W. Heise, K. A. Jones, P. Cairns, S. Dravitzki, and Y. Ogawa, 2009, "A Magnetotelluric Study of Mount Ruapehu Volcano, New Zealand", *Geophysical Journal International*, Vol. 179, No. 2, pp. 887-904.

Innocenti, F., R. Mazzuoli, G. Pasquare, F. R. Di Brozolo, and L. Villari, 1975, "The Neogene Calcalkaline Volcanism of Central Anatolia: Geochronological Data on Kayseri-Nigde Area", *Geological Magazine*, Vol. 112, No. 4, pp. 349-360.

Kaufman A. A. and G.V. Keller, *The Magnetotelluric Sounding Method, Methods in Geochemistry and Geophysics*, Elsevier Scientific Publishing Company, Vol.15, 1981.

Karaş, M., S. B. Tank, and S. Özaydın, 2017, "Electrical Conductivity of a Locked Fault: Investigation of the Ganos Segment of the North Anatolian Fault Using Three-Dimensional Magnetotellurics", *Earth, Planets and Space*, Vol. 69, No. 1, pp. 1-14.

Karaş, M., S. B. Tank, Y. Ogawa, N. Oshiman, M. Matsushima, and Y. Honkura, 2020, "Probing the Relationship Between Electrical Conductivity and Creep Through Upper Crustal Fluids Along the Western Part of the North Anatolian Fault with Three-dimensional Magnetotellurics", *Tectonophysics*, Vol. 791, pp. 228561.

Kaya, T., S. B. Tank, M. K. Tunçer, I. I. Rokoityansky, E. Tolak, and T. Savchenko, 2009, "Asperity Along the North Anatolian Fault Imaged by Magnetotellurics at Düzce, Turkey", *Earth, Planets and Space*, Vol. 61, No. 7, pp. 871-884.

Kaya, T., T. Kasaya, S. B. Tank, Y. Ogawa, M. K. Tunçer, N. Oshiman, ... and M. Matsushima, 2013, "Electrical Characterization of the North Anatolian Fault Zone Underneath the Marmara Sea, Turkey by Ocean Bottom Magnetotellurics", *Geophysical Journal International*, Vol. 193, No. 2, pp. 664-677.

Kaymakci, N., Y. Ozcelik, H. S. White, and P. M. Van Dijk, 2001, "Neogene Tectonic Development of the Çankiri Basin, Central Anatolia, Turkiye.", *Turkish Association of Petroleum Geologists Bulletin*, Vol. 13, No. 1, pp. 27-56.

Kelbert, A., N. Meqbel, G. D. Egbert, and K. Tandon, 2014, "ModEM: A Modular System for Inversion of Electromagnetic Geophysical Data", *Computers & Geosciences,*, Vol. 66, pp. 40-53.

Khyzhnyak, M., 2014, *Geoelectric Strike and Its Application in Magnetotellurics*, Ph.D. Thesis.

Klügel, A., T. H. Hansteen, and K. Galipp,, 2005, "Magma Storage and Underplating Beneath Cumbre Vieja Volcano, la Palma (Canary Islands)", *Earth and Planetary Science Letters*, Vol. 236, No. 1-2, pp. 211-226.

Koçyiğit, A. and A. Beyhan, 1998, "A new Intracontinental Transcurrent Structure: the Central Anatolian Fault Zone, Turkey", *Tectonophysics*, Vol. 284, No. 3-4, pp. 317-336.

Koçyiğit, A. and E. Oğuz, 2001, "A Tectonic Escape Structure: Erciyes Pull-Apart Basin, Kayseri, Central Anatolia, Turkey", *Geodinamica Acta*, Vol. 14, No. 1-3, pp. 133-145.

Kürkçüoğlu, B., E. Sen, E. Aydar, A. Gourgaud, and N. Gündoğdu, 1998, "Geochemical Approach to Magmatic Evolution of Mt. Erciyes Stratovolcano Central Anatolia, Turkey", *Journal of Volcanology and Geothermal Research*, Vol. 85, No. 1-4, pp. 473-494.

Kürkçüoğlu, B, E. Sen, A. Temel, E. Aydar, and A. Gourgaud, 2001, "Trace-element Modeling and Source Constraints for Tholeiitic and Calc-alkaline Basalts from a Depleted Asthenospheric Mantle Source, Mt. Erciyes Stratovolcano, Turkey", *International Geology Review*, Vol. 43, No. 6, pp. 508-522.

Kürkçüoğlu, B., E. Sen, A. Temel, E. Aydar, and A. Gourgaud, 2004, "Interaction of Asthenospheric and Lithospheric Mantle: the Genesis of Calc-alkaline Volcanism at Erciyes Volcano, Central Anatolia, Turkey", *International Geology Review*, Vol. 46, No. 3, pp. 243-258.

Lahee, F. H., *Field Geology*, McGraw-Hill Book Company, Incorporated, 1923.

Lee, B., M. Unsworth, K. Árnason, and D. Cordell, 2020, "Imaging the Magmatic System Beneath the Krafla Geothermal Field, Iceland: a New 3-D Electrical Resistivity Model from Inversion of Magnetotelluric Data", *Geophysical Journal International*, Vol. 220, No. 1, pp. 541-567.

Le Pennec, J. L., J. L. Bourdier, J. L. Froger, A. Temel, G. Camus, and A. Gourgaud, 1994, "Neogene Ignimbrites of the Nevsehir Plateau (Central Turkey): Stratigraphy, Distribution and Source Constraints.", *IEEE Transactions on Systems, Man, and Cybernatics*, Vol. 63, No. 1-2, pp. 59-87.

Ledo, J., P. Queralt, A. Martí, A. G. and Jones, 2002, "Two-dimensional Interpretation of Three- dimensional Magnetotelluric Data: an Example of Limitations and Resolution", *Geophysical Journal International*, Vol. 150, No. 1, pp. 127-139.

Madden, T. and P. Nelson, 1964, "A Defense of Cagniard's Magnetotelluric Method", *Magnetotelluric methods*, pp. 89-102.

Martí, A., P. Queralt, and J. Ledo, 2009, "WALDIM: A Code for the Dimensionality Analysis of Magnetotelluric Data Using the Rotational Invariants of the Magnetotelluric Tensor", *Computers & Geosciences*, Vol. 35, No. 12, pp. 2295-2303.

Maulinadya, S., and H. Grandis, 2019, "Geoelectric Strike Analysis from Magnetotelluric (MT) Data Using Swift and Polar Diagram Methods", *In IOP Conference Series: Earth and Environmental Science*, Vol. 318, No. 1, pp. 012049.

Mauriello, P., D. Patella, Z. Petrillo, and A. Siniscalchi, 2000, "An Integrated Magnetotelluric Study of the Mt. Etna Volcanic Structure".

McNeice, G. W., and A. G. Jones, 2001, "Multisite, Multifrequency Tensor Decomposition of Magnetotelluric Data", *Geophysics*, Vol. 66, No. 1, pp. 158-173.

McNeill, J. D., *Use of Electromagnetic Methods for Groundwater Studies*, In Geotechnical an Environmental Geophysics: Volume I: Review and Tutorial, pp. 191-218 ,Society of Exploration Geophysicists, 1990.

Meijers, M. J., N. Kaymakci, D. J. Van Hinsbergen, C. G. Langereis, R. A. Stephenson and J. C. Hippolyte, 2010, "Late Cretaceous to Paleocene Oroclinal Bending in the Central Pontides (Turkey)", *Tectonics*, Vol. 29, No. 4.

Menke, W., *Geophysical Data Analysis: Discrete Inverse Theory*, Academic press., 1984.

Monroe, J. S., R. Wicander, and R. W. Hazlett, *Physical Geology: Exploring the Earth*, Vol. 584, Belmont: Thomson Brooks/Cole, 2007.

Munoz, G., 2014, "Exploring for Geothermal Resources with Electromagnetic Methods", *Surveys in geophysics*, Vol. 35, No. 1, pp. 101-122.

Niasari, S. W., 2016, "A Short Introduction to Geological Strike and Geo-electrical Strike", *In AIP Conference Proceedings*, AIP Publishing LLC, Vol. 1755, No. 1, pp. 100002.

Ogawa, Y., M. Ichiki, W. Kanda, M. Mishina, and K. Asamori, 2014, "Three-dimensional Magnetotelluric Imaging of Crustal Fluids and Seismicity Around Naruko Volcano, NE Japan", *Earth, Planets and Space*, Vol. 66, No. 1, pp. 1-13.

Okay, A. I. and O. Tüysüz, 1999, "Tethyan Sutures of Northern Turkey", *Geological Society, London, Special Publications*, Vol. 156, No. 1, pp. 475-515.

Okay, Aral I., 2008, "Geology of Turkey: a Synopsis", *Anschnitt*, Vol. 21, pp. 19-42.

Özaydın, S., S. B. Tank, and M. Karaş, 2018, "Electrical Resistivity Structure at the North-Central Turkey Inferred from Three-dimensional Magnetotellurics", *Earth, Planets and Space*, Vol. 70, No. 1, pp. 1-9.

Panchuk, K., 2019, "Physical Geology; First University of Saskatchewan Edition".

Pasquare, G., 1968, "'Geology of the Cenozoic Volcanic Area of Central Anatolia (Provinces of Kayseri and Nevsehir, Turkey)", *Atti Accademia Nazionale dei Lincei*, Vol. 9, No. 1, pp. 53-204.

Piña-Varas, P., J. Ledo, P. Queralt, A. Marcuello, and N. Perez, 2018, "On the Detectability of Teide Volcano Magma Chambers (Tenerife, Canary Islands) with Magnetotelluric Data", *Earth, Planets and Space*, Vol. 70, No. 1, pp. 1-11.

Rawer, K., *Wave Propagation in the Ionosphere*, Springer Science & Business Media, Vol. 5, 2013.

Rikitake, T., 1948, "1. Notes on the Electromagnetic Induction within the Earth.", *Earth.Bull. Earthquake Res. Inst.*, Vol. 24, pp. 1-9.

Samrock, F., A. Kuvshinov, J. Bakker, A. Jackson, S. Fisseha, 2015, "3-D Analysis and Interpretation of Magnetotelluric Data from the Aluto-Langano Geothermal Field, Ethiopia", *Geophysical Journal International*, Vol. 202(3), pp. 1923-1948.

Sarıkaya, M. A., Z. Marek, and A. Çiner, 2009, "Glaciations and Paleoclimate of Mount Erciyes, Central Turkey, Since the Last Glacial Maximum, Inferred from 36Cl Cosmogenic Dating and Glacier Modeling", *Quaternary Science Reviews*, Vol. 28, No. 23-24, pp. 2326-2341.

Sasaki, Y., 2004, "Three-dimensional Inversion of Static-Shifted Magnetotelluric Data", *Earth Planets Space*, Vol. 56, pp. 239-248.

Serway, R. A., and J. W. Jewett, *Principles of Physics: A Calculus-Based Text*, Vol. 2, Cengage learning, 2012.

Simpson, F., K. Bahr, *Practical Magnetotellurics*, Cambridge University Press, 2005.

Siripunvaraporn, W., 2012, "Three-Dimensional Magnetotelluric Inversion: an Introductory Guide for Developers and Users", *Surveys in geophysics*, Vol. 33, No. 1, pp. 5-27.

Spitzer, K., 2001, "Magnetotelluric Static Shift and Direct Current Sensitivity", *Geophysical Journal International*, Vol. 144, No. 2, pp. 289-299.

Stanley, W. D., V. F. Labson, W. J. Nokleberg, B. Jr. Csejtey, and M. A. Fisher, 1990, "The Denali Fault System and Alaska Range of Alaska: Evidence for Underplated Mesozoic Flysch from Magnetotelluric Surveys", *Geological Society of America Bulletin*, Vol. 102, No. 2, pp. 160-173.

Swift, C. M. Jr., 1967, *A Magnetotelluric Investigation of an Electrical Conductivity Anomaly in the South-western United States*, Ph.D. Thesis, M.I.T..

Şen, E., B. Kürkçüoğlu, E. Aydar, A. Gourgaud, P.M. Vincent, 2003, "Volcanological Evolution of Mount Erciyes Stratovolcano and Origin of the Valibaba Tepe Ignimbrite (Central Anatolia, Turkey)", *Journal of Volcanology and Geothermal Research*, Vol. 125, No. 3-4, pp. 225-246.

Şen, P. A., A. Temel and A. Gourgaud, 2004, "Petrogenetic Modelling of Quaternary Post-Collisional Volcanism: a Case Study of Central and Eastern Anatolia", *Geological Magazine*, Vol. 141, No. 1, pp. 81-98.

Şengör, A. C., and Y. Yilmaz, 1981, "Tethyan Evolution of Turkey: a Plate Tectonic Approach", *Tectonophysics*, Vol. 75, No. 3-4, pp. 181-241.

Şengör, A. M. C., O. Tüysüz, C. Imren, M. Sakınç, H. Eyidoğan, N. Görür, and C. Rangin, 2005, "The North Anatolian Fault: A New Look", *Annu. Rev. Earth Planet. Sci.*, Vol. 33, pp. 37-112.

Tank, S. B., Y. Honkura, Y. Ogawa, M. Matsushima, N. Oshiman, M. K. Tunçer, ... and A. M. Işıkara, 2005, "Magnetotelluric Imaging of the Fault Rupture Area of the 1999 Izmit (Turkey) Earthquake", *Physics of the Earth and Planetary Interiors*, Vol. 150, No. 1-3, pp. 213-225.

Tank, S. B., and M. Karaş, 2020, "Unraveling the Electrical Conductivity Structure to Decipher the Hydrothermal System Beneath the Mt. Hasan Composite Volcano and Its Vicinity, SW Cappadocia, Turkey, *Journal of Volcanology and Geothermal Research*, Vol. 405, pp. 407048.

Tatar, O.,J. D. Piper, and H. Gürsoy, 2000, "Palaeomagnetic Study of the Erciyes Sector of the Ecemiş Fault Zone: Neotectonic Deformation in the Southeastern Part of the Anatolian Block", *Geological Society, London, Special Publications*, Vol. 173, No. 1, pp. 423-440.

Temel, A., M. N. Gündoğdu, A. Gourgaud, and J. L. Le Pennec, 1998, "Ignimbrites of Cappadocia (Central Anatolia, Turkey): Petrology and Geochemistry", *Journal of Volcanology and Geothermal Research*, Vol. 85, No. 1-4, pp. 447-471.

Tikhonov, A. N., 1985, "On Determining Electrical Characteristics of the Deep Layers of the Earth's Crust", *Doklady*, Vol. 73, No. 2, 1950.

Toprak, V., 1998, "Vent Distribution and Its Relation to Regional Tectonics, Cappadocian Volcanics, Turkey", *Journal of Volcanology and Geothermal Research*, Vol. 85, No. 1-4, pp. 55-67.

Tseng, K. H., Y. Ogawa, S. B. Tank, N. Ujihara, Y. Honkura, A. Terada, A., ... and W. Kanda, 2020, "Anatomy of Active Volcanic Edifice at the Kusatsu–Shirane Volcano, Japan, by Magnetotellurics: Hydrothermal Implications for Volcanic Unrests", *Earth, Planets and Space*, Vol. 72, No. 1, pp. 1-11.

Unsworth, M., W. Wenbo, A. G. Jones, S. Li, P. Bedrosian, J. Booker, and T. Handong, 2004, "Crustal and Upper Mantle Structure of Northern Tibet Imaged with Magnetotelluric Data", *Journal of Geophysical Research: Solid Earth*, Vol. 109, No. B2.

Unsworth, M., 2005, "New Developments in Conventional Hydrocarbon Exploration with Electromagnetic Methods", *CSEG Recorder*, Vol. 30, No. 4, pp. 34-38.

Vozoff, K., 1972, "The Magnetotelluric Method in the Exploration of Sedimentary Basins", *Geophysics*, Vol. 37, No. 1, pp. 98-141.

Vozoff, K., 1991, "The Magnetotelluric Method", in Nabighian, M. N., Ed.,Electromagnetic methods in applied Geophysics: Volume 2, Application, Parts A and B, Vol. 2, *SEG*, pp. 641-711.

Ward, S. E., and G. W. Hohmann, 1987, "Electromagnetic Theory for Geophysical Applications", *Electromagnetic Methods in Applied Geophysics*, Vol. 1, pp. 130-311.

Weinstein, L. A., *Electromagnetic waves*, Radio I Svyaz', Moscow, 1988.

Wohletz, K., 2006, "Fractures in Welded Tuff.", *Special Papers-Geological Society Of America*, Vol. 408 pp.17-31.

Yang, D., W. Guo, and Y. Tan, 2018, "Application of Magnetotelluric Method to the Detection of Overburden Failure Height in Shallow Seam Mining", *Arabian Journal of Geosciences*, Vol. 11, No. 13, pp. 1-9.

Yıldırım, C., M. A. Sarıkaya, A. Çiner, 2016, "Late Pleistocene Intraplate Extension of the Central Anatolian Plateau, Turkey: Inferences from Cosmogenic Exposure Dating of Alluvial Fan, Landslide, and Moraine Surfaces Along the Ecemiş Fault Zone.", *Tectonics*, Vol. 35, No. 6, pp. 1446-1464.

Yilmaz, Y., O. Tüysüz, E. Yiğitbaş, Ş. Genç, A. M. C. and Şengor, 1997, "Geology and Tectonic Evolution of the Pontides", *IEEE Transactions on Systems, Man, and Cybernatics.*

Yoshimura, R., Y. Ogawa, Y. Yukutake, W. Kanda, S. Komori, H. Hase, ... and Y. Usui, 2018, "Resistivity Characterisation of Hakone Volcano, Central Japan, by Three-Dimensional Magnetotelluric Inversion", *Earth, Planets and Space*, Vol. 70, No. 1, pp. 1-10.

Zell, H., 2017, "Earth's Atmospheric Layers, NASA", https://www.nasa.gov/missionpages /sunearth/science/atmosphere-layers2.html, accessed on February 2022.

Zhang, K., W. Wei, Q. Lu, H. Dong, Y. Li, 2014, "Theoretical Assessment of 3-D Magnetotelluric Method for Oil and Gas Exploration: Synthetic Examples", *Journal of Applied Geophysics*, Vol. 106, pp. 23-36.

Zhu, R., P. Zhao, and L. Zhao, 2021, "Tectonic Evolution and Geodynamics of the Neo-Tethys Ocean", *Science China Earth Sciences*, pp. 1-24.

APPENDIX A: APPARENT RESISTIVITY AND PHASE
CURVES OF THE MT. ERCİYES
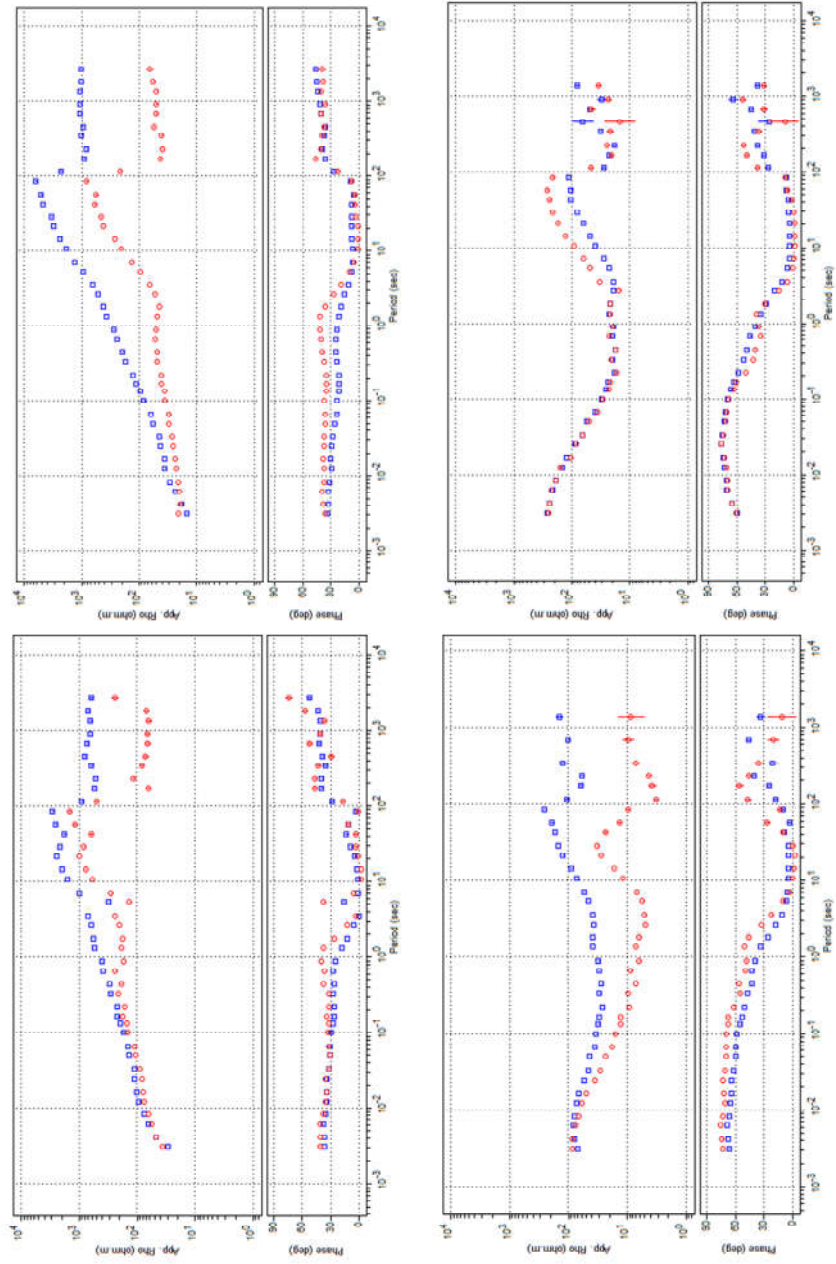
Figure A.1. Apparent resistivity and phase curves of station 29, 30, 28, and 26, respectively. See the map in Figure 6.4 for the station's location.
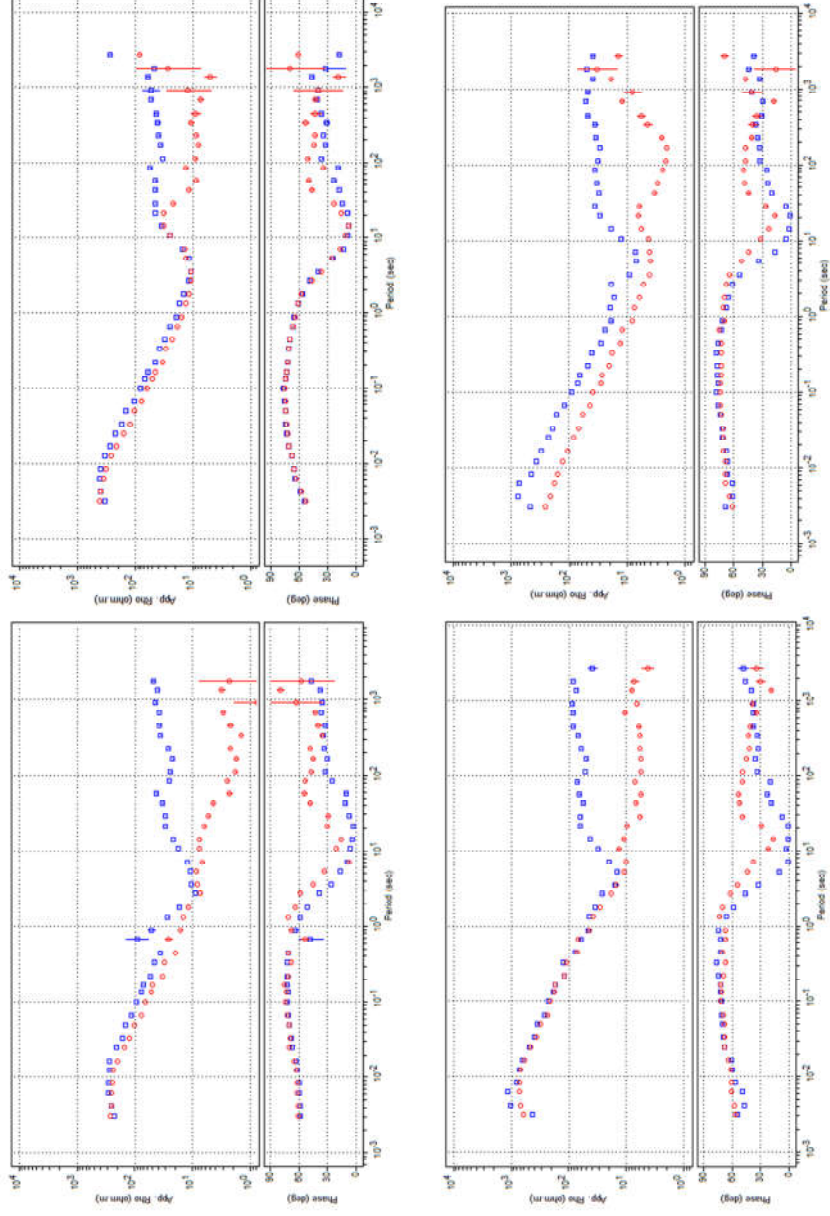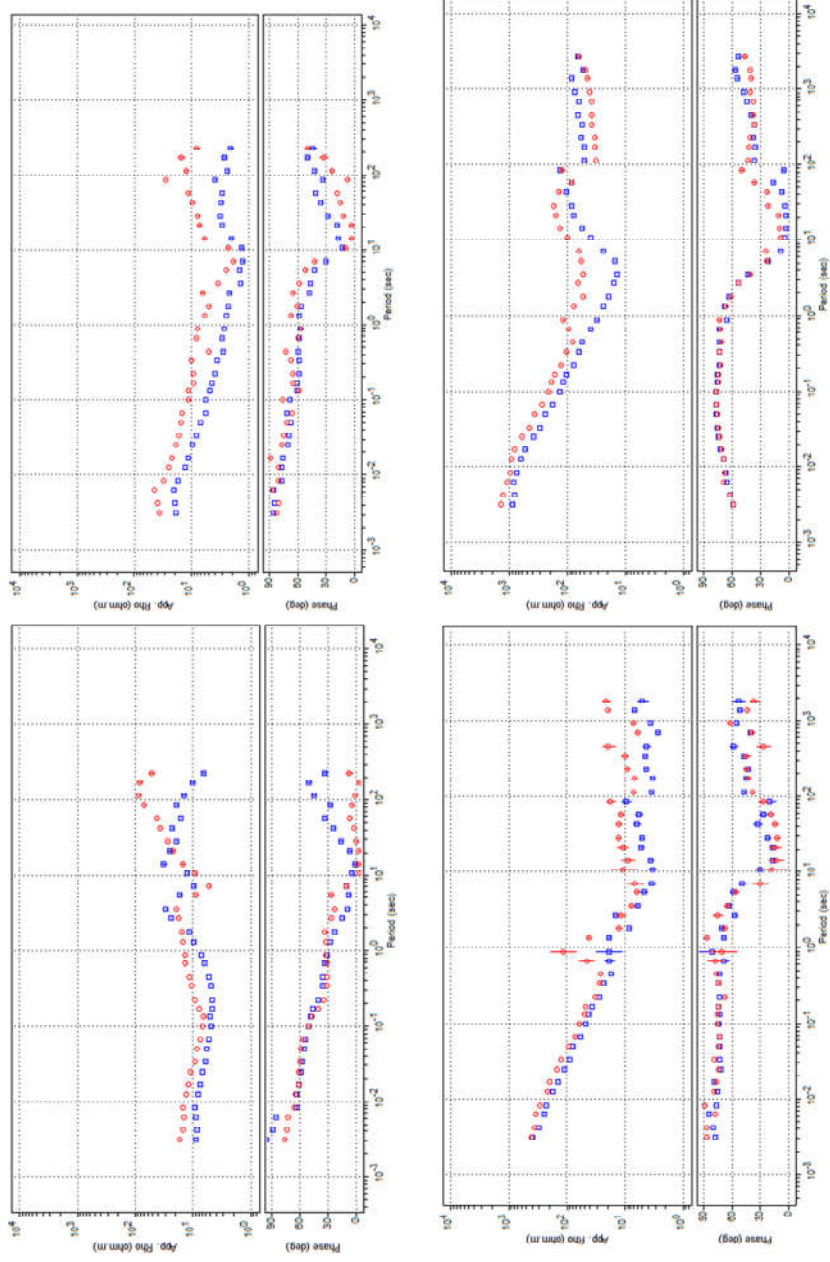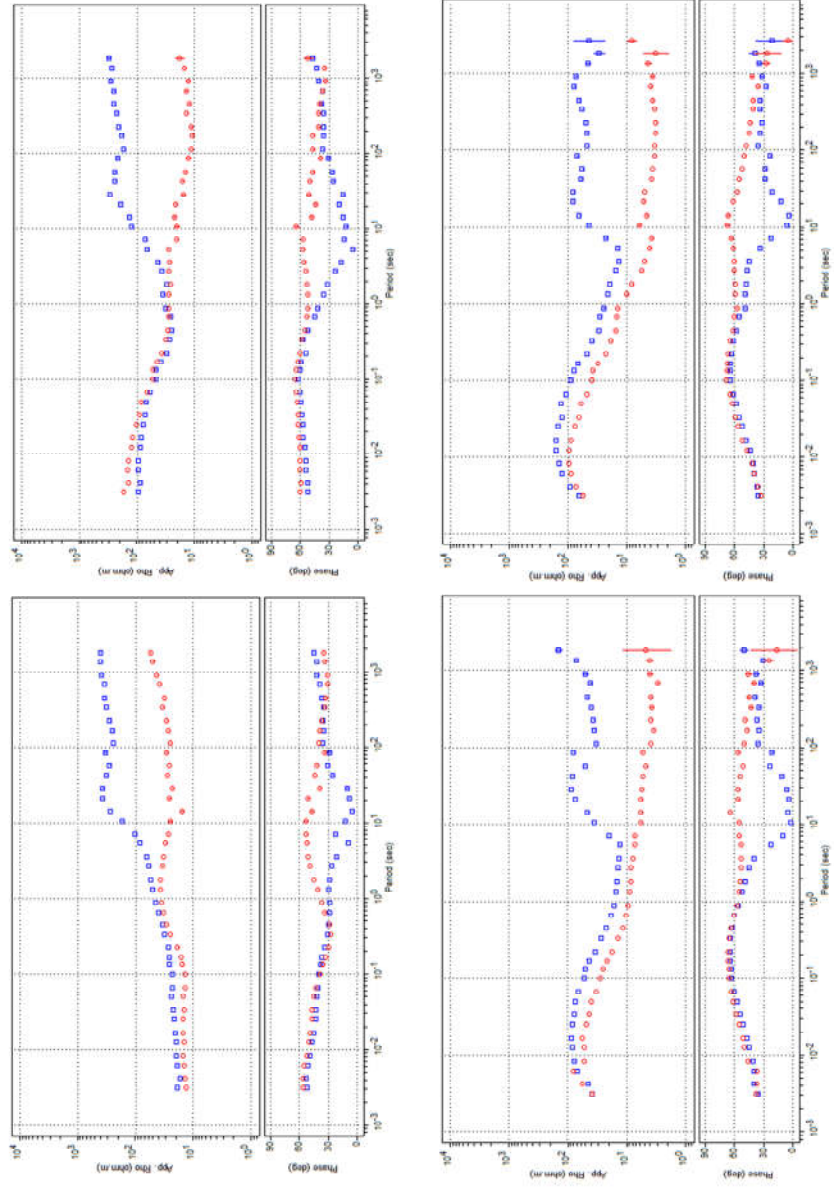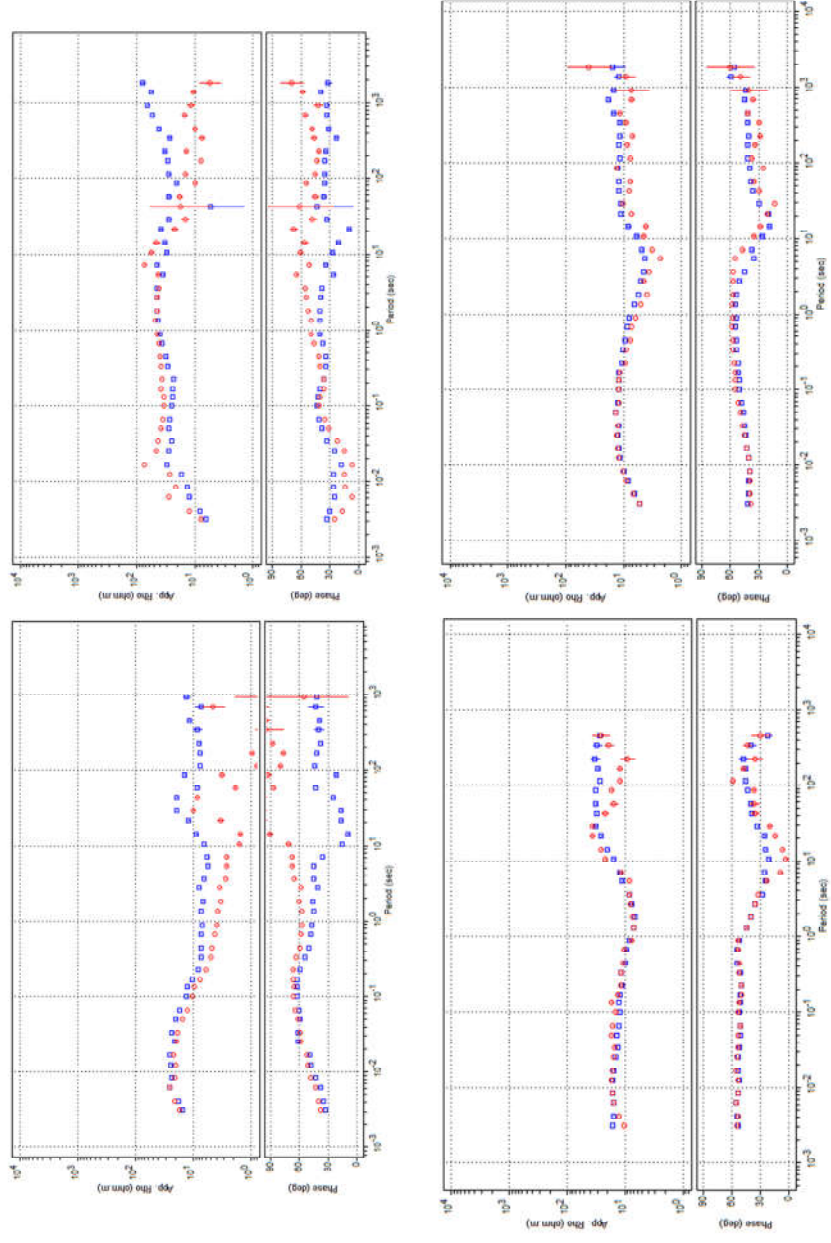
Figure A.2. Apparent resistivity and phase curves of station 27, 23, 24, and 17, respectively. See the map in Figure 6.4 for the station's location.
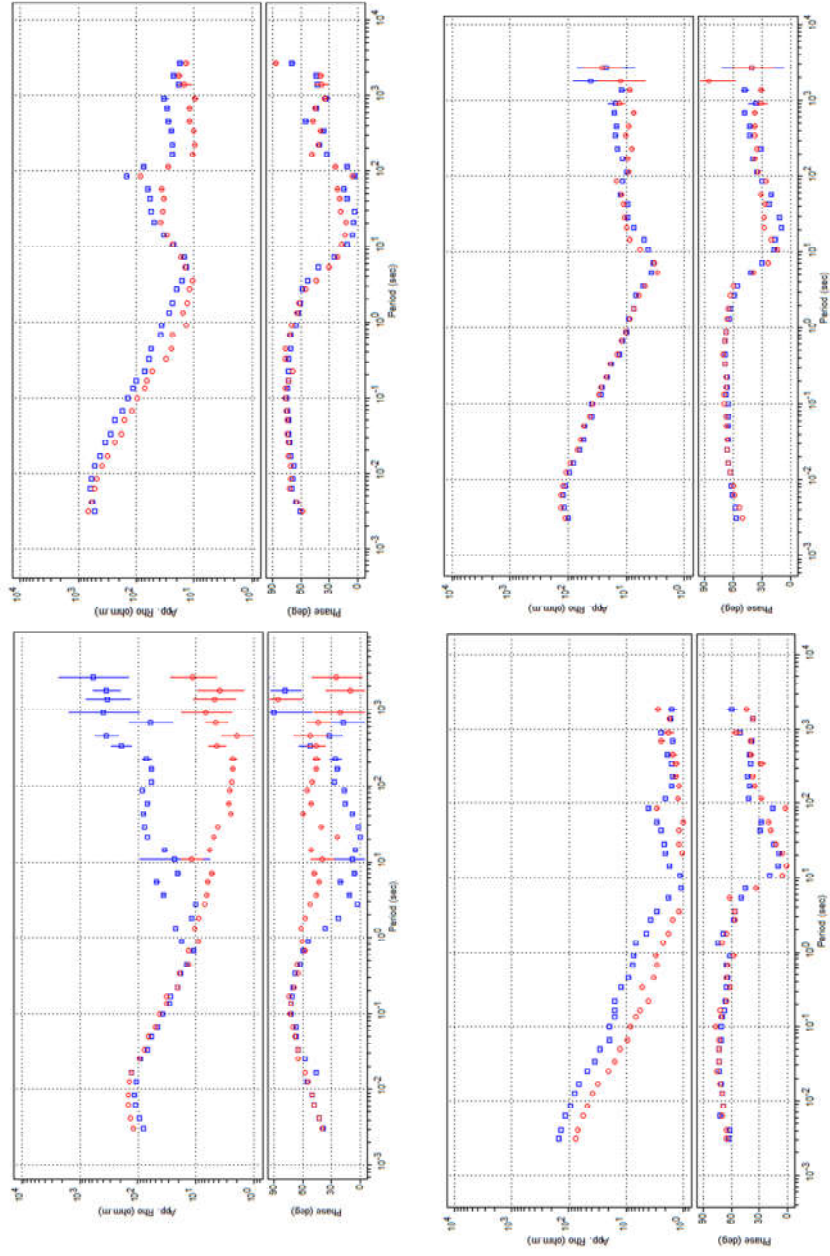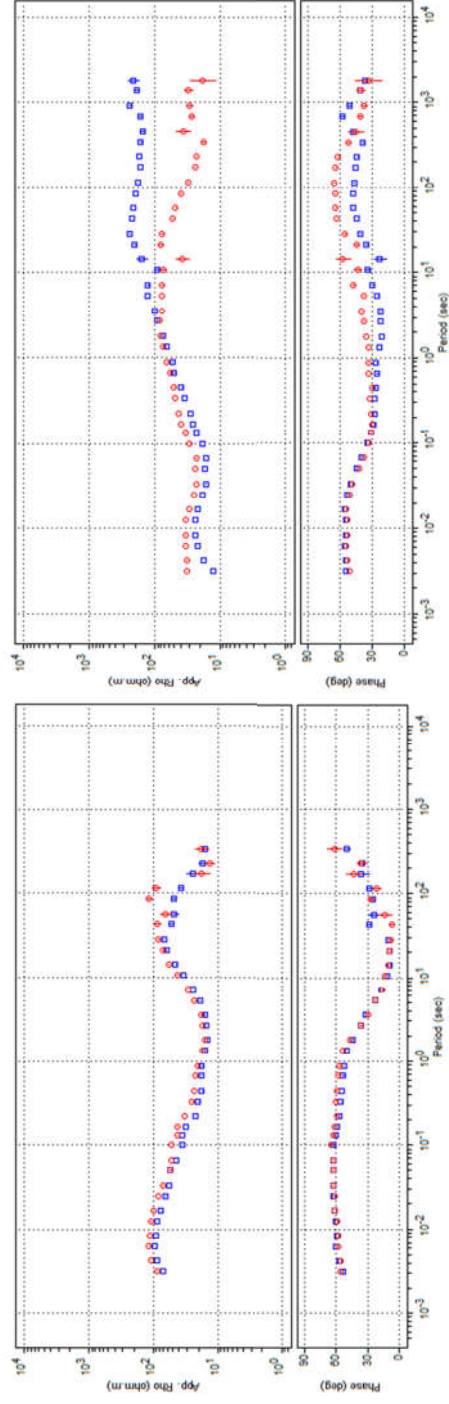
Figure A.3. Apparent resistivity and phase curves of station 31, 19, 15, and 16, respectively. See the map in Figure 6.4 for the station's location.
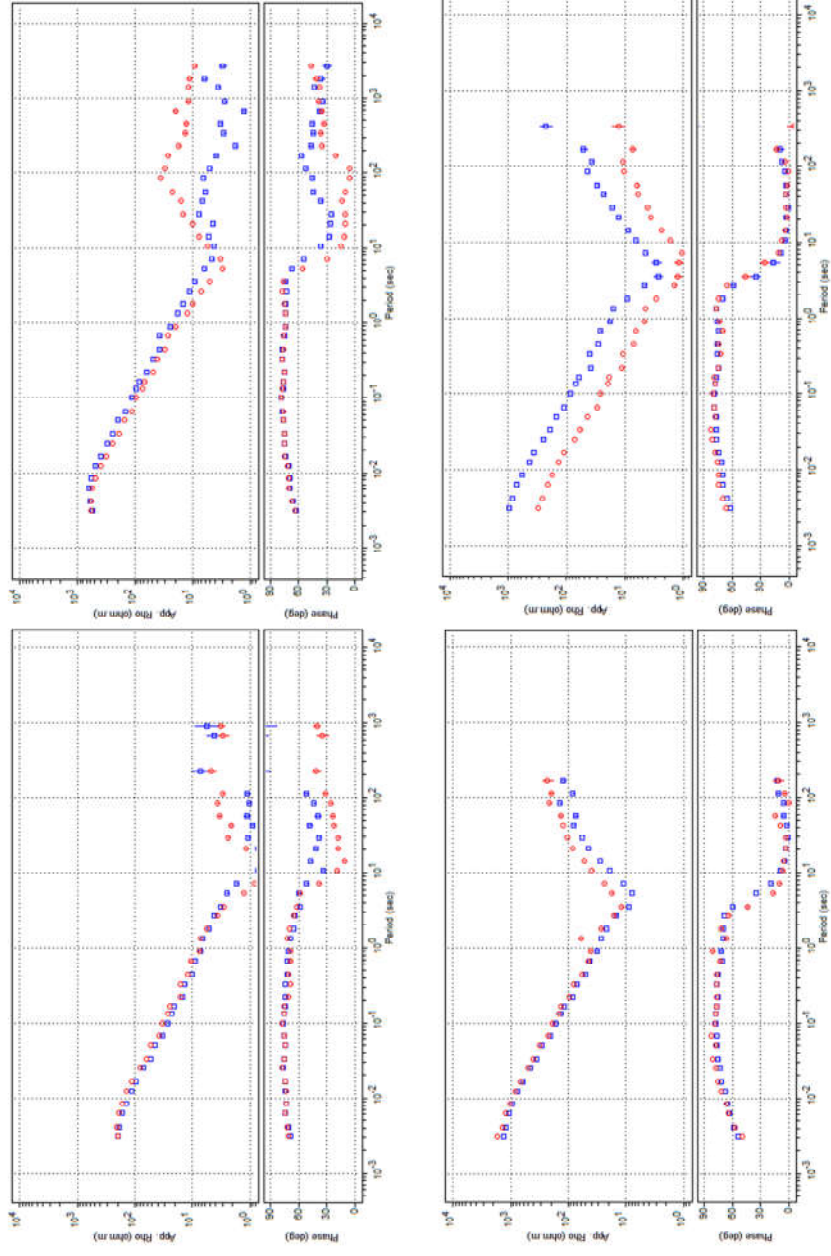
Figure A.4. Apparent resistivity and phase curves of station 13, 12, 20, and 21, respectively. See the map

in Figure 6.4 for the station's location.
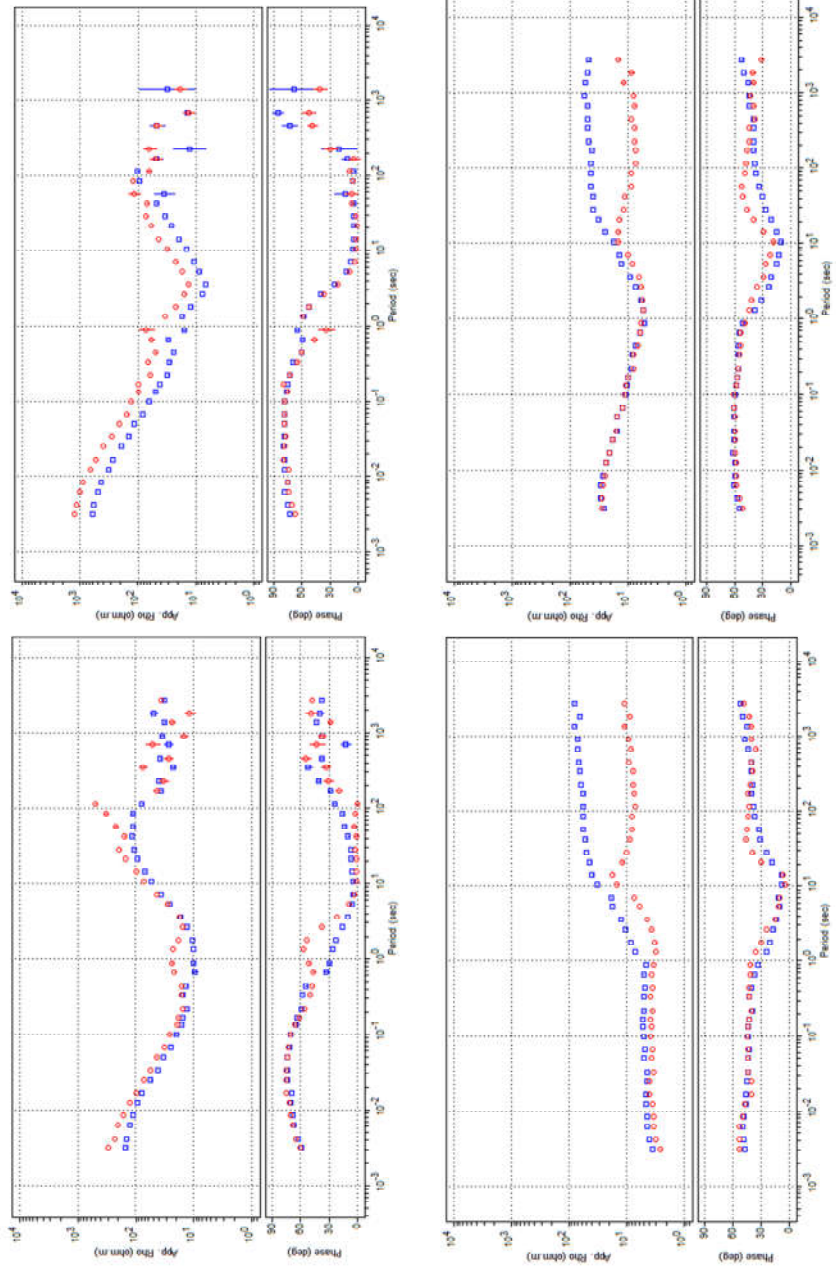
Figure A.5. Apparent resistivity and phase curves of station 25, 22, 2, and 3, respectively. See the map in Figure 6.4 for the station's location.
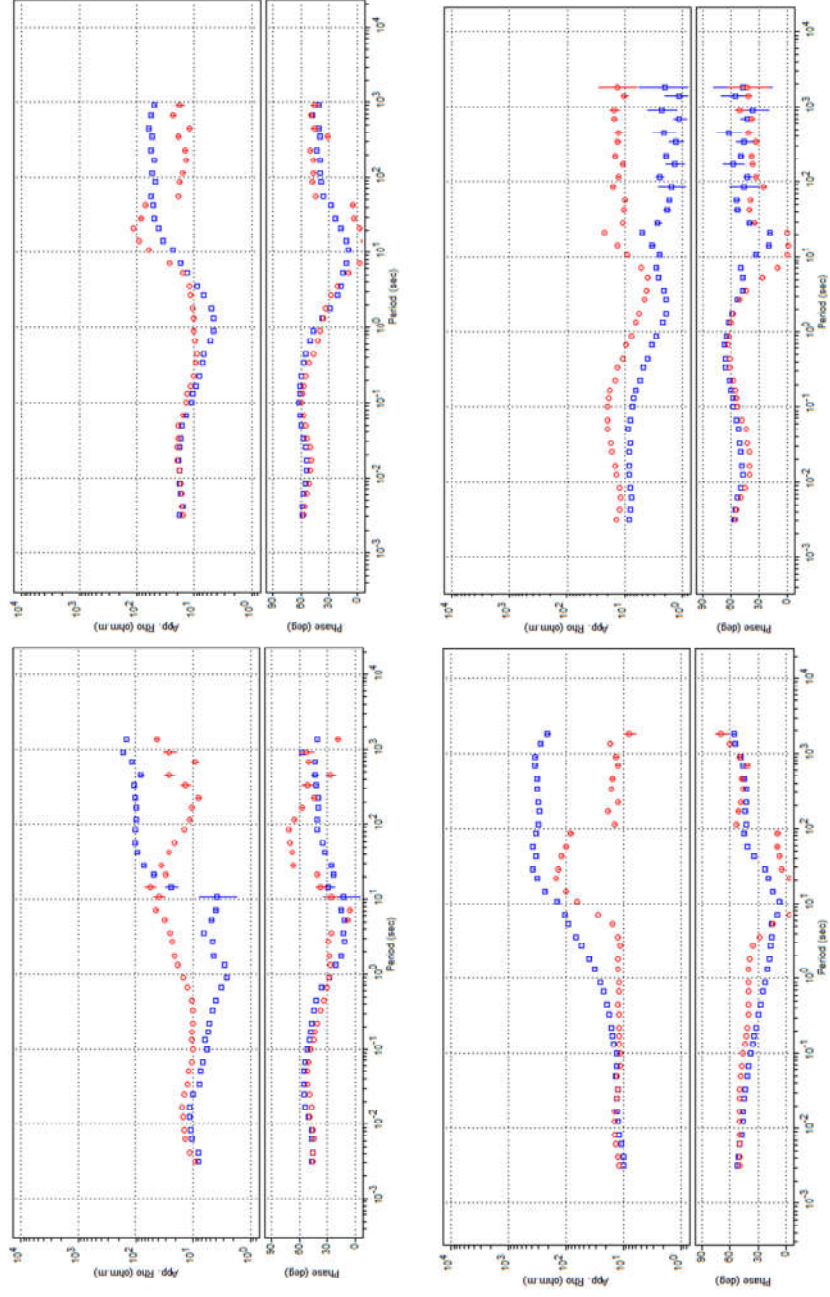
Figure A.6. Apparent resistivity and phase curves of station 4, 5, 6, and 8, respectively. See the map in Figure 6.4 for the station's location.

Figure A.7. Apparent resistivity and phase curves of station 10, 17, 14, and 11, respectively. See the map in Figure 6.4 for the station's location.

Figure A.8. Apparent resistivity and phase curves of station 33, 34, 35, and 36, respectively. See the map in Figure 6.4 for the station's location.

Figure A.9. Apparent resistivity and phase curves of station 37, 38, 1, and 7, respectively. See the map in Figure 6.4 for the station's location.

Figure A.10. Apparent resistivity and phase curves of station 9 and 32, respectively. See the map in Figure 6.4 for the station's location.

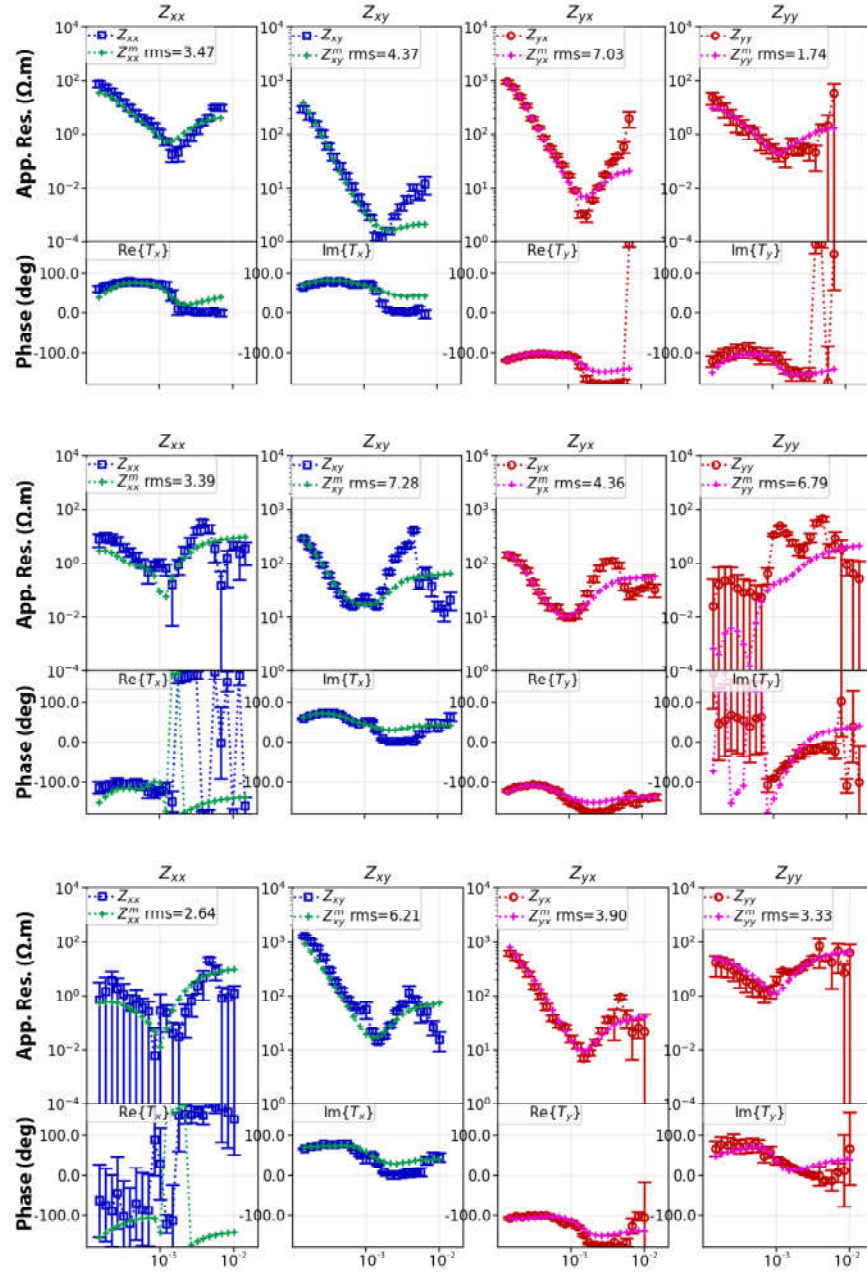# APPENDIX B: FITTING CURVES OF FINAL ERCİYES MODEL
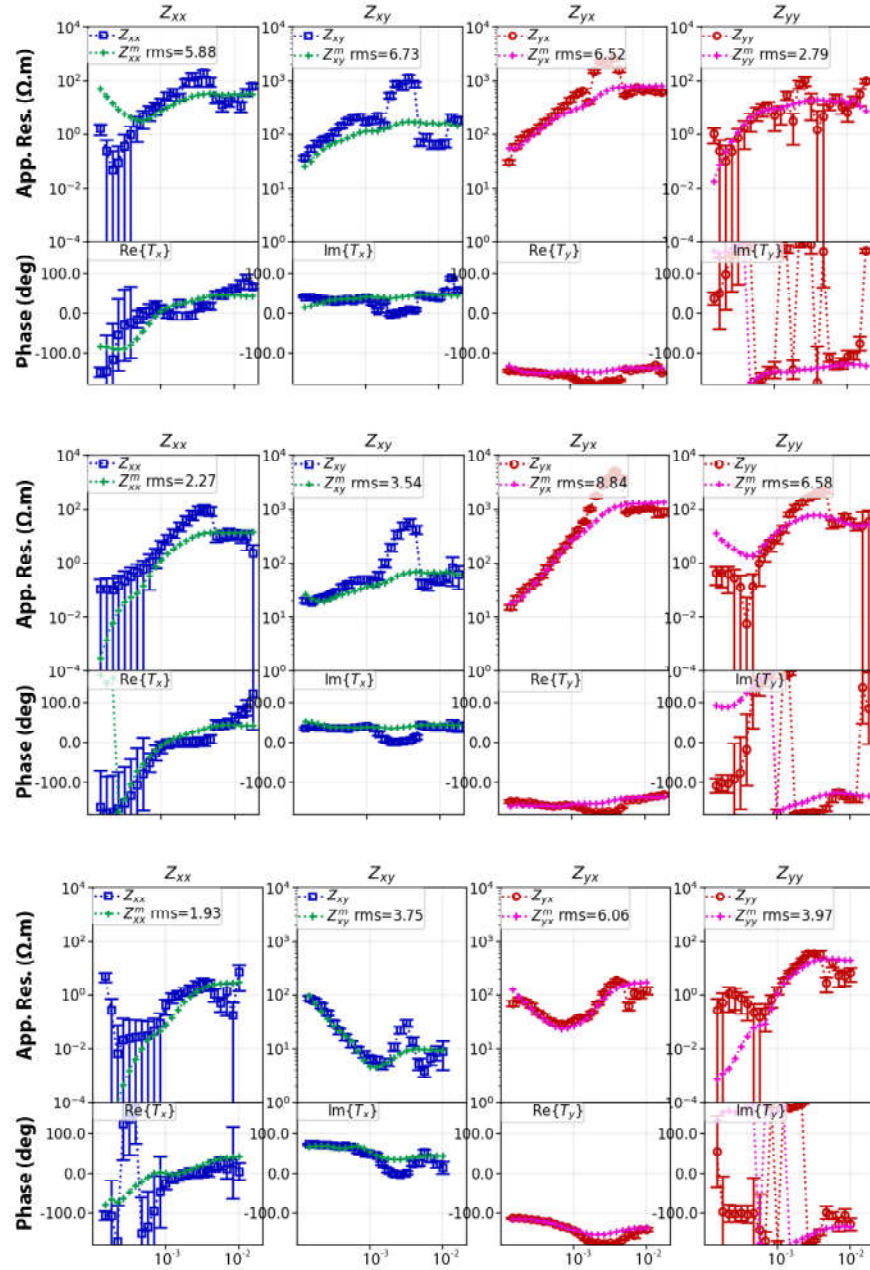
Figure B.1. Fitting curves of station 29, 30 and 28 for the final resistivity model. See the map in Figure 6.4 for the station's location.
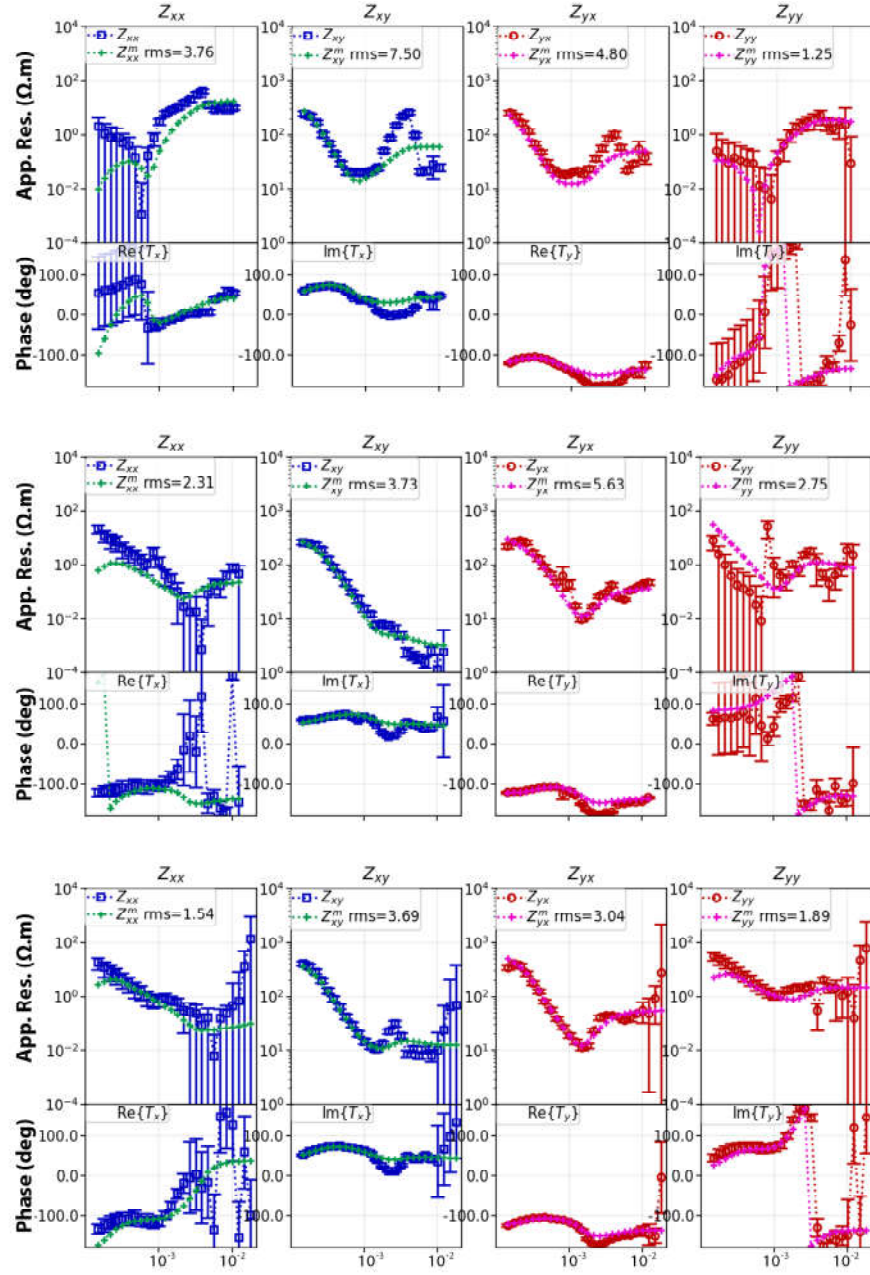
Figure B.2. Fitting curves of station 26, 27 and 23 for the final resistivity model. See the map in Figure 6.4 for the station's location.
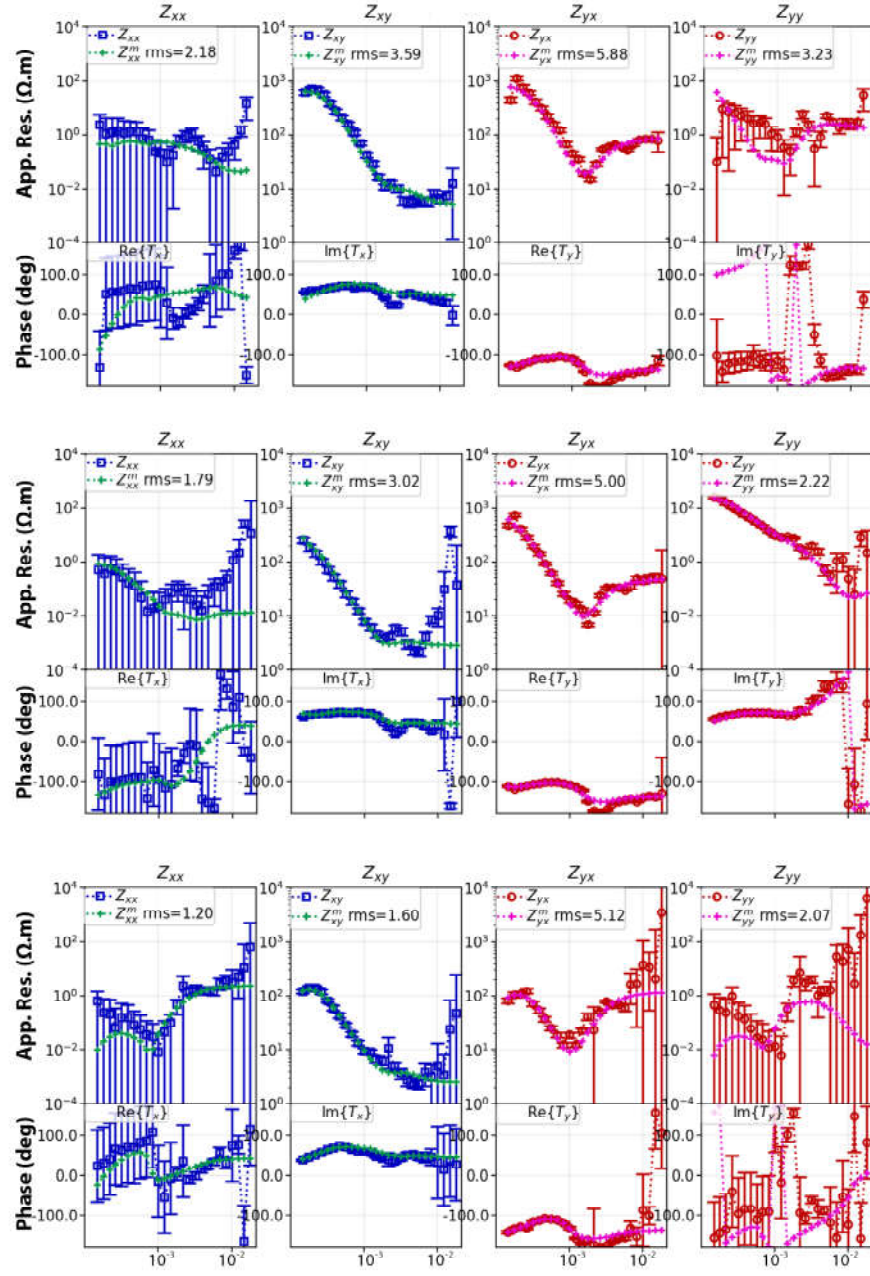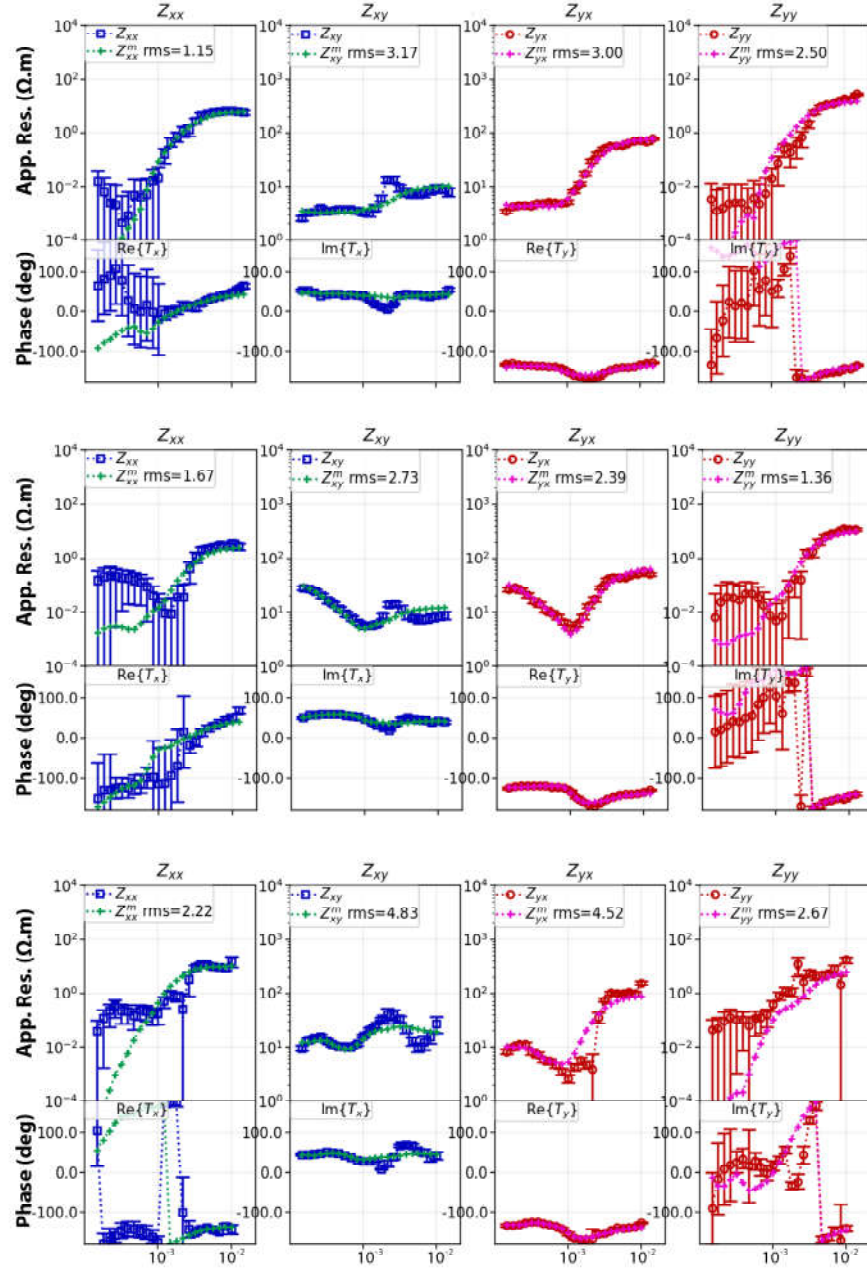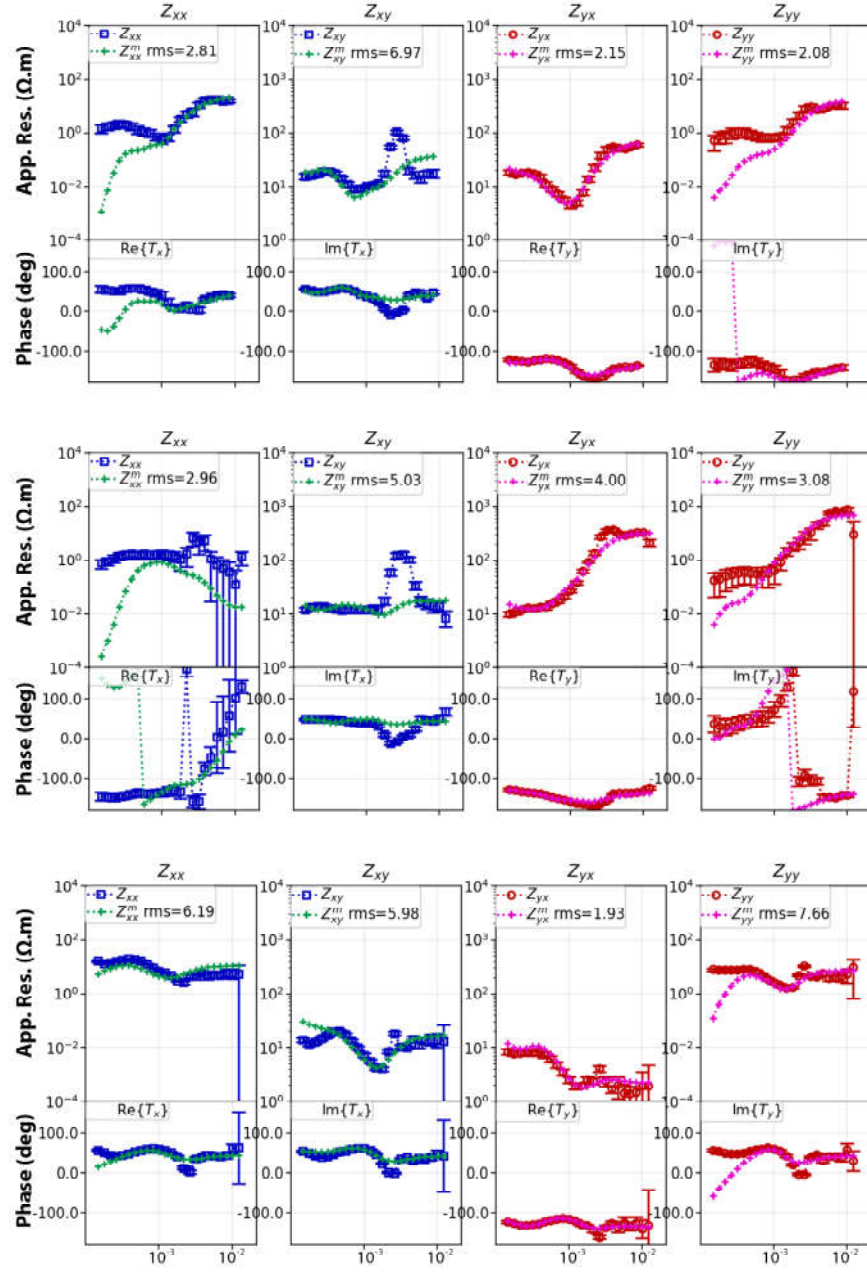
Figure B.3. Fitting curves of station 24, 18 and 31 for the final resistivity model. See the map in Figure 6.4 for the station's location.
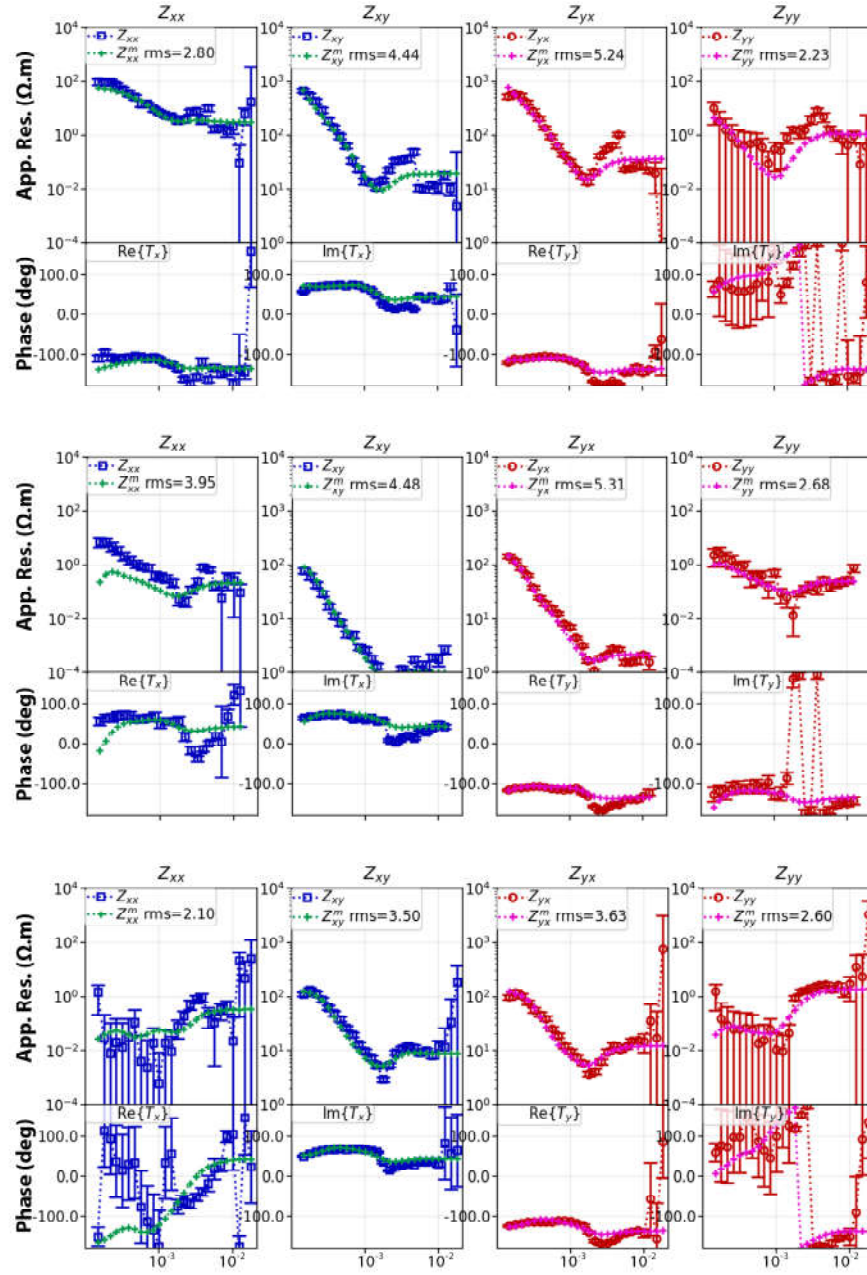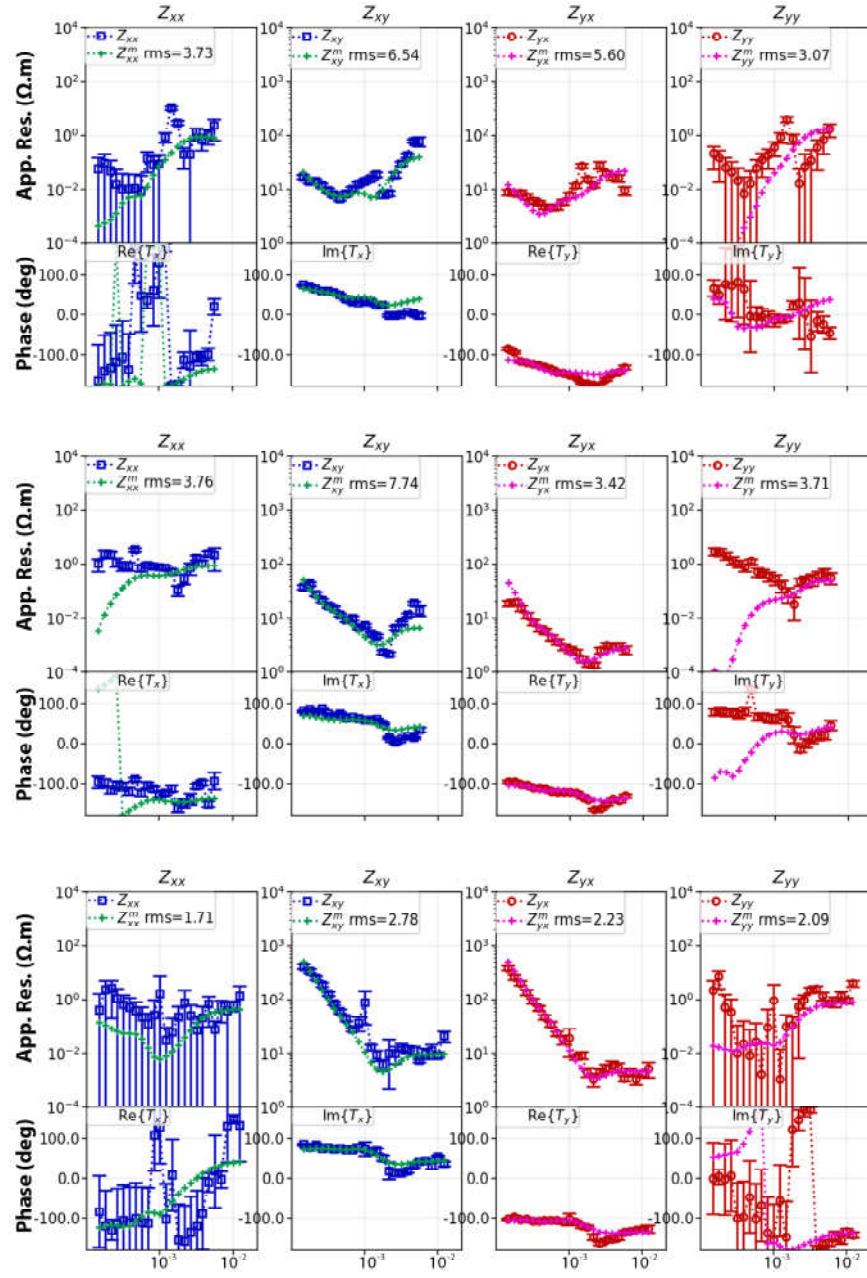
Figure B.4. Fitting curves of station 19, 15 and 16 for the final resistivity model. See the map in Figure 6.4 for the station's location.
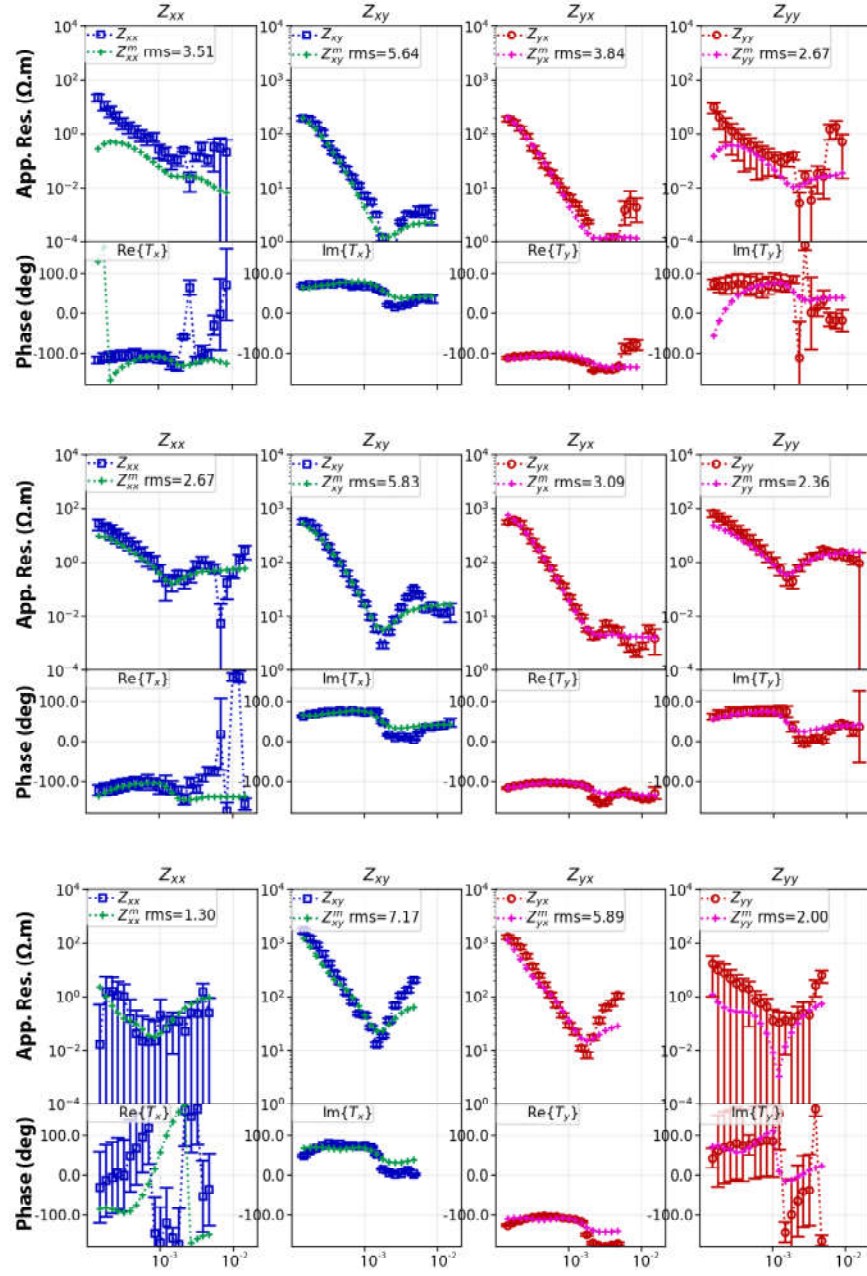
Figure B.5. Fitting curves of station 13, 12 and 20 for the final resistivity model. See the map in Figure 6.4 for the station's location.

Figure B.6. Fitting curves of station 21, 22 and 25 for the final resistivity model. See the map in Figure 6.4 for the station's location.

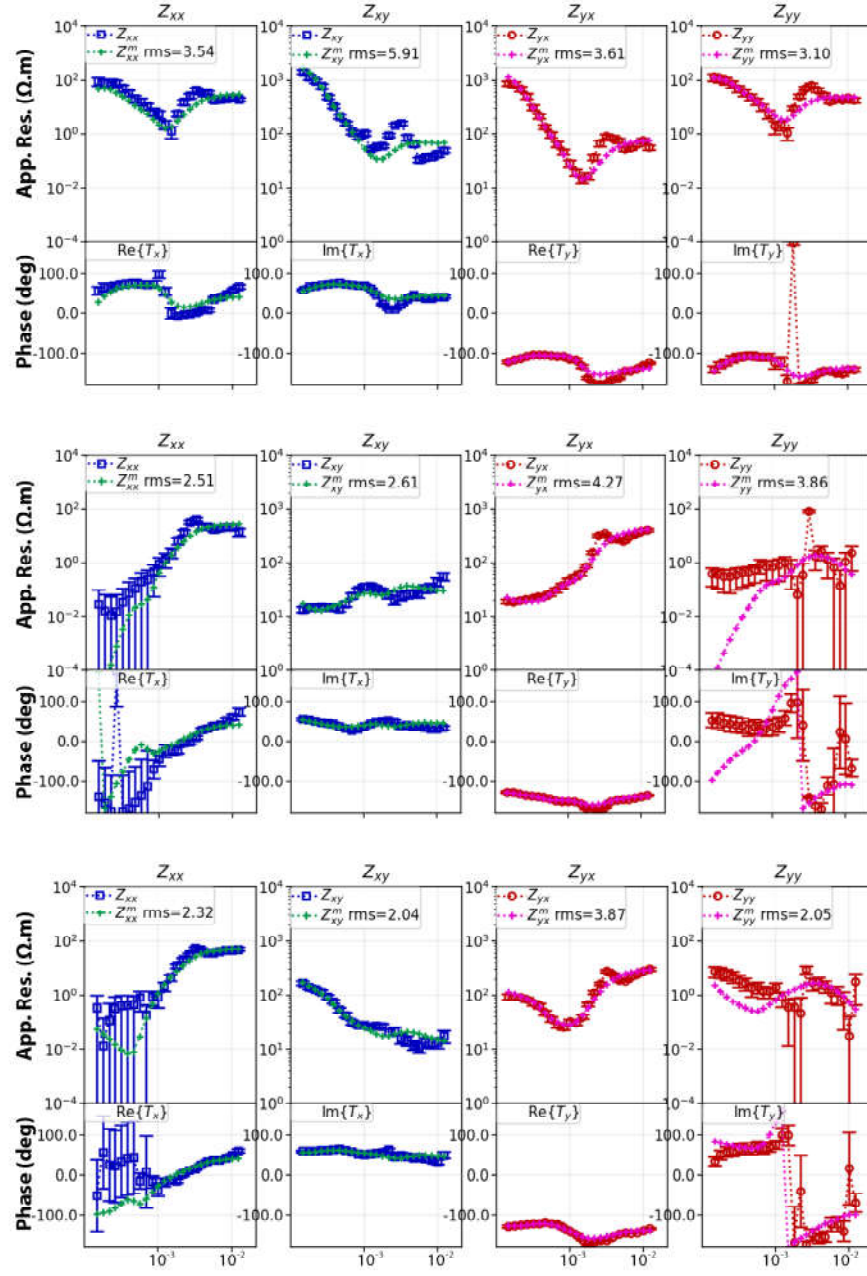Figure B.7. Fitting curves of station 2, 3 and 4 for the final resistivity model. See the map in Figure 6.4 for the station's location.

Figure B.8. Fitting curves of station 5, 6 and 8 for the final resistivity model. See the map in Figure 6.4 for the station's location.

Figure B.9. Fitting curves of station 10, 17 and 14 for the final resistivity model. See the map in Figure 6.4 for the station's location.

Figure B.10. Fitting curves of station 11, 33 and 34 for the final resistivity model.
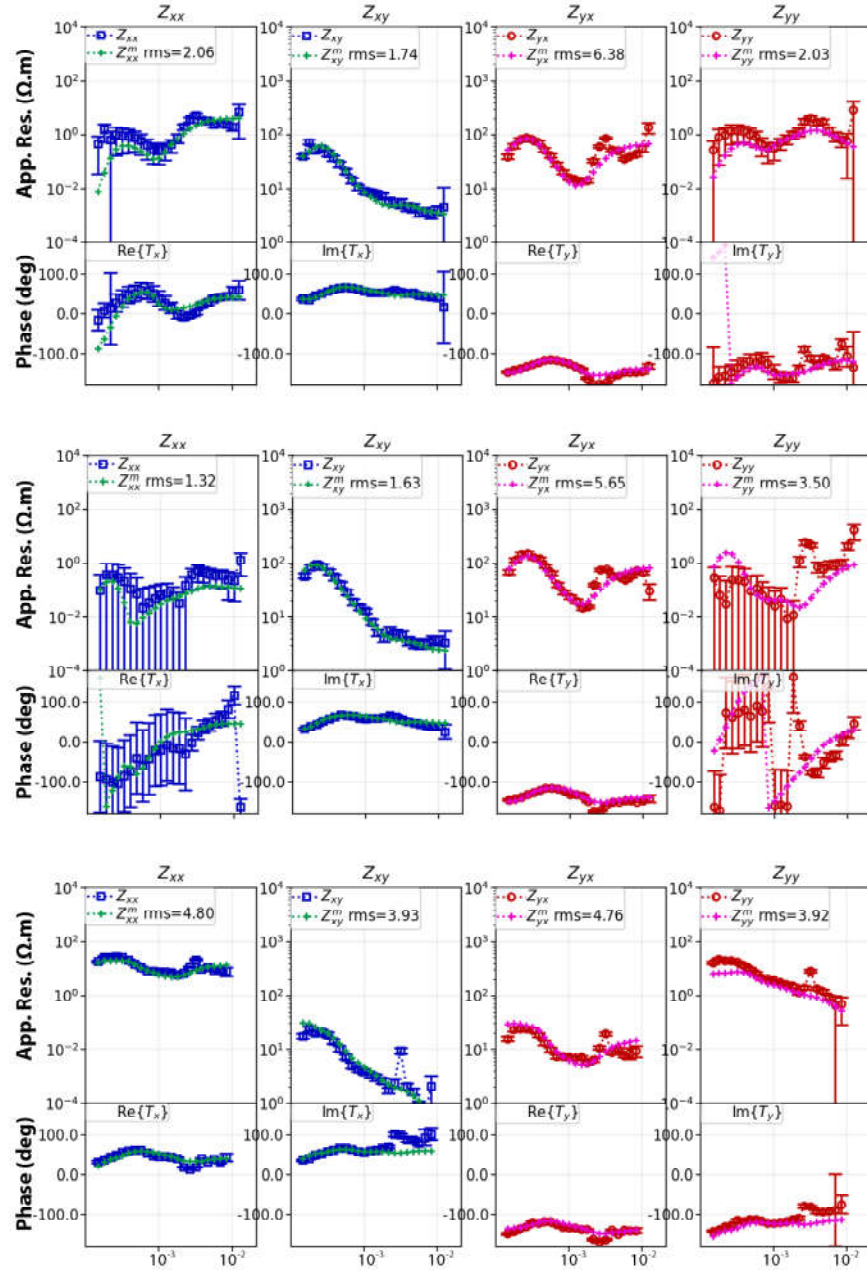See the map in Figure 6.4 for the station's location.

Figure B.11. Fitting curves of station 35, 36 and 37 for the final resistivity model. See the map in Figure 6.4 for the station's location.
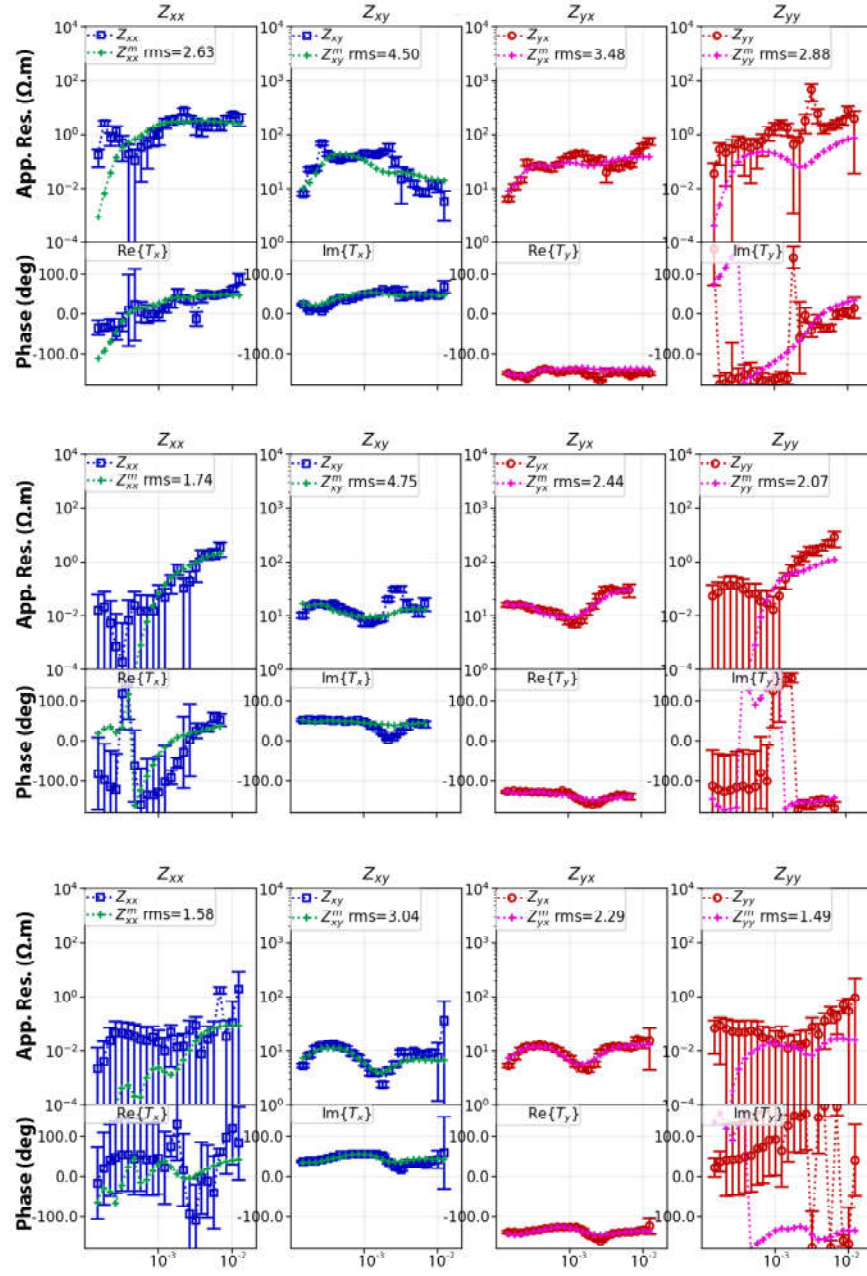
Figure B.12. Fitting curves of station 38, 1 and 7 for the final resistivity model. See the map in Figure 6.4 for the station's location.
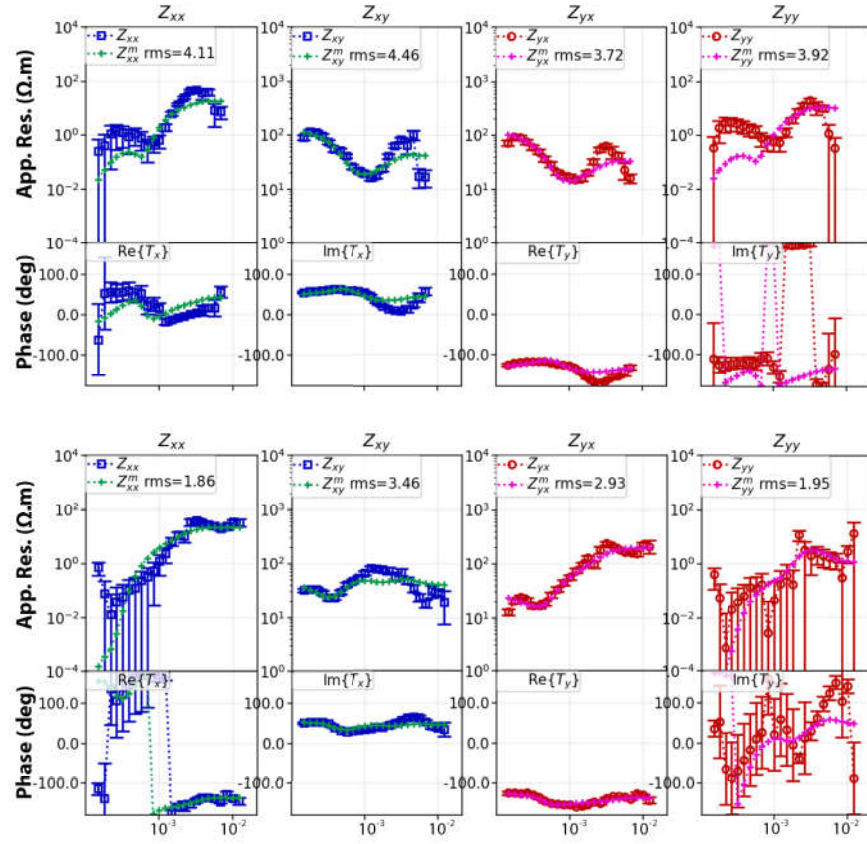
Figure B.13. Fitting curves of station 9 and 32 for the final resistivity model. See the map in Figure 6.4 for the station's location.